A Multifaceted Photocatalytic Exploration – From Alkyne Semi-Hydrogenation to Plasmonic Nanostructures.

Melissa Julieth Cely Pinto

A thesis submitted to the Faculty of Science in partial fulfillment of the requirements for the Doctorate in Philosophy degree in Chemistry

Department of Chemistry and Biomolecular Sciences
Faculty of Science
University of Ottawa

Supervisor: Juan (Tito) Scaiano

In dedication to:

God for giving me the opportunity and strength to achieve my goals and to be successful during this experience.

To my mentor Dr. Tito Scaiano for helping me develop my skills, continuous support and to open the opportunity to study in Canada.

My husband, Alejandro, for his love, endless support, and encouragement. You have been a listener and a supporter throughout this entire experience. You have been a source of strength, support, patience, and motivation for me. I am truly blessed to have you as my partner in this dance called life.

My family, especially my aunties (mis tías) and parents, Eddy and Gelver, who have taught me to believe in myself, to always strive for the best, and even the largest task can be accomplished if it's done one step at a time. Thank you for your guidance and love/¡Gracias por tantas enseñanzas Familia!.

&

I also dedicate this dissertation to my friends who have supported me throughout the process. I will always appreciate all you have done.

"*Strive not to be a success, but rather to be of value."*
- Albert Einstein.
"*The greatest glory in living lies not in never falling, but in rising every time we fall.*"
-Nelson Mandela.

Abstract

In this dissertation, we summarize the effect of metal nanoparticles (NPs) and metal nanoparticle-decorated titanium dioxide (M@TiO_2) materials in processes such as photoenolization, and semi-hydrogenation of alkynes. We also studied the photochemistry of substituted aromatic ketones such as tetralones and capping ligands such as lipoic acid for the synthesis of metal nanostructures. The primary objective of this multifaceted research was to identify optimal conditions and mechanisms that enhance both reaction efficiency and the fast synthesis of nanostructures. By focusing on molecules that can revert to their original state, we aim to increase their availability for further chemical reactions. This work also contributes to the development of more effective catalytic systems, facilitating innovative applications in organic synthesis. Furthermore, our research addresses practical challenges faced at the laboratory level, where students often find difficult to monitor reactions in a timely manner. Timely monitoring is crucial for successful organic transformations, and photocatalysis offers a significant advantage by allowing easy control of the reaction environment through the simple on/off manipulation of light, since light serves as the initial factor that initiates the reactions. This approach not only enhances reaction management but also leads to the development of cost-effective catalysts that can serve as an alternative materials, reducing reliance on those that are currently depleting, such as palladium.

Firstly, we investigated the photoenolization process as a convenient driver for the synthesis of gold (Au) nanostructures using the substituted ketone 3,3,6,8-tetramethyl-1-tetralone which undergoes photoenolization to produce a photoenol excited state with a lifetime of around~3 μs, which involves the carbonyl triplet state of the ketone (τ ~1.9 ns), as a precursor. For this, we used the laser flash photolysis (LFP) technique to evaluate the absorbance signal over time after the excitation of the sample with a laser pulse. The change in absorbance can result in decay or growth signals from transient species created in the sample from the laser excitation and can be monitored through time leading us to conclusions on the structure of the species. In this case, we monitored the excited states of the photoenol and the ketone itself. In the case of excited photoenol like the one from the selected tetralone, if metal ion trapping fails, it returns to the original ketone precursor and remains available for future events that can lead to the synthesis of target nanoparticles (NPs). This study also

includes the characterization of the photochemistry of the substituted tetralone, and the dual behaviour of reaction intermediates, as biradicals and excited states, in energy and electron transfer processes.

Furthermore, we studied the photopolymerization of α-lipoic acid (LA) as a novel approach to produce a cross-linked polymeric matrix of lipoic acid monomers (PALA) which helps to control the size of plasmonic gold nanostructures when using the same substituted ketone 3,3,6,8-tetramethyl-1-tetralone, previously mentioned, as the photo-initiator for the reduction of Au(III) to Au^0. A complete characterization of the polymer is included, and the dual behaviour of LA as an in-situ stabilizer for the nanostructures and reducing agent is investigated. These findings are relevant to the understanding of the photochemical transformation of this biologically relevant compound and would benefit the increasing use of LA and PALA for the synthesis of various nanomaterials.

Likewise, to further explore the role of photocatalysts in organic chemistry processes, we explored the semi-hydrogenation reaction of alkynes. This reaction is particularly important in the fine chemicals and pharmaceutical industries, and it is thus important to find catalytic processes that will drive the reaction efficiently and at a low cost. The real challenge is to drive the alkyne-to-alkene reaction while avoiding over-hydrogenation to the saturated alkane moiety. The problem is more difficult when dealing with aromatic substitution at the alkyne center. M@TiO_2 materials were used in this research as heterogeneous catalysts, offering the advantage of an ease-catalyst separation. Particularly, systems such as Pd@TiO_2, Cu@TiO_2 and CuPd@TiO_2. Photocatalysts based on Palladium (Pd) tend to proceed to the alkane moiety, and stopping at the alkene with good selectivity requires very precise timing with basically no timing tolerance when the reaction times are measured in hours or overnight. However, the goal of high conversion with high selectivity could be achieved with TiO_2-supported copper (Cu@TiO_2), although with slower kinetics than for Pd@TiO_2. Therefore, by combining the features of both metals in one catalyst, we discovered that the novel bimetallic catalyst, namely, CuPd@TiO_2 (0.8% Cu and 0.05% Pd), could improve the kinetics by 50% with respect to Cu@TiO_2, while achieving a selectivity over 95% and with exceptional timing tolerance when methanol was used as the hydrogen source in the system.

Further, the low Palladium content minimizes its use, as Palladium is regarded as an element at risk of depletion.

Additionally, in order to facilitate catalyst separation from batch reaction and develop a suitable catalytic system we employed a magnetic catalyst named Fe_3O_4@TiO_2 to explore the synthesis of Schiff Bases from Benzyl Alcohol and Nitrobenzene. Schiff bases are condensation products of primary amines with carbonyl compounds like aldehydes or ketones and are extensively used in different fields. They serve multiple purposes such as dyes, catalysts, and intermediate species in organic synthesis. They have also demonstrated diverse biological activities including antibacterial and antifungal activities. In this study, we compared the efficiency of the magnetic catalyst with respect to Pd@TiO_2, Cu@TiO_2, and TiO_2 under ultraviolet light (UV) and inert atmosphere.

Finally, moving into another technique of catalysis, we investigated the mechanistic and kinetic studies of polarity reversal catalysis involving amino-boranes compounds that serve as catalysts generating nucleophilic radicals that can abstract hydrogen from electron-poor substrates such as nitriles. This ongoing research allows us to form electrophilic radicals from electron-deficient molecules. By using LFP we have successfully monitored both radicals from these molecules and boryl radical species.

Acknowledgements

I would like to start by expressing my gratitude to my Ph.D. supervisor, Dr. Juan (Tito) Scaiano. Prof. Scaiano, you allowed my family and me to come to Canada by accepting me as your student. In this journey, you have allowed me to pursue my dreams as a Professional at the University and also in your laboratories, and at the same time you have given me the possibility to learn and enjoy the amazing country Canada is. You are a distinguished scientist, an incredible, kind, and inspiring person and one of the many things I have always admired from you is your passion for academia and your ability to describe and explain the necessary chemical concepts to understand the chemistry behind every experiment. Your stories have inspired me to strive always to be a better person and chemist. I am very grateful and lucky to have the honor to be one of your students.

I would also like to thank Dr. Anabel Lanterna, for teaching and training me in different instruments in the lab, especially for having the patience to perform many Electron Paramagnetic Resonance (EPR) experiments with me. Your deep understanding of chemistry has profoundly influenced my daily research endeavors. I learned so much from you. You also were an amazing person to talk to about anything else outside the chemistry world. I appreciate all your support when I just arrived in Canada. I wish you the best of luck as a Professor at the University of Nottingham!.

I also want to personally thank Bowen Wang and Neeraj Yoshi in our group. Both of you have played essential roles in the laboratory and have helped me to enhance my skills in chemistry. I will be grateful for the assistance you have provided whenever I have faced challenges. I also extend my gratitude to the entire Scaiano group, including both past and present members. Your inclusive and supportive environment has made my journey truly rewarding. I wish you the best to each of you as you embark on your future endeavors. I truly believe in your potential to achieve remarkable achievements.

I also give my thanks to my closest friends in this journey: Mahzad, Daliane, and Saba. You have been great colleagues and mostly amazing friends. Your support in the natural ups and downs of this Ph.D. journey has made smoother my path. Thank you for your friendship.

My most sincere gratitude to my Family, especially my parents. You have always been there to help me achieve my dreams and earn a doctorate. Mom and Dad, you both have taught me to believe in myself and to strive for the best by being always a better person. Thank you for the way you raised me. Without my Family, I would not be where I am today.

My biggest thanks go to my husband, Alejandro. You have been there to help me through and push me when I have been at my lowest. Your love, support, and encouragement have made this chapter of my life both memorable and successful. I am immensely fortunate and deeply grateful to have you by my side. Thank you! Gracias!

Table of Contents

List of Publications

Publications presented in this Thesis

Melissa Cely-Pinto and Juan C. Scaiano*; Photoenolization as a convenient driver for the synthesis of plasmonic nanostructures. Photochemistry and Photobiology Science, **2021**, 20, 1611-1619.

Melissa Cely-Pinto, Bowen Wang and Juan C. Scaiano*; Understanding α-lipoic acid photochemistry helps to control the synthesis of plasmonic gold nanostructures. Photochemistry and Photobiology Science, **2023**, 22, 1299-1307.

Melissa Cely-Pinto, Bowen Wang and Juan C. Scaiano*; Photocatalytic Semi-Hydrogenation of Alkynes: A Game of Kinetics, Selectivity and Critical Timing. Nanomaterials, **2023**, 13, 2390.

Daliane Regis Correa da Silva, Melissa Cely-Pinto and Juan C. Scaiano*, Magnetic catalyst for efficient One-Pot Synthesis of Schiff Bases from Benzyl Alcohol and Nitro Compounds under UV irradiation. ***(After the initial submission process, we have successfully advanced to publication in Catalysts, 2024, 14(9), 612.)***

List of Figures

List of Tables

List of Schemes

List of Abbreviations

A	Acceptor
AFM	Atomic force microscopy
BDE	Bond dissociation energy
BenzA	Benzaldehyde
BR	Biradical
CB	Conduction band
CH_3CN	Acetonitrile
D	Donor
DCM	Dichloromethane
DHLA	Dihydrolipoic acid
DLS	Dynamic light scattering
DMSO	Dimethyl sulfoxide
DPhA	Diphenylacetylene
DPhB	1,4-Diphenylbutadiyne
DT	Decatungstate
DTBP	Di-tert-butyl peroxide
e^-	electron
EDS	Energy dispersive spectroscopy
EPR	Electron paramagnetic resonance
ESI	Electron spray ionization
EtOH	Ethanol
GC	Gas Chromatography
GPC	Gel permeation chromatography
h^+	hole
H^+	Hydrogen ions
HAT	Hydrogen atom transfer
HL	2N-salicylidene-5-(p-nitrophenyl)-1,3,4-thiadiazole
HOMO	Highest occupied molecular orbital
HPLC	High-performance liquid chromatography

hν	Light
I-2959	Irgacure-2959
IC	Internal conversion
ICCD	International Centre for Diffraction data
ICP-OES	Inductively coupled plasma - optical emission spectrometry
ISC	Intersystem crossing
Ka	Alkane
Ke	Alkene
K_{eT}	Rate constant of electron transfer
K_Q	Rate constant of quenching
Ky	Alkyne
LA	Lipoic Acid
LED	Light-emitting diode
LFP	Laser Flash Photolysis
LSPR	Localized Surface Plasmon Resonance
LUMO	Lowest unoccupied molecular orbital
M	Molar
M@TiO_2	Metal nanoparticle-decorated titanium dioxide
MeOH	Methanol
MIC	Minimum inhibitory concentration
mM	Milimolar
MNP	Metal Nanoparticle
MS	Mass Spectrometry
MV	Methyl Viologen
N/A	Not applicable
NA	Nitroanisole
NaCt	Trisodium citrate
Nd/YAG	Neodymium-doped yttrium aluminum garnet
NIR	Near Infrared
NMR	Nuclear magnetic resonance spectroscopy
NP	Nanoparticle

NPs	Nanoparticles
PALA	Cross-linked polymeric matrix of lipoic acid
PCC	Precipitated calcium carbonate
PhA	Phenylacetylene
PhP	1-Phenyl-1-Propyne
PMT	Photomultiplier Tube
PRC	Polarity Reversal Catalysis
PTFE	Polytetrafluoroethylene filter
PVC	Polyvinyl Chloride
PVP	Polyvinyl pyrrolidone
PXRD	Polycrystalline X-Ray Diffractometer
S_1	Singlet excited state
Sel	Selectivity
SEM	Scanning electron microscope
S_o	Ground state
SPR	Surface Plasmon Resonance
T_1	Triplet excited state
TEM	Transmission electron microscopy
THF	Tetrahydrofuran
UV	Ultraviolet
UVA	Ultraviolet A (315 nm – 400 nm)
UVB	Ultraviolet B (280 nm – 315 nm)
UVC	Ultraviolet C (100 nm – 280 nm)
UV-Vis	Ultraviolet-visible spectroscopy
VB	Valence band
XPS	X-ray photoelectron spectroscopy
ΔE	Energy gap
ΔOD	Change in absorbance over time
τ	Lifetime
3-BA	3-Benzylaniline

1. Introduction

1.1. Opening Remarks

The work presented in this dissertation is focused on the field of photochemistry and photocatalysis. This doctoral thesis comprises three peer-reviewed scientific publications[1,2,3] (chapters 2-4), and one publication undergoing the pre-submisison process (chapter 5). I was the first contributing author for the scientific publications of chapters 2-4, thus the majority of the experimental work was completed by me. Additionally, chapters 5-6 involved collaboration with my colleagues Daliane Regis Da Silva and Saba Didarataee respectively. In chapter 5 titled "*Magnetic catalyst for efficient One-Pot Synthesis of Schiff Bases from Benzyl Alcohol and Nitro Compounds under UV irradiation*", Daliane Regis Da Silva focused on synthesizing the magnetic catalyst (Fe_3O_4@TiO_2[1]), a material she had extensive experience with from her doctoral studies. Meanwhile, I synthesized the other metal-based TiO_2 catalysts (Pd@TiO_2 and Cu@TiO_2) disclosed in the same chapter. Both, Daliane and I conducted the chemical reactions and analyzed the results. On the other hand, chapter 6 directed to Future work: Polarity reversal catalysis, Saba Didarataee and I shared responsibility for conducting the reactions and analyzing the results. I would like to highlight that within the Scaiano group, Saba has been actively involved in working with decatungstate (DT, $W_{10}O_{32}^{4-}$), which is part of the suggestions for continuing this ongoing research.

Chapters 2-5 include the manuscripts and supporting information. On the other hand, chapter 6 corresponds to a partial summary of the results obtained in our exploration of polarity reversal catalysis, along with proposed future directions to advance this area of research. Likewise, this introductory chapter will focus on introducing the reader to the background knowledge required to understand the information disclosed in this document

[1] The symbol '@' in this context denotes that the component on the left decorates the component on the right, highlighting a surface interaction between the two materials.

related to photochemistry, nanomaterials, radical chemistry, and heterogeneous photocatalysis.

Photochemistry not only offers the tools for synthesizing catalysts based on M@TiO_2 materials and nanostructures but also the study of chemical reactions and the transient species that can be formed. These capabilities are essential in different applications in chemistry and particularly, in this dissertation our focus lies on using different photoactivated precursors for the synthesis of nanostructures, semi-hydrogenation processes, radical chemistry, and other organic synthesis. Thus, it is noteworthy that using light as part of different reactions and preparing photo-responsive materials has emerged as one of the most studied approaches for alternative and sustainable routes of chemical synthesis. This approach helps in understanding the features of these materials and also clarifies the roles played by intermediate species in these processes.

Light is involved in all the projects herein discussed and it is defined as electromagnetic radiation with different wavelengths. The visible region (400-700 nm) can be seen by the human eye, and it has been widely used in this field because of the availability of sources, including sunlight. Ultraviolet light (UV) can be categorized according to its spectral ranges. Specifically, UVA radiation is characterized by wavelengths ranging from 315 nm to 400 nm, and it is this range that window glass allows to pass through. On the other hand, UVB radiation, covering the range of 280 nm to 315 nm,is blocked by window glass.. In contrast, UVC is the light that is not part of the solar spectrum at sea level.[4] Therefore, given that light is energy and plays an essential role in all the discussed reactions within this dissertation, it is imperative to mention two fundamental concepts: the first and second principles of photochemistry: the first principle states that "*Light must be absorbed to cause any chemical change"*, while the second one asserts that "*for each photon of light absorbed by a molecule, only, one molecule is activated for a photochemical reaction*". [5] Thus, regardless of the specific chemical reaction, the photons in these reactions must possess enough energy to meet the requirements of the process.[4] Further discussion on the main objectives and structure of this dissertation will be provided at the end of this chapter.

1.2. Introduction to Photochemistry

Photochemistry is concerned with the chemical changes that occur by the interaction of light with matter. Chemical reactions that result from exposure of chemical systems to light have been called photochemical reactions, and their study comprises the science called photochemistry. According to Nicholas J. Turro,[6] the term photochemical reaction has taken on a more specific definition: "*a photochemical reaction starts in one of the electronically excited states of a reactant and ends with the appearance of the first ground-state product(s)".* That is, photochemical reactions belong to the category of electronic relaxation processes wherein the molecule does not return to its initial state. With this in mind, photochemical reactions are different from conventional thermal reactions given that the former always involves a molecule possessing an excited state. In this sense, for a photochemical process to begin, a molecule must initially have the ability to absorb photons (hν) at a specific frequency. When the absorbed energy is high enough, the molecule is excited, causing an electron from the ground state electronic level to transition to another one of higher energy. Figure 1.2.1 illustrates a simplified Jablonski diagram which shows the different processes a molecule can have after the absorption of a photon.

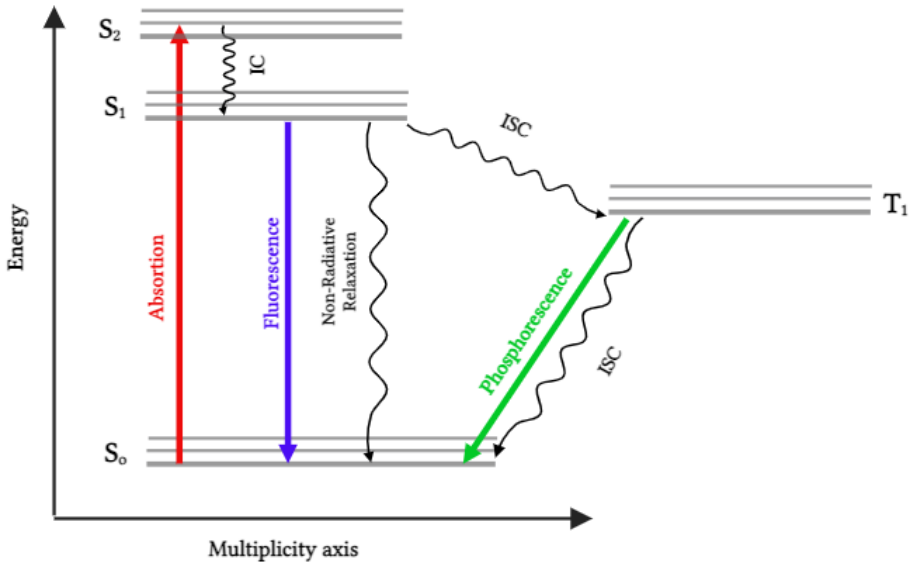

Figure 1.2.1. Jablonski diagram. The four lines S_0, S_1, S_2, T_1 represent the relevant states and their vibrational energy states. Solid arrows show radiative processes such as absorption, fluorescence, and phosphorescence, while wavy arrows represent radiationless

processes, such as relaxation of a singlet state ($S_1 \rightarrow S_0$) without light emission, referred to as internal conversion (IC). Intersystem crossing (ISC) refers to a change of electron spin, for example, going from S_1 to T_1.

In the previous diagram, electrons are promoted from the highest occupied molecular orbital (HOMO) of a molecule to a singlet state (S_2). The electron is directly excited into a higher vibrational energy state of the first or second excited singlet state (S_1 and S_2 respectively). This higher vibrational energy state is denominated as LUMO which stands for Lowest unoccupied molecular orbital. When the electron relaxes from the S_2 state to the S_1 state, or from any higher vibrational energy state to a lower one, a radiationless process occurs and it is known as Internal Conversion (IC). This non-radiative decay process releases energy in the form of heat, and it is well-known as Kasha's rule.[7] This rule states that higher excited states (higher than S_1, such as S_2, S_3, and so on) undergo rapid relaxation to the lowest excited state, S_1, from where photochemical and photophysical phenomena, such as fluorescence, take place.[4] Both radiative processes, fluorescence, and phosphorescence, occur from excited states, the first one from the excited singlet state and the former from the excited triplet state (Please refer to Figure 1.2.1.). Fluorescence involves emission without a change in multiplicity whereas phosphorescence involves emission with a change in it.

On the other hand, Intersystem Crossing (ISC) can also occur. Still, in this instance, the transition happens between two states of different multiplicity, *e.g.*, from $T_1 \rightarrow S_0$ or $S_1 \rightarrow T_1$ and it involves an electronic spin change. This inversion of spin on an electron is a forbidden process that slows down this transition. In the context of photochemistry, "*forbidden*" indicates that while the process is unlikely to occur rapidly, it is not impossible. Even though some molecules such as benzophenone effectively execute this process, the generally low likelihood of this event happening often results in prolonged lifetimes in the triplet excited state, given the inability to return to the ground state without a spin flip.[8] Likewise, another concept to consider as part of this dissertation is the energy gap ($\Delta E_{S \rightarrow T}$) between these processes which helps to study the behaviour of the two excited states and the rate at which they switch between each other. For example, comparing these energy differences between different molecules provides insights into a wide range of

chemical processes in catalysis and redox chemistry. Figure 1.2.2 depicts these parameters for benzene[9] and benzophenone[4] which tells us that transitions with smaller energy differences may occur more rapidly than those with larger differences, and thus mechanistic insights into processes such as electron transfer can be obtained, besides underlying principles governing different photochemical reactions. Similarly, studying the lifetimes of various excited states, such as triplets, can enhance the understading of the dynamics of energy transfer, the efficiency of photochemical reactions and the stability of intermediate species involved in photochemical process.

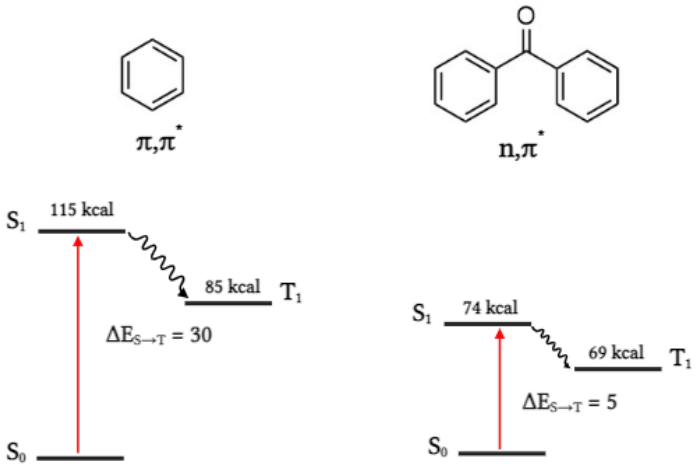

Figure 1.2.2. Jablonski Diagrams of $\Delta E_{S\rightarrow T}$ values for benzene and benzophenone. The energy values are in units of kcal/mol. Please note that both excited states of the molecules have different electronic configurations. Benzene exhibits a π,π* transition that involves the excitation of electrons from a bonding π orbital to an antibonding π* orbital while benzophenone shows an n, π^* transition that involves the promotion of an electron from a non-bonding orbital to an antibonding π^*orbital.

In fact, understanding the lifetimes of excited states when using organic molecules as photoactivated precursors for the rapid synthesis of nanostructures is a key concept that will be considered in Chapter 2. Considering Figure 1.2.2., after exciting with light, both molecules have a triplet excited state generated via ISC of their singlet states created after light absorption. However, there are other ways to produce this triplet excited state or even singlet processes in organic molecules, like for example, through sensitization. Senzitization is an energy transfer process that requires, for example, a triplet donor with

a higher excited triplet excited state than the acceptor. Spin state of the electrons is maintained during the sensitization process.[4] This is the case of the reaction depicted in Figure 1.2.3, wherein the benzophenone triplet state (T_1) is the triplet donor that will transfer energy to *cis*-pentadiene, which is an acceptor, leading to its triplet excited state and the ground state (S_0) of benzophenone.[10,11]

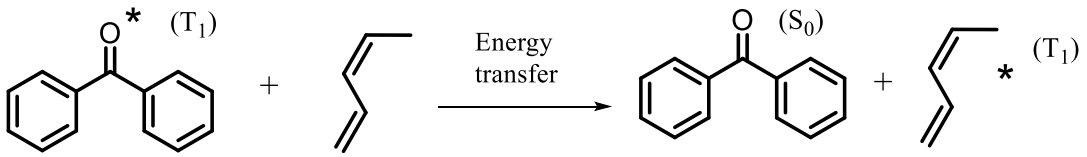

Figure 1.2.3. Sensitization process for *cis*-pentadiene. In this case, T_1 of benzophenone is being quenched by the *cis*-pentadiene and for the diene, it is a sensitization process because of the energy transfer process between T_1 of benzophenone to the ground state of the diene. This allows the formation of a new excited state (T_1) of the acceptor (pentadiene). Please note that the acceptor excited state should have lower energy than the donor, this is crucial for sensitization to be effective.[4] Following energy transfer the excited diene can relax to both *cis* and *trans* ground states.

Besides the above , there are additional tools for the study of photochemical reaction mechanisms like quenching of excited states, Stern-Volmer plots for data analysis, and laser flash photolysis. All of these topics will be covered in Chapter 2, except for the last one, which will be presented separately as a subsection in the current chapter. Additionally, understanding photochemistry is increasingly linked to the use of nanomaterials, which possess unique properties that enhance light-matter interactions. Nanomaterials will be explained in the following section.

1.3. Nanomaterials

Nanomaterials are defined as materials with sizes less than 100 nanometers[12] (Figure 1.3.1). These materials show different physicochemical properties than bulk materials which are influenced by their size and shape. Interestingly, tailoring these properties of nanomaterials at the nanoscale level yields different features and functionalities, offering novel opportunities for exploration and development.

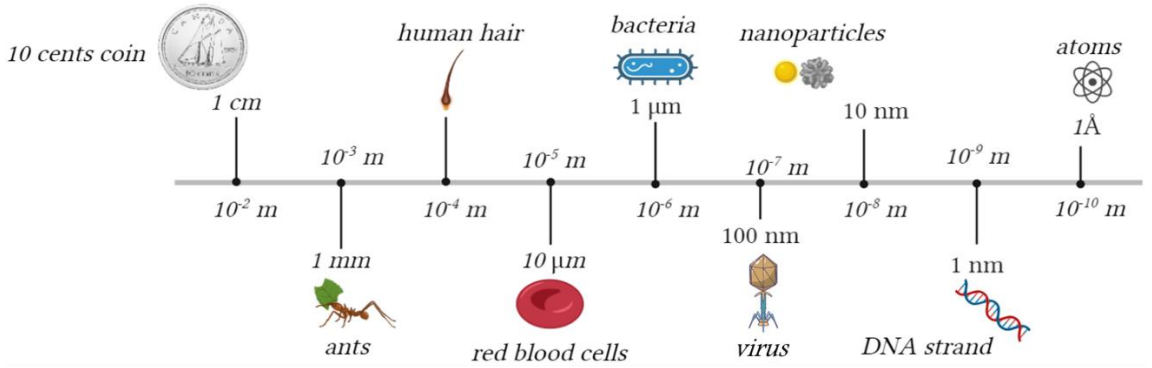

Figure 1.3.1. Different substances in the length scale from 1 cm to 1Å. This image offers a frame of reference for the reader. The data of the figure was taken from different references.[13, 14, 15]

For example, the colour of colloidal silver (Ag) nanoparticles can be yellow, orange, or green depending on the shape and size, which can be explained by localized surface plasmon resonance (LSPR), that refers to the collective oscillation of electrons at the interface of mettalic structures, which occurs when these electrons interact with incident light of a specific wavelength.[16, 17] This collective oscillation of electrons also occurs in the case for gold (Au). Apart from colour, the specific surface area of nanomaterials is significantly larger compared to the corresponding bulk material. Indeed, nanomaterials possess a large fraction of surface atoms per unit volume.[18] This is attributed to an increase in the ratio of the surface atoms to interior atoms. Therefore, materials made up of nanoparticles have relatively larger surface area when compared to the same volume of material made up of bigger particles, which implies that nanomaterials contain a higher number of reactive sites compared to bulk materials and thus, this is one of the reasons why these materials have a great potential for the field of catalysis.

Besides the above, nanomaterials are characterized by having great surface energy, and thus they exhibit high reactivity. This high surface energy comes from the large number of surface atoms relative to the total number of atoms, giving surface atoms a greater tendency to interact with their environment.This can be attributed to the unique electronic structure and abundance of surface atoms in nanomaterials. Consequently, nanomaterials

have gained attention as promising heterogeneous catalysts, thanks to their high surface area-to-volume ratio.[18]

Nanoparticles can be synthesized chemically, biologically,[19] through a photochemical approach, among other synthesis processes. The photochemical approach is the preferred option in this dissertation. In Chapter II a photoactivated precursor such as a substituted aromatic tetralone is used, while in Chapter IV, the benzoin Irgacure 2959 (I-2959) is utilized. In both cases, the light source is UVA light and a ketyl radical is formed in the process. As an illustration, Figure 1.3.2 depicts the rapid Norrish Type I cleavage[4, 20] that I-2959 undergoes.

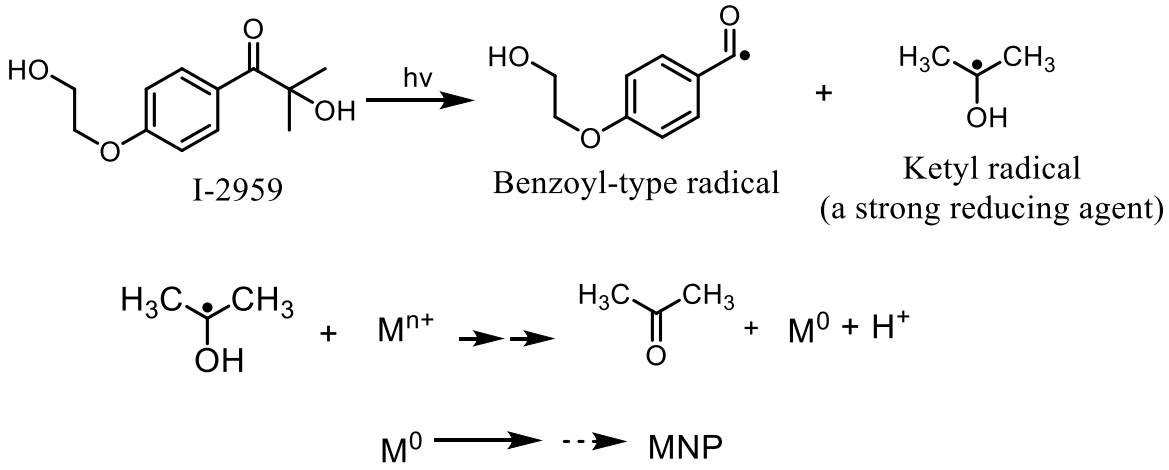

Figure 1.3. 2. Photocleavage of the Benzoin I-2959 under UV irradiation. In this reaction, ketyl radicals are generated and they can be defined as a "*caged electron*"[20] and in the presence of suitable acceptors, such as metal ions, is ready to deliver an electron, leading to the synthesis of metal nanoparticles (MNPs), such as Au, Cu, Ag, by reducing the metal ion.

In this instance, the triplet excited state of I-2959 has a short lifetime (~10 ns)[21] and it is unlikely to be quenched by metal ions in solution. This short lifetime ensures efficient radical generation and trapping and this is the reason why the versatility of ketyl radical mediated MNP has been examined within our group along the radical reduction process and the mechanism of this photochemical reaction.[22, 23, 24] In addition to this, a key benefit of producing heterogeneous nanoparticle systems is the easy removal and reusability processes following their use in different photochemical reactions. All these features

ensure a promising future for the application of nanomaterials. Moreover, due to their potential applications in emerging areas of nanoscience and technology, size, shape, and surface morphology play an important role in controlling the physical, chemical, optical, and electronic properties [25] of these nanoparticles. In this dissertation, the synthesis of nanoparticles is typically done in solution under UVA irradiation using a photoactivated precursor and usually involves the reduction of metal salts to atomic states that form particles. However, there are other ways of making nanostructures like these, for example, sol-gel chemistry,[26] hydrothermal chemistry,[27] ion-exchange chemistry,[28] and thermal synthesis, among others. Due to the high surface energy and reactivity of the nanoparticles, aggregation might occur unless their surfaces are protected or passivated. For example, in thermal synthesis, a common method to avoid aggregation is using self-assembled monolayers with thiol-functionalized organics,[25, 29] or using capping agents using polymeric matrices.[30] Furthermore, the use of trisodium citrate[31, 32,33, 34] ($Na_3C_6H_5O_7$) is also an alternative that leads to monodisperse nanoparticles as it aims to control the growth and formation of the NPs and it can be easily substituted if desired. Specifically, $Na_3C_6H_5O_7$ species are attached to the surface of the NPs and serve as nucleation centers for the NPs growth, avoiding agglomeration at the same time.[35] Basically, stabilizing agents control the nucleation, growth, and stabilization of the synthesis process. This will be discussed in more detail in Chapter II which involves MNPs.

When talking about noble MNPs, once they form, it is possible to identify the nanostructures by observing a change in colour in the solution, or by also monitoring a plasmon band using Ultraviolet-Visible spectroscopy (UV-Vis). This absorption profile gives information about the size of the NPs, the visually observed colour, and even if there is an agglomeration of the nanostructures. All of these perceptible characteristics are due to the localized surface plasmon resonance (LSPR) effect. LSPR is produced by metal nanoparticles, usually gold or silver, and shows a strong absorption band in the UV-Vis region. LSPR depends on the metal, particle size, shape, interparticle distance, temperature, and the environment where the NPs are synthesized. It is an optical phenomenon generated by a light wave trapped within conductive NPs smaller than the wavelength of light. This phenomenon involves surface plasmon resonance wherein the electric field from incident

light can stimulate electrons in a conduction band (CB), leading to localized plasmon oscillations with resonant frequency.[36] Actually, variations in particle geometry result in a shift in surface electron density, leading to alterations in oscillation frequency and this can be analyzed in the absorption band. Accordingly, LSPR is based on multiple factors, as mentioned before, and notably changes in nanoparticle geometry and shape induce shifts in surface electron density, thus altering the oscillation frequency, which could be detectable through changes in the absorption band. Analyzing these features is essential for understanding the potential applications of this phenomenon. Furthermore, it is worth noting that these changes in size and morphology can also be obtained when changing different conditions of the synthesis, *e.g.*, the irradiation frequency. For example, Scaiano and Stamplescoskie[22] published a facile method for the preparation of silver nanoparticles (AgNPs) of different sizes and morphologies by choosing the desired optical properties and irradiating spherical AgNP seeds with a specific light-emitting diode to control these features. Figure 1.3.3. shows a representation of this scientific report to show how the spherical AgNP seeds were transformed into other shapes.

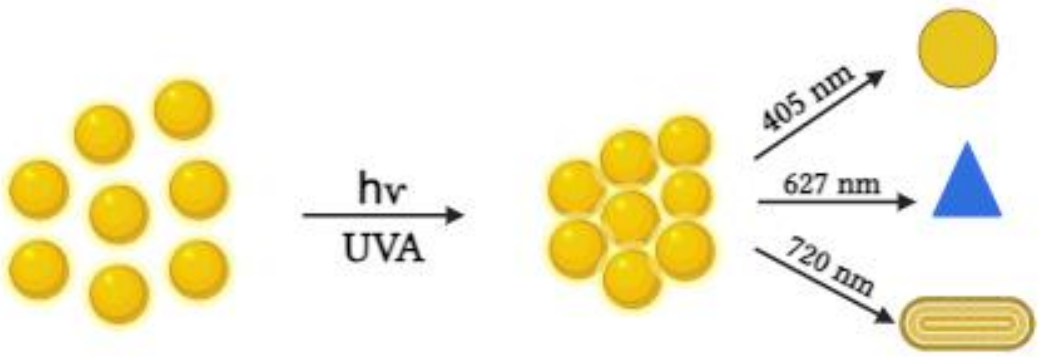

Figure 1.3.3. Transformation of AgNP seeds.

For example, from the previously mentioned publication,[22] for spherical AgNPs the plasmon peak is about 400 nm and the size is usually around 10 nm, but upon 405 nm irradiation, even though the spherical shape is conserved, the rate of growth decreases as the particles coalesce at longer times. On the other hand, the irradiation of AgNP seeds with 627 nm light led to platelets with a plasmon peak of around ~690 nm. Something similar happens to gold NPs (AuNPs) which display a plasmon peak with a maximum of

530 nm when they are nanospheres,[37] but of ~700 nm when their shape is rods.[38] Therefore, it is essential to understand parameters such as aspect ratio, concentration, and aggregation level to determine the optical and chemical properties of the NPs. As a matter of fact, UV-Vis spectroscopy is a useful technique and through the absorption spectra of these nanoparticles is possible to gain insights into these features. These nanostructures are often characterized by techniques such as Transmission Electron Microscopy (TEM), Scanning Electron Microscopy (SEM), and Atomic Force Microscopy (AFM) to confirm their size/size distribution and shape. Some of these techniques have been used when characterizing the nanostructures disclosed in this dissertation.

1.4. Heterogeneous Metal-Nanoparticle Decorated Titanium Dioxide

Heterogeneous photocatalysts are materials suspended in a reaction solution instead of being homogeneously dissolved in it. The interest of photocatalysis has focused on the use of semiconductor materials as photocatalysts for different applications. This photoactive semiconductor absorbs light to induce oxidation and reduction reactions on its surface[39] and this is the reason for using these materials for the removal of organic and inorganic species from aqueous or gas phase systems in environmental clean-up, drinking water treatment, and health applications.[40] In the context of history and research, in 1972 Fujishima and Honda[41] discovered the photochemical separation of water into hydrogen and oxygen in the presence of the semiconductor TiO_2. Actually, among the various photocatalysts, TiO_2, is the most widely employed semiconductor and it has been largely used in heterogeneous photocatalysis, due to its chemical stability, nontoxicity, and low cost.[42] Semiconductors, by definition, are materials that fall between insulators and conductors in their electronic properties. Semiconductors are characterized by an energy gap between the valence band (VB), which is the highest occupied energy level, and the CB. This energy gap is often referred to as the band gap of the semiconductor that is between these bands.[43] As indicated in Figure 1.4.1a, the activation of the semiconductor photocatalysts is achieved through the absorption of a photon which results in the promotion of an electron (e^-) from the VB to the CB, with the subsequent generation of a hole (h^+) in the valence band. After these charge carriers are generated, they can recombine,

either emitting light or releasing heat as the e^- returns to the energy of the valence band. Nevertheless, charge carriers can migrate toward the surface where they can be trapped in surface sites, or within the bulk of the material. These trap sites tend to involve defects in the crystal lattice of the semiconductor and they are usually in the surface. These trapped charge carriers exhibit slower recombination rates, typically occurring within the nanosecond range rather than picoseconds.[44, 45] When these charge carriers are trapped at the surface, they can be involved in different redox reactions with compounds present in the surrounding solution, and specifically, h^+ serves as potent electron acceptors and e^- acts as electron donors as shown in Figure 1.4.1a.

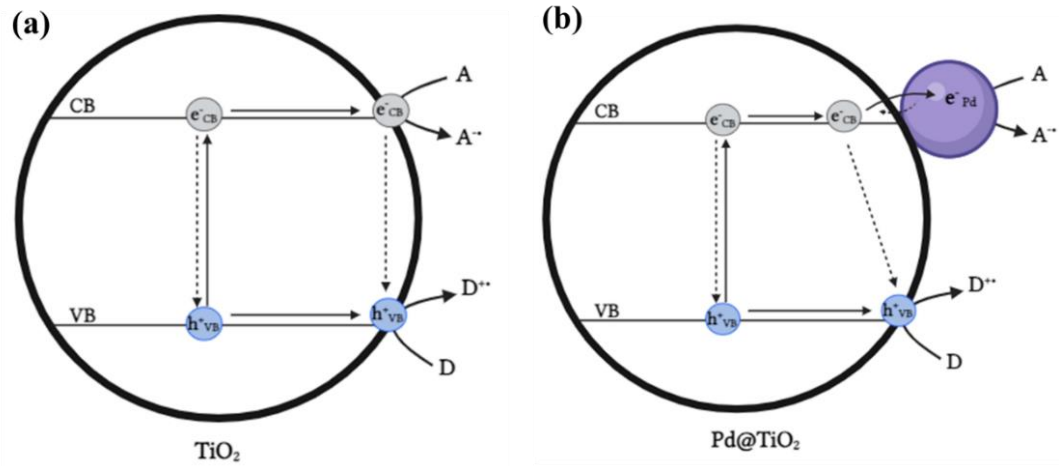

Figure 1.4.1. The fate of charge carriers generated after light excitation of semiconductors particles for (a) bare TiO_2 and (b) PdNP-decorated TiO_2. Note that A is an electron acceptor and D is an electron donor. Dashed lines represent the recombination of the photo-generated e^-- h^+ pair which occurs with the release of heat.

In the case of bare TiO_2 as a photocatalyst, it has a large band gap of ~3.2 eV and thus it only can absorb UV light (<400 nm) and as represented in Figure 1.4.1a, the charge carriers can recombine. Accordingly, to avoid said fast recombination, several strategies have been applied to modify the band gap energy, including decorating the surface of the semiconductor with NP or through doping. Specifically, decorating TiO_2 with metal or metal or metal oxide nanoparticles is a process that adds superficial modifications to the

TiO_2 surface. Nanoparticles supported on the surface of TiO_2 often fall within the 1-10 nm size range. As depicted in Figure 1.4.1b, the metal acts as an electron trap, which reduces the rate of recombination by facilitating the transfer of the excited e^- into the CB into the MNP.[45] In the case of Pd@TiO_2, in this dissertation, PdNP is synthesized by reduction of Pd^{+2} to Pd^0 under UVA irradiation in the presence of TiO_2 and its synthesis does not require an organic ligand/reductant that could arrest particle growth and maximizes the available NP surface.[46] In this case, TiO_2 can directly reduce the metal through photoexcitation with UV light. However, for metals such as copper (Cu) and Ag, a photoinitiator, is used to more readily reduce the metal. As mentioned in section 1.3 Nanomaterials of this dissertation, I-2959 is frequently used for this purpose. Given the reducing strength of the ketyl radical generated after irradiation of I-2959, it is possible to reduce the metal ion to an oxidation state of zero, thus leading to the NP formation on the TiO_2 surface. Hence, the decoration process is a common strategy to increase the lifetime of the charge carriers in TiO_2. Moreover, decorating the TiO_2 surface with noble transition metals like Pd or Au, shifts the absorption spectrum of the semiconductor *per se* towards the visible region creating visible light-induced e^- - h^+ pairs.[47,48] In fact, while Pd NP decorated TiO_2 does not show strong absorption in the visible region, plasmonic Au-decorated TiO_2 does. Therefore, it is true that the addition of NP onto the surface of TiO_2 facilitates the photocatalytic organic reactions of any absorbed molecule at ambient or moderate temperatures.[49]

Additionally, irrespective of the mechanism behind any photocatalytic organic reaction, there is a correlation between the rate of reaction and light intensity. As the incident light intensity increases, more electrons occupy higher levels which boots the photocatalytic performance of the heterogeneous material. This enhancement is due to the transfer of electrons to reactant molecules, facilitated by the abundance of these carriers.[50,51] Likewise, metal oxide NP can also decorate the surface of TiO_2, as is the case of CuO. Metal oxide particles often display changes in oxidation state over time from certain reactions, sometimes playing an integral role in the chemistry occurring. Our research group has demonstrated the above-mentioned for CuO_x@TiO_2 photocatalysts in copper-click chemistry, where atmospheric conditions are necessary for the regeneration

of active sites on the NP surface. The active form is Cu(I), with interconversion among Cu(0), Cu(I) and Cu (II). TiO_2 helps to reduce it when it is too oxidized, and oxygen helps to oxidize it when it is too reduced.[52] Consequently, both metallic NP and metal oxide NP supported on TiO_2 present promising alternatives for enhancing catalyst performance. Their catalytic activity, stability, and cost-effectiveness make them attractive candidates for different reactions. Furthermore, understanding the mechanistic insights and synergic effects between the NP and TiO_2 can further optimize their performance.

On the other hand, the doping process also helps with the idea of extending the wavelength range of the photoactivation of TiO_2 photocatalysts towards the visible light region and improving the use of solar energy. This process involves the direct addition of the element into the crystal structure of the material due to the introduction of additional energy levels into the TiO_2 structure, allowing more carriers to diffuse to the surface. As a result, this process modifies the TiO_2 bandgap and reduces the rate of recombination of the photogenerated carriers.[53] Nonetheless, even though other processes help with this goal, in this dissertation decoration of TiO_2 with different metals is the preferred one and it will be described in Chapters IV and V.

1.5. Laser Flash Photolysis

Laser Flash Photolysis (LFP) is a well-known technique that uses a pulsed laser as the source to study events in chemical reactions that have a duration of nanoseconds to milliseconds. Specifically, this technique studies the transient absorption of chemical species generated after the short but intense pulse from the pulse laser source. Flash photolysis was developed by George Porter and Ronald Norrish to study the short-lived intermediates in photoinduced reactions in 1949. To the best of our knowledge, in 1960, Lindqvist was able to detect the triplet state of acridine,[54] with a modified laser technique. Nowadays, nanosecond LFP has become a widely used tool for kinetic studies. Despite advancements in the components originally utilized by Lindqvist over 64 years ago, the system has remained unchanged. Such was the impact of this technique that Porter and Norrish won the Nobel Prize for this in 1967 and its use was reported by different scientists, such as Worral et al.[55] The typical setup is depicted in Figure 1.5.1., basically, the sample

is excited with a laser pulse and thus the change in absorbance (ΔOD) over time (μs) is measured by a probe beam. Specifically, the probe beam passes through the sample in a perpendicular direction to the one of the laser pulse and then passes through a monochromator which selects the desired detection wavelength to monitor the transient species. This signal enters into a photomultiplier tube (PMT) which amplifies a signal into an electrical current for detection and passes through an oscilloscope which graphically displays varying voltages of one or more signals as a function of time, giving the plot shown in Figure 1.5.1. These changes in absorbance are from the transient species created in the samples after laser excitation and the formation of a decay or a growth signal can be monitored with this time-resolved technique. These absorbance spectra allow for insights into the structure and lifetimes of the generated species. This particular technique was used in Chapters II, III, and VI to learn more about the photochemistry of different molecules and to monitor biradicals as photoinitiators for the synthesis of nanostructures and boryl radicals as effective hydrogen abstractors.

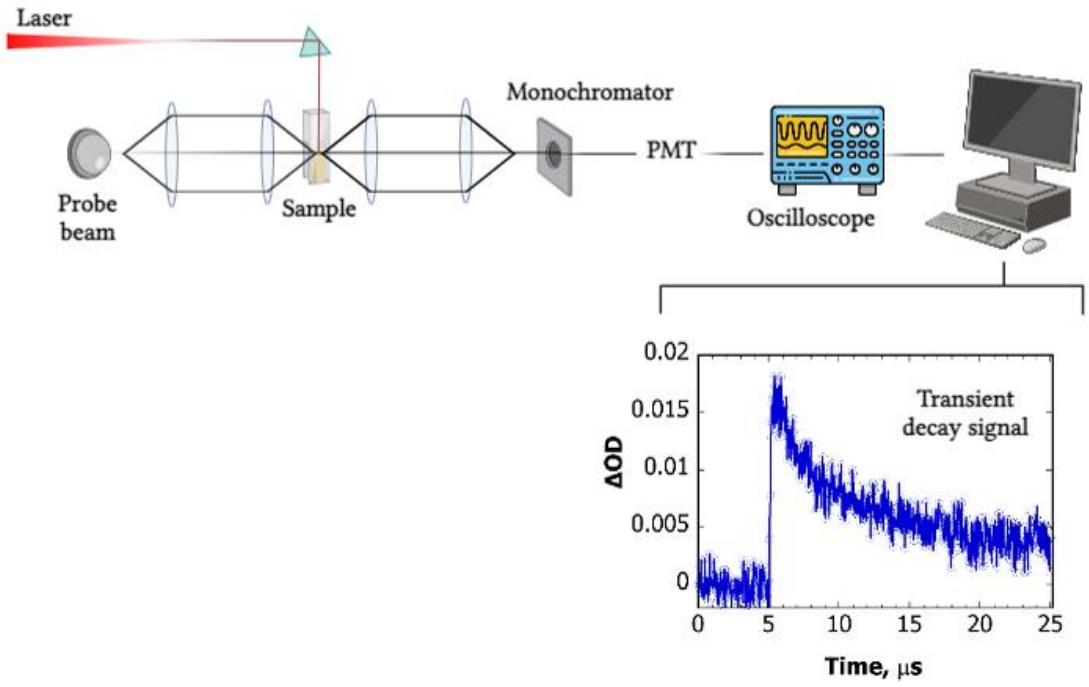

Figure 1.5.1. Typical optical setup for laser flash photolysis.

There are different lasers and wavelengths for this technique, as mentioned by Scaiano[56] and represented in Table 1.5.1., the solid-state lasers, such as neodymium-doped yttrium aluminum garnet (Nd/YAG) are very useful given the harmonics generated from the fundamental wavelength of 1064 nm, by frequency doubling into 532 nm or frequency tripling into 355 nm.[57] This provides a valuable array of effective excitation wavelengths to use, with the 355 nm harmonic being utilized in this dissertation. There are different durations of the laser pulse which limits the timescales that can be evaluated.[58] For example, there are nano, femto, and picosecond LFP techniques, wherein the nanosecond LFP is the most adequate for the study of different photochemical systems.

In the last few years, laser techniques have become available and attractive to organic chemistry. For example, in 1982 1,4-biradicals were monitored as intermediate species in the Norrish type II reaction and the photoenolization of *o*-alkyl-substituted carbonyl compounds.[56] Specifically, by using a nitrogen laser that produces a 337 nm pulses and a duration of ~8 ns, biradicals and photo-enols of different molecules were studied to prove that LFP technique was extremely useful in determining lifetimes of these species in different solvents, absolute rates of hydrogen abstraction by the radicals and also rate constants of various electron acceptors with these radicals.

Table 1.5.1. Typical lasers used in LFP. Information reproduced from Scaiano, J. C., Nanosecond Laser Flash Photolysis: A Tool for Physical Organic Chemistry. In Reactive Intermediate Chemistry, John Wiley & Sons: 2003; pp 847-871.

Laser	Fundamental (nm)	Harmonics (nm)
Nitrogen	337	N/A
Excimer	157	N/A
	193	
	248	
	308	

	351	
Ruby	694	347
Nd/YAG	1064	532, 355, 266

In the previous scenario, the reaction intermediates (biradicals) produce a signal within the accessible spectral range, but there are some cases in which no signal is provided. This is the case of the reaction of *tert*-butoxyl with aromatic alcohols, which will be further discussed in this dissertation and is shown in Figure 1.5.2. Later in the 1970s the technique called "*the probe method*"[59] was introduced and is useful when some of the products or intermediate species are "invisible" to the nanosecond LFP. Therefore, LFP is essential when studying chemical reactions, their mechanisms, kinetics, and pathways that help to understand the chemistry behind several processes. Further elaboration on this topic will be provided within the document.

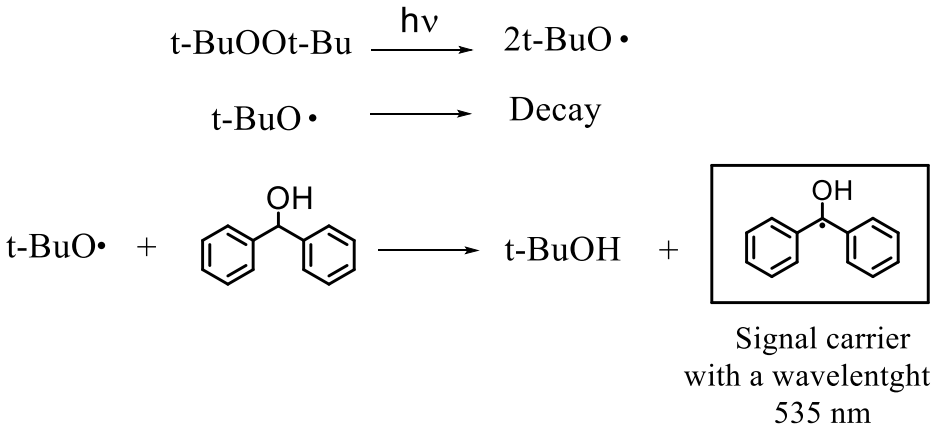

Figure 1.5.2. The probe method: mechanism between the tert-butoxyl radical and diphenylmethanol using a 355 nm laser pulse. The radical produced by hydrogen abstraction can be detected quite easily at 535 nm. The mechanism assumes that the decay of the t-butoxy radical is a pseudo-first-order process. Likewise, the signal carrier being a ketyl radical is regarded as a stable species in this time scale.[59]

1.6. Thesis contents outline

The goal of this dissertation is to show a multifaceted photocatalytic exploration of a variety of different chemical applications. This will start with Chapter II directed to the photoenolization process of substituted tetralone as a convenient driver for the synthesis of AuNP. Specifically, the photochemistry of this molecule is studied including the excited states of the ketone and the enol, in which the triplet excited state of the enol serves to lead to a fast synthesis of gold nanostructures. In the case of excited photoenols like this one, the advantage is that if the metal ion trapping fails, the species return to the original ketone precursor and remain available for future events, and lead to the nanoparticles. Likewise, this chapter includes the study of different energy transfer processes including the monitoring of singlet oxygen which quenches the excited triplet state of the enol and the quenching of the triplet excited state of the ketone (the precursor of the excited triplet state of the enol) using 1,3-pentadiene. Furthermore, electron transfer processes were also studied using $HAuCl_4$ and methyl viologen dichloride hydrate ($C_{12}H_{14}Cl_2N_2 \cdot xH_2O$) which helped to determine different rate constants associated with these reactions.

Chapter III describes the α-lipoic acid photochemistry to control the synthesis of plasmonic nanostructures. Explicitly, we focus on a novel approach to produce a cross-linked polymeric matrix of lipoic acid monomers (named PALA in this dissertation) through the photopolymerization of lipoic acid (LA). This method helps to control the size of plasmonic AuNP when using the same substituted tetralone described in Chapter II, as the photoinitiator for the reduction of Au (III) to Au(0). Additionally, the synthesized polymer (with a length between 5-6 monomers of LA) is characterized through Dynamic Light Scatering (DLS) and Gel Permeation Chromatography (GPC). The dual behaviour of LA as both: an in-situ stabilizer and reducing agent is also explored, thus, the results help us understand the photochemical transformation of LA expanding the use of it and its polymer in the synthesis of nanomaterials.

On the other hand, Chapter IV explores the semi-hydrogenation reaction of alkynes, including a scope of 4 compounds and testing 3 main photocatalysts: $Pd@TiO_2$, $Cu@TiO_2$, and a bimetallic catalyst $PdCu@TiO_2$ which was synthesized via galvanic replacement

synthesis. It is worth mentioning that the real challenge in semi-hydrogenation processes is to avoid over-hydrogenation to the saturated alkane moiety, and thus reaching a critical time in which the reaction should be stopped. The reality of the organic chemistry laboratory is that reaction times must be somewhat forgiving, as their times are measured in hours and sometimes overnight, and on rare occasions on continuous real-time monitoring of the reaction mixture composition. Therefore, semi-hydrogenation of alkynes can be a challenging process, as one would like to combine reasonable activity with high selectivity. Besides the characterization of the catalysts, we investigated the adsorption capacity of the materials after being in contact with alkyne solutions in ethanol (EtOH) and methanol (EtOH) for 40 min. We also evaluated the effectiveness of the solvents as hydrogen donors in the reaction and the kinetics of the semi-hydrogenation process using UVA light irradiation. In the case of Pd@TiO_2, the reaction was fast but the selectivity was <1% at twice the time for 95% conversion of the alkyne. In contrast, Cu@TiO_2 and CuPd@TiO_2 offered excellent selectivity without critical timing requirements. The latter was about 52% faster than Cu@TiO_2 and to our surprise, not only preserved the selectivity but also offered a small improvement. This will be further discussed in detail in Chapter IV.

Chapter V is directed to the synthesis of Schiff bases from benzyl alcohol and nitro compounds under UVA irradiation, using different catalysts including TiO_2, Pd@TiO_2, Cu@TiO_2, and Fe_3O_4@TiO_2, with Fe_3O_4@TiO_2 demonstrating great efficiency. Schiff bases are essential organic compounds widely used across many fields, traditionally formed via condensation of primary amines and carbonyl compounds, a process typically demanding high energy and leading to environmental risks. Catalysts often incorporate metals like Pd, which are under depletion, and thus the exploration of alternatives such as the magnetic Fe_3O_4@TiO_2 catalyst detailed herein was explored. The reactions were performed by using 0.1 M nitrobenzene in benzyl alcohol under UVA light (λ=369 nm) and N_2 for 3, 6, and 20 hours. Results indicate that after 3 hours of irradiation, Pd@TiO_2 achieved 26.9 mmol (27%) of N-Benzylideneaniline but also significant undesired hydrogenation of the Schiff base, while TiO_2 reached 28.7 mmol Schiff base. Cu@TiO_2 and Fe_3O_4@TiO_2 yielded 15.3 mmol and 18 mmol respectively. Initially, Fe_3O_4@TiO_2

showed delayed catalytic onset but superior long-term performance, producing 41.7 mmol at 6 hours and 99% conversion at 20 hours, a milestone for magnetic catalysts in this application. This chapter presents a novel approach that uses a magnetic catalyst with improved features such as its easy separation and its efficiency in the synthesis of Schiff bases, making a great contribution to catalysis research. In Chapter VI, this dissertation explores the future directions of the studies discussed in previous chapters, along with conclusions, highlighting the importance of these projects. Additionally, it introduces a new area of research related to polarity reversal catalysis, which facilitates slow or ineffective reactions, caused by unfavorable interactions between radicals and substrates. This chapter provides a brief overview of initial results in this emerging field, opening the door for future research in this area.

1.7. References

1. M. Cely-Pinto and J. C. Scaiano, *Photochemical and Photobiological Sciences*, 2021, **20**, 1611–1619.
2. M. Cely-Pinto, B. Wang and J. C. Scaiano, *Photochemical and Photobiological Sciences*, 2023, **22**, 1299–1307.
3. M. Cely-Pinto, B. Wang and J. C. Scaiano, *Nanomaterials*, 2023, **13**, 2390.
4. J. C. Scaiano, *Photochemistry essentials*, American Chemical Society, 2022.
5. J. C. Scaiano, *Chemical Society Reviews*, 2023, **52**, 6330–6343.
6. Nicholas J. Turro and Angelo A. Lamola, *The Science of Photobiology*, 1977.
7. M. Kasha, *Discussions of the Faraday Society*, 1950, **9**, 14-19.
8. C. M. Marian, *Wiley Interdisciplinary Reviews: Computational Molecular Science*, 2012, **2**, 187–203.
9. B. Hajgató, D. Szieberth, P. Geerlings, F. De Proft and M. S. Deleuze, *Journal of Chemical Physics*, 2009, 131, 224321.
10. M. Bigwood and S. Boué, *Bulletin des Sociétés Chimiques Belges*, 1973, **82**, 685–691.
11. Peter A. Leermakers and George F. Vesley, *Journal of Chemical Education*, 1964, **41**, 535–541.
12. L. A. Kolahalam, I. V. Kasi Viswanath, B. S. Diwakar, B. Govindh, V. Reddy and Y. L. N. Murthy, in *Materials Today: Proceedings*, 2019, **18**, 2182–2190.
13. B. Ward, PhD Thesis, Arenberg Doctoral School, Faculty of Science, 2014.

14. M. Bloemen, PhD Thesis, KU Leuven, Faculty of Science , 2015.
15. T. Roy and A. Kumar Chakraborty, *Insights in Biomedicine*, 2016, **1**, 1-10.
16. Y. Sun and Y. Xia, *Analyst*, 2003, **128**, 686–691.
17. A. L. González, C. Noguez, J. Beránek and A. S. Barnard, *Journal of Physical Chemistry C*, 2014, **118**, 9128–9136.
18. A. B. Asha and R. Narain, *Polymer Science and Nanotechnology: Fundamentals and Applications*, Elsevier, 2020, 343–359.
19. S. Hasan, *Research Journal of Recent Sciences*, 2015, **4**, 9-11.
20. J. C. Scaiano, K. G. Stamplecoskie and G. L. Hallett-Tapley, *Chemical Communications*, 2012, **48**, 4798–4808.
21. K. L. McGilvray, M. R. Decan, D. Wang and J. C. Scaiano, *Journal of the American Chemical Society*, 2006, **128**, 15980–15981.
22. K. G. Stamplecoskie and J. C. Scaiano, *Journal of the American Chemical Society*, 2010, **132**, 1825–1827.
23. C. R. Bourgonje, D. R. C. da Silva, E. McIlroy, N. D. Calvert, A. J. Shuhendler and J. C. Scaiano, *Journal of Materials Chemistry B*, 2023, **11**, 6114–6122.
24. M. Yaghmaei, C. R. Bourgonje and J. C. Scaiano, *Molecules*, **28**, 4445–4460.
25. P. Raveendran, J. Fu and S. L. Wallen, *Journal of the American Chemical Society*, 2003, **125**, 13940–13941.
26. M. Parashar, V. K. Shukla and R. Singh, *Journal of Materials Science: Materials in Electronics*, 2020, **31**, 3729–3749.
27. T. J. Daou, G. Pourroy, S. Bégin-Colin, J. M. Grenèche, C. Ulhaq-Bouillet, P. Legaré, P. Bernhardt, C. Leuvrey and G. Rogez, *Chemistry of Materials*, 2006, **18**, 4399–4404.
28. S. Zhang, J. Li, X. Wang, Y. Huang, M. Zeng and J. Xu, *ACS Applied Materials & Interfaces*, 2014, **6**, 22116–22125.
29. J. P. Vanegas, J. C. Scaiano and A. E. Lanterna, *Langmuir*, 2017, **33**, 12149–12154.
30. M. K. Corbierre, N. S. Cameron, M. Sutton, S. G. J. Mochrie, L. B. Lurio, A. Rühm and R. B. Lennox, *Journal of the American Chemical Society*, 2001, **123**, 10411–10412.
31. K. L. McGilvray, C. Fasciani, C. J. Bueno-Alejo, R. Schwartz-Narbonne and J. C. Scaiano, *Langmuir*, 2012, **28**, 16148–16155.
32. J. C. Scaiano, P. Billone, C. M. Gonzalez, L. Maretti, M. L. Marin, K. L. McGilvray and N. Yuan, *Pure and Applied Chemistry*, 2009, **81**, 635–647.

33. P. S. Yerragopu, S. Hiregoudar, U. Nidoni, K. T. Ramappa, A. G. Sreenivas and S. R. Doddagoudar, *International Research Journal Pure and Applied Chemistry*, 2020, **21**, 37–50.
34. K. Ranoszek-Soliwoda, E. Tomaszewska, E. Socha, P. Krzyczmonik, A. Ignaczak, P. Orlowski, M. Krzyzowska, G. Celichowski and J. Grobelny, *Journal of Nanoparticle Research*, , 2017, **19**, .273.
35. Z. Zhang, H. Chen, C. Xing, M. Guo, F. Xu, X. Wang, H. J. Gruber, B. Zhang and J. Tang, *Nano Research*, 2011, **4**, 599–611.
36. E. Petryayeva and U. J. Krull, *Analytica Chimica Acta*, 2011, **706**, 8–24.
37 M. L. Marin, K. L. McGilvray and J. C. Scaiano, *Journal of the American Chemical Society*, 2008, **130**, 16572–16584.
38. R. Kumar, L. Binetti, T. H. Nguyen, L. S. M. Alwis, A. Agrawal, T. Sun and K. T. V. Grattan, *Scientific Reports*, 2019, **9**, 17469.
39. M. A. Fox and M. T. Dulay, *Heterogeneous Photocatalysis*, 1993, **93**, 341–357.
40. A. O. Ibhadon and P. Fitzpatrick, *Catalysts*, 2013, **3**, 189–218.
41. A. Fujishima, K. Honda, *Nature*, 1972, **43**, 37–38.
42. Q. Guo, C. Zhou, Z. Ma and X. Yang, *Advanced Materials*, 2019, **31**, 1901997.
43. A. Mills and S. Le Hunte, *An overview of semiconductor photocatalysis*, 1997, **108**, 1–35.
44. S. T. Martin, H. Herrmann, W. Choi and M. R. Hoffmann, *Journal of the Chemical Society, Faraday Transactions*, 1994, **21**, 3315–3322.
45. V. Subramanian, E. E. Wolf and P. V. Kamat, *Journal of the American Chemical Society*, 2004, **126**, 4943–4950.
46. A. Elhage, A. E. Lanterna and J. C. Scaiano, *ACS Catalysis*, 2017, **7**, 250–255.
47. A. Elhage, A. E. Lanterna and J. C. Scaiano, *ACS Sustainable Chemistry & Engineering*, 2018, **6**, 1717-1722.
48. A. Elhage, A. E. Lanterna and J. C. Scaiano, *ACS Catalysis*, 2017, 7, 250–255.
49. X. Wu, E. Jaatinen, S. Sarina and H. Y. Zhu, *Journal of Physics D: Applied Physics*, 2017, **50**, 283001.
50. S. Sarina, E. Jaatinen, Q. Xiao, Y. M. Huang, P. Christopher, J. C. Zhao and H. Y. Zhu, *Journal of Physical Chemistry Letters*, 2017, **8**, 2526–2534.
51. S. Sarina, H. Zhu, E. Jaatinen, Q. Xiao, H. Liu, J. Jia, C. Chen and J. Zhao, *Journal of the American Chemical Society*, 2013, **135**, 5793–5801.

52. B. Wang, J. Durantini, J. Nie, A. E. Lanterna and J. C. Scaiano, *Journal of the American Chemical Society*, 2016, **138**, 13127–13130.
53. F. Huang, A. Yan, and H. Zhao, in *Semiconductor Photocatalysis - Materials, Mechanisms and Applications*, InTech, 2016.
54. L. Lindqvist, *Comptes Rrendus Hebdomadaires des Séances de l'Académie des Sciences*, 1966, **263**, 852–854.
55. D. R. Worrall and S. L. Williams, *Encyclopedia of Modern Optics*, 2005, 31–38.
56. J. C. Scaiano, P.J. Wagner, *Journal of the American Chemical Society*, 1982, **15**, 4626–4627.
57. R. A. Moss, M. S. Platz and M. Jones, *Reactive Intermediate Chemistry*, Wiley, 2003.
58. D. J. Shields, M. Chakraborty, N. Abdelaziz, A. Duley and A. D. Gudmundsdottir, in *Photochemistry*, Royal Society of Chemistry, 2020, **47**, 70–121.
59. H. Paul, R. D. Small and J. C. Scaiano, *Journal of the American Chemical Society*, 1978, **100**, 4520–4527.
60. H. Wang, H. Liu, M. Wang, M. Huang, X. Shi, T. Wang, X. Cong, J. Yan and J. Wu, *iScience*, **24**, 2021, 102693.

2. Photoenolization as a convenient driver for the synthesis of plasmonic nanostructures

2.1. Preamble to chapter 2

Thischapter explores the process of photoenolization of a substituted tetralone such as 3,3,6,8-tetramethyl-1-tetralone when exposed to light. This transformation leads to the formation of a photoenol excited state, which is a highly energetic state that lasts for approximately 3 μs. This excited state arises from the carbonyl triplet state of its precursor, the ketone, which has a characteristic lifetime of about 1.9 ns. The main property of the photoenol excited state is that it exhibits a biradical character which makes it particularly valuable for the fast synthesis of gold nanostructures (AuNPs). In this case, the excited photoenol could be trapped by metal ions but if this process does not occur, it reverts to its original ketone form. This reversibility process ensures that the molecule (the substituted tetralone) remains available for future events that could lead to the formation of the desired nanoparticles. This dynamic behaviour highlights the versatility of substituted tetralones in this synthesis process.

Additionally, this chapter explores a detailed characterization of the photochemistry of substituted tetralones using LFP as the main technique. It was possible to understand the complex mechanism governing their transformation under UVA light exposure and the dual nature of the photoenol as a biradical and an excited state. This behaviour plays an important role in facilitating processes of energy and electron transfer which end up essential for the synthesis of AuNPs. Particularly, the tetralone used in this chapter is an efficient precursor for the photogeneration of AuNPs, offering the possibility of getting the nanostructures within minutes of exposure to UVA irradiation. This rapid synthesis process is facilitated by the presence of the biradical species involved in the photoenolization of the tetralone, wherein the ketyl moiety within the biradical acts as a potent reductant, driving the reduction of gold ions and facilitating the formation of AuNPs. However, in the absence of stabilizing agents during the synthesis, the resulting AuNPs exhibit agglomeration. Thus, to avoid this issue and enhance the spectral characteristics of the

resulting AuNPs, different concentrations of sodium citrate were used. Therefore, the use of tetralone as a precursor for the photogeneration of AuNPs offers a rapid and efficient synthesis route with precise control over spectral quality. This unique mechanism not only provides valuable insights into fundamental photochemical processes but also holds significant promise for advancing applications in nanotechnology and materials science.

2.2. Postprint Version of Manuscript

First published in Photochemical and Photobiological Sciences, **2021,** 20, 1611–1619

Abstract

Substituted tetralones such as 3,3,6,8-tetramethyl-1-tetralone undergo photoenolization to produce a photoenol excited state with a lifetime around ~ 3 μs, which involves the carbonyl triplet state of the ketone (τ ~ 1.9 ns), as a precursor; the excited photoenol also has biradical character and is useful for the fast synthesis of gold nanostructures. In the case of excited photoenols like this one, if metal ion trapping fails, they return to the original ketone precursor and remain available for future events that can lead to the target nanoparticles. This study includes the characterization of the photochemistry of the substituted tetralone, and the dual behaviour of reaction intermediates, as biradicals and excited states, in energy and electron transfer processes.

Introduction

The Norrish type II photoreaction of ketones is characterized by the abstraction of γ-hydrogens by excited carbonyl groups leading to biradicals that subsequently undergo fragmentation and cyclization reactions.[1] A similar reaction can take place in ortho-substituted aromatic ketones and is referred as photoenolization; the overall process is illustrated in scheme 2.2.1.

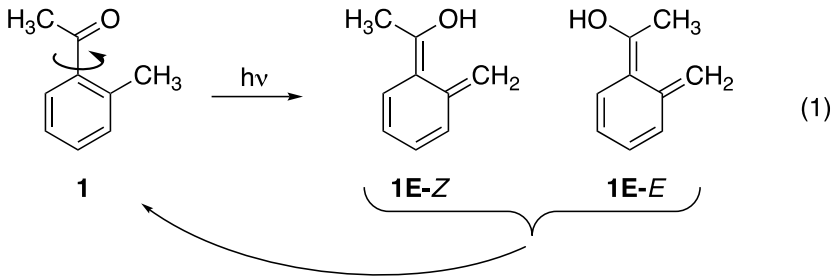

Scheme 2.2.1. General photoenolization process of 2-methylacetophenone, which produces 2 photoenols: *Z* and *E* isomers.

The reaction produces two photoenols with different lifetimes depending on the orientation of the O-H group relative to the CH_2 moiety. Under normal conditions both enols return to the original ketone precursor and the process has been proposed as a photostabilization strategy for polymers.[2] The reaction involves the carbonyl triplet state and is exceptionally fast, so much so, that hydrogen transfer is faster than bond rotation, and, as a result, molecules such as o-methylacetophenone have two distinct triplets, corresponding to the two rotamers, with the *Z* conformer being the one with the preferred orientation (as drawn in Scheme 2.2.1)[3] having the shorter triplet lifetime (~0.5 ns), while E conformer has a triplet lifetime of ~34 ns. If reducing triplet lifetimes is desirable, then tetralones (see Scheme 2.2.2) should be preferred, as the carbonyl group is locked in the most favorable orientation for H-transfer.[4] For example, the triplet state of **2** has a lifetime of 4.5 ns.[4]

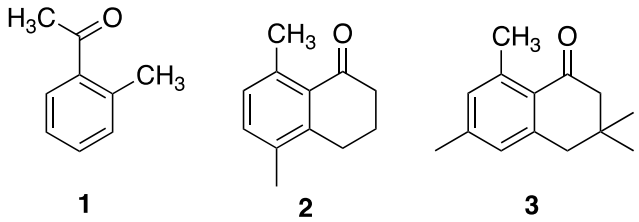

Scheme 2.2.2. Structures of representative photoenolizable ketones.

Just as in the case of the Norrish Type II reaction, photoenolizations involve a 1,4-biradical, as illustrated in scheme 2.2.3, but in fact the biradical is the same species as the triplet state of the photoenol;[5] the two are simply resonance structures.

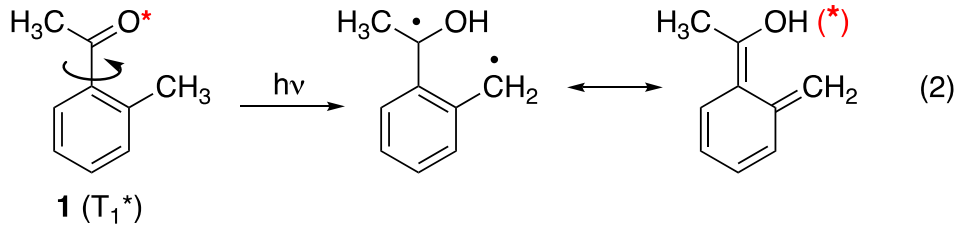

Scheme 2.2.3. Photoenolization process of 2-methylacetophenone after UV irradiation which produces 1,4-biradical that is the same species as the triplet state of the photoenol.

In the synthesis of plasmonic nanostructures, photochemistry can provide remarkable temporal and spatial control. In addition, adjustments of irradiance level can be used to control the reaction kinetics, frequently linked to the final nanostructure dimensions.[6] Unfortunately, transition metal ions are frequently efficient quenchers of excited states, sometimes leading to very long reaction times, reflecting attenuated quantum yields as a result of excited state quenching. The secret to a fast and efficient photochemical nanostructure synthesis rests on the generation of strong reductants from very short-lived excited states that can escape metal ion quenching. For example, Irgacure 2959 (I-2959), a substituted benzoin, generates ketyl radicals efficiently and mediated by a very short-lived (~11 ns) triplet state.[7, 8] As a result, excited triplet states largely escape quenching, and gold nanoparticles (AuNP) can be produced in minutes using conventional UVA light sources.[6]

Ketyl radical centers in monoradicals or biradicals can transfer electrons to a wide range of good electron acceptors, including oxygen, methyl viologen, and gold ions.[6, 9, 10] In this contribution, we explore the use of **3**, a commercially available tetralone, as a photoactivated precursor for the rapid synthesis of gold nanostructures. As part of this study we characterize in detail the photochemistry of **3**, and the dual behaviour of reaction intermediates in both, energy and electron transfer processes. In the case of other photochemical precursors (including I-2959), if the reducing free radicals are not trapped by the target metal ions, they normally proceed in secondary reactions to produce organic debris. In contrast, in the case of excited photoenols or biradicals, if metal ion trapping fails, the enols return to the original ketone precursor and remain available for future events that can lead to the target nanoparticles. A combination of bench scale synthesis, electron

microscopy, and laser flash photolysis delivers an intimate understanding of the applications of photoenolizable ketones as precursors for plasmonic nanostructures.

Results and discussion

Bench scale experiments and particle characterization

Irradiation of water-acetonitrile solutions of **3** and $HAuCl_4$ using UVA light led to a characteristic reddish colour of AuNP in less than one minute. For example, in a typical experiment a 2 mL sample of 1 mM $HAuCl_4$ in 1:1 water:acetonitrile containing 10 mM 3, was irradiated with a LED source centered at 368 nm giving an irradiance of 38,600 W m^2 (Fig. S2.4.1 †ESI). While other alcoholic or aqueous solvents also worked, 1:1 water-acetonitrile (v/v) proved convenient and met solubility requirements for the various experiments performed. Figure 2.2.1 shows the spectra obtained immediately after 30 s of UVA exposure and after some delay. Using this source of light, the onset of formation of nanoparticles was confirmed from the change in solution colour from light-yellow to purple as well as with the appearance of a plasmon band located at ~550 nm. Clearly, the plasmon peak extends to longer wavelengths, which is an indication of aggregation and polydispersity.[11,12] On the other hand, the intensity of the absorption peak increases in the following 10 minutes due to an increase in the population of plasmonic AuNP. We note that the monitor beam in the spectrometer (Cary 100) contributes to a post-irradiation growth process. The inset A of Figure 2.2.1 shows a representative TEM image where the nanoparticles obtained aggregate over 40 min having a nanoflower-like shape.[13,14] In fact, Au nanoflowers formation is related to the absence of particle stabilizing agents in the media.

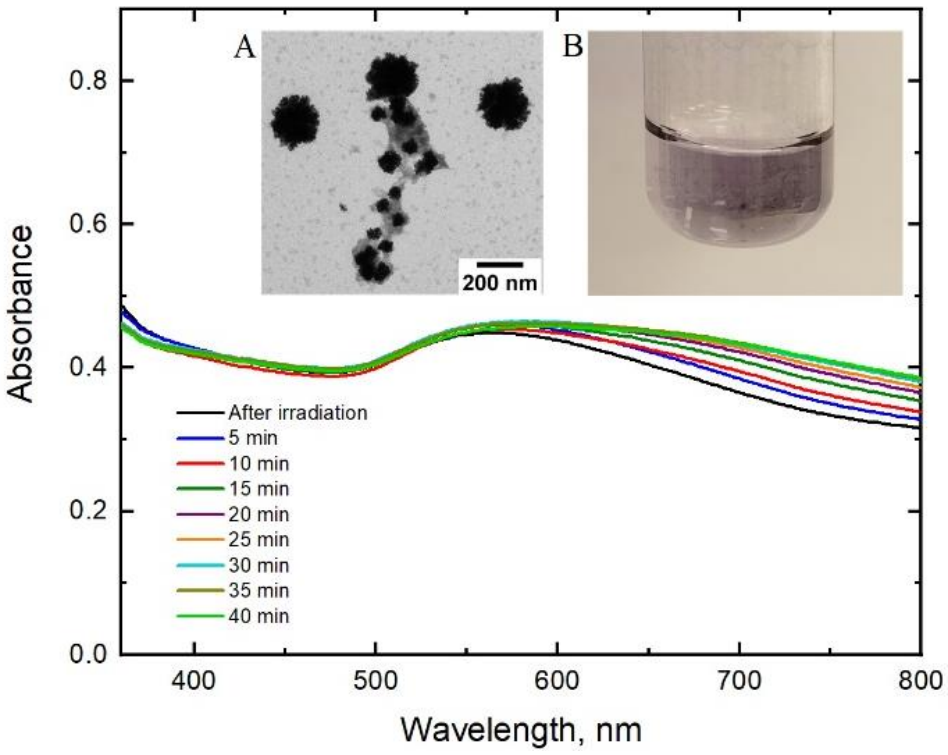

Figure 2.2.1. AuNP spectra obtained immediately after irradiation of 10 mM 3 and 1 mM $HAuCl_4$ in water-acetonitrile with UVA light for 30 s followed by post-irradiation growth at variable times, Inset: TEM image Au NPs **(A)**, colour of AuNPs immediately after irradiation **(B)**. Gold nanoflower structures form rapidly within just 30 s of irradiation, exhibiting a distribution of hotspots that are randomly located during the initial formation phase.

In an attempt to control particle growth and aggregation, the synthesis was repeated under various conditions, in particular using sodium citrate (NaCt)[13] as an in situ stabilizer. According to Dong et al.[13] the molar ratio (MR) of NaCt to $HAuCl_4$ is a primary factor that should be controlled to achieve a desired particle size. Specifically, to the system 10 mM **3** and 1 mM $HAuCl_4$ in 1:1 water:acetonitrile, 0.02mM, 0.05mM and 0.5mM of NaCt were added, keeping a molar ratio of NaCt to $HAuCl_4$ from 0.02 to 0.5. Figure 2.2.2 shows the spectra of the AuNPs when adding NaCt as a stabilizer.

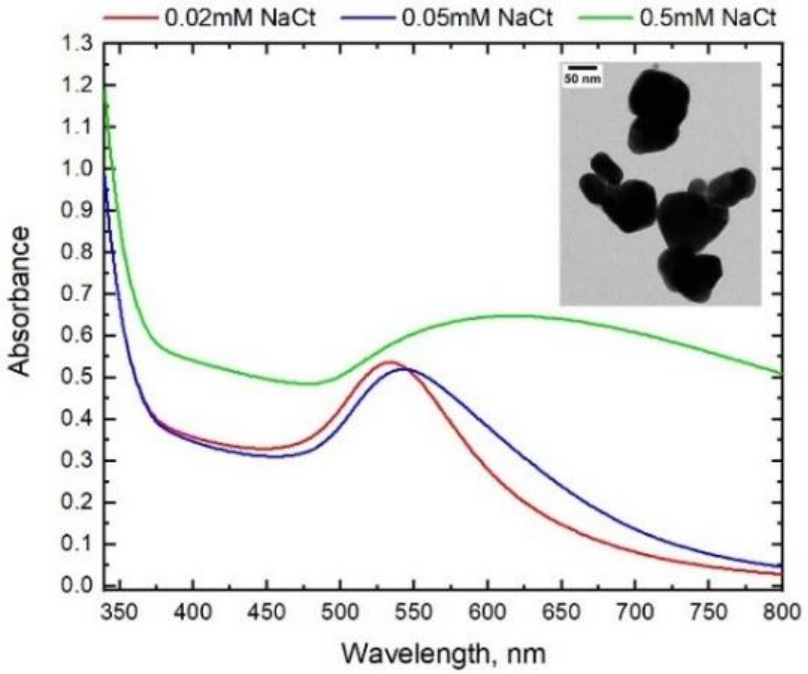

Figure 2.2.2. AuNP spectra obtained immediately after irradiation of sample containing 10 mM 3, 1 mM $HAuCl_4$, with 0.02 mM, 0.05 mM and 0.5 mM of NaCt with UVA light for 30 s. Inset: TEM image of Au NPs using 0.02 mM NaCt.

Concentration of 0.5 mM of NaCt provides a red shift of the plasmon band making it broader than expected, perhaps due to ionic strength effects,[14] while concentrations of 0.02 mM and 0.05 mM of NaCt provide a well-defined plasmon peak between 530-550 nm, with a more regular shape of the nanostructures as we can see in the inset of Figure 2.2.2. Nevertheless, while NaCt provides efficient stabilization and contributes to better control the shape of the AuNPs (Fig. S2.4.2 †ESI), its coverage relies on weak bonding and as a result it is easy to replace with other more permanent surface protectors if desirable.

Laser flash photolysis (LFP) of tetralone 3

The photolysis of **3** was examined in acetonitrile solution using 355 nm laser excitation. Initial samples were 20 mM with an absorbance of ~0.3 at the laser wavelength, see Figure S2.4.3 (†ESI) for the corresponding absorption spectrum. A signal,

characterized as the triplet state of the enol, was monitored at 390 nm and led to the transient spectra shown in Figure 2.2.3 with a lifetime of ~3.4 μs when the sample was deaerated with N_2 (left inset) and ~0.3 μs when under air.

The blue line signal observed on the left inset in Figure 2.2.3 is quenched by oxygen, as illustrated by the two decays shown. Diagnostic experiments (vide infra) and comparison with literature data[5] will show unequivocally that the species observed corresponds to the triplet state of the enol (**5(T$_1$*)**), which is a resonance structure of the biradical (**4BR**) resulting from intramolecular hydrogen transfer. Considering this, we tried to measure the lifetime of the ground state of the enol species (**5** in Scheme 2.2.4) and we found out that it is around ~170 μs with a signal much weaker and longer lived than **5(T$_1$*)**. Unfortunately, an accurate measurement was not possible. The proposed mechanism, including some of the reactions we illustrate below is given in Scheme 2.2.4.

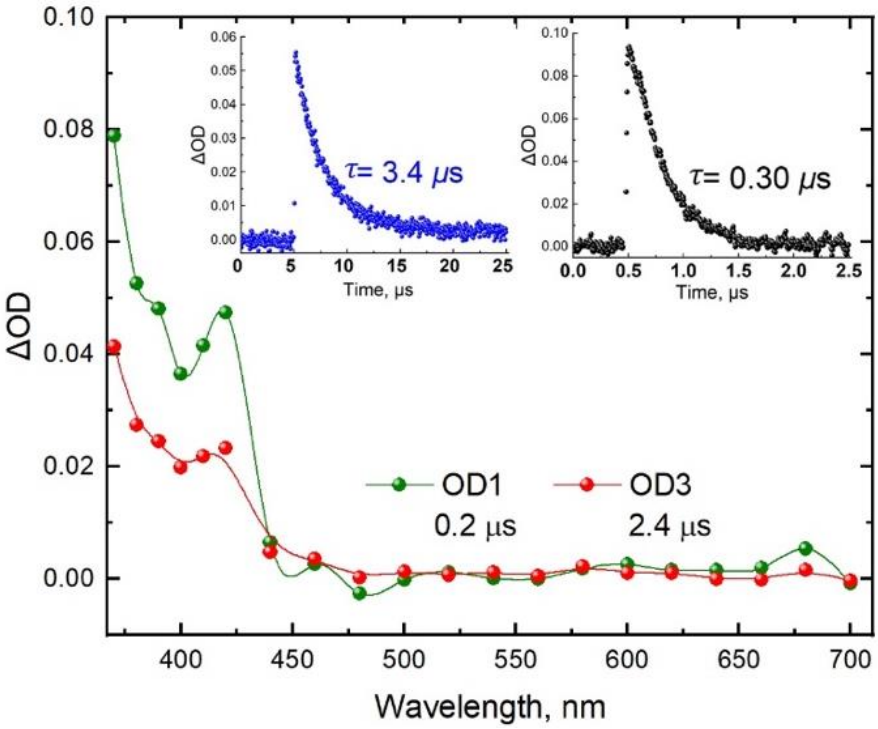

Figure 2.2.3. Transient spectra upon 355 nm laser excitation of **3** 20mM (MeCN) under N_2. Monitored at two different times following laser excitation. The two insets show the signal decay monitored at 390 nm under N_2 (left, τ = 3.4 μs) and under air (right, τ = 0.30 μs).

While excited triplet states are normally quenched by oxygen this is not a very good diagnostic tool, as many species can be quenched or scavenged by oxygen, including free radicals and carbenes.[15,16] However, when the quenching by oxygen is accompanied by the formation of singlet oxygen, then the test can be regarded as conclusive evidence for the excited triplet nature of the species being quenched.[17]

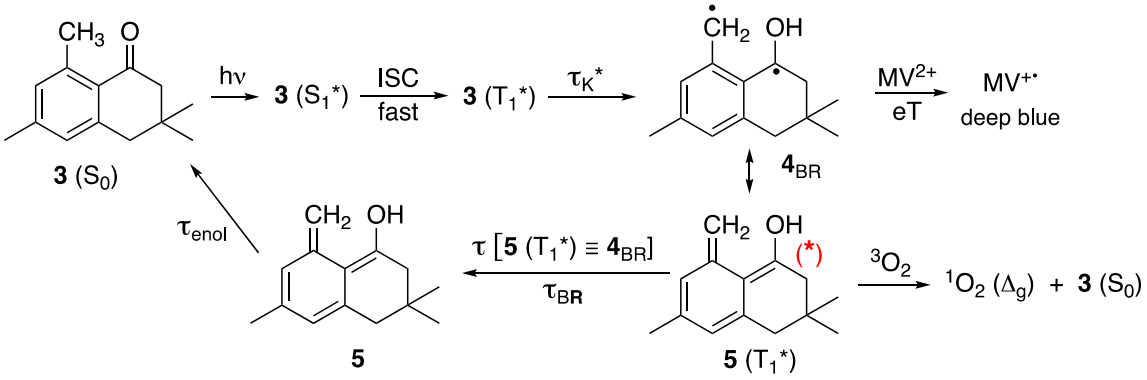

Scheme 2.2.4. General mechanism for the photochemistry of **3** in the presence of MV^{2+} or oxygen.

There are many strategies to monitor singlet oxygen, but the most direct and convenient is to monitor its luminescence at 1270 nm. Excitation at 355 nm of a 20 mM acetonitrile solution of **3** under air leads to the readily detectable NIR emission from singlet oxygen, Figure 2.2.4. When the laser is operated at full power (~22 mJ/pulse) the signal is strong and the lifetime 33 μs, which is significantly shorter than typical lifetimes reported for acetonitrile (typically 70-90 μs).[18] When the laser pulse is attenuated by a factor of 7, the signal decreases, and the lifetime is now 70 μs. This type of behaviour is well understood and corresponds to cases where the laser pulse, beyond forming singlet oxygen, generates long-lived transients or products that can scavenge singlet oxygen. In this case, the culprit is the enol **5**, as enols are known to scavenge singlet oxygen.[5]

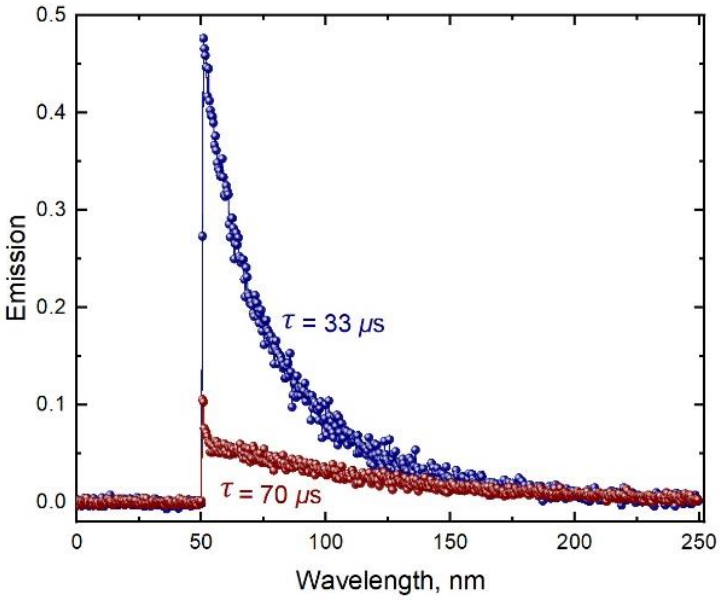

Figure 2.2.4. Singlet oxygen emission at 1270 nm of a 20 mM solution of **3**; Lifetime of singlet oxygen blue decay; red, decay when signal is attenuated.

Based on previous results, a question has raised as whether the triplet state of the ketone, **3(T_1*)**, could be species detected and be quenched by oxygen, with concurrent generation of singlet oxygen. With a triplet energy around 58 kcal/mol, conjugated dienes readily quench aromatic carbonyl triplets[19] (such as tetralones), but normally not low energy triplets such as enols. Thus, we monitored the long lived (~3.4 μs) transient signal at 390 nm for different concentrations of 1,3-pentadiene. The lifetime of the 390 nm signal was not affected, but its yield (top ΔOD before significant decay) was slightly reduced with each diene addition, as shown in the inset in Figure 2.2.5. This suggests that while the long lived transient (assigned to **5(T_1*)** = **4BR**) is not quenched, its precursor, the triplet ketone, 3(T_1*) is. From the variation of the optical densities (top ΔOD) when adding the quencher and equation (1) it is possible to construct a Stern-Volmer plot (Figure 2.2.5), from which $k_Q\tau_K$* can be obtained.

$$\Delta OD_{\infty}^{0} \Big/ \Delta OD_{\infty} = 1 + \ k_Q \tau_K (3)$$

The value of the slope is (12.5 ± 1.1) M^{-1}. By taking k_Q ~ 6.5 x 10^9 $M^{-1}s^{-1}$ for dienes, as measured for the molecule 5-methoxy-2-tetralone, which is a related tetralone triplet

with a longer-lived triplet (see ESI, Figure S2.4.4, signal decay in black (A)), we calculate τT ~ 1.9 ns. In other words, the precursor is the ketone triplet, but too short-lived for direct detection in our LFP system.

Naphthalenes are another type of triplet quencher with quenching efficiencies similar to dienes. Addition of up to 0.049 M 1-methylnaphthalene led to a modest signal of its triplet (~420 nm), see Figure S2.4.5 (†ESI). As expected the growth of the signal was too fast for our LFP system, in agreement with the 1.9 ns lifetime determined by diene quenching.

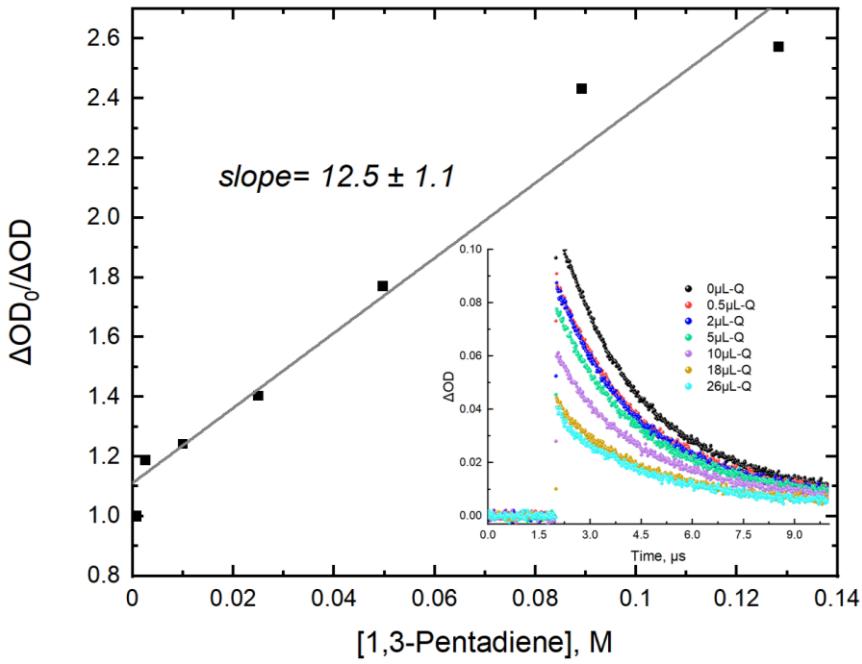

Figure 2.2.5. Stern Volmer plot for the quenching of **3**, by 1,3-pentadiene. The inset shows the decrease of the top ΔOD as more diene is added. Note that the actual lifetime (for the enol triplet) does not change, only its yield is affected.

Laser flash photolysis of tetralone 3 in the presence of Au(III)

Addition of $AuCl_4^-$ to a system containing tetralone causes the biradical $\mathbf{4_{BR}}$ (also triplet enol) to be scavenged accompanied by the formation of gold atoms, leading to nanoparticle formation, Scheme 2.2.5. These unprotected NPs are synthesized in seconds in 1:1 acetonitrile: water solution under N_2. AuNPs have previously been synthesized photochemically using ketyl radicals as reducing agents, derived from benzophenone[20] or benzoin,[21] that although they require different conditions, are mediated by triplet excited states with longer lifetimes.

Given the excellent signal to noise obtained in LFP experiments (see insets in Figure 2.2.3) it seemed natural to try to determine k_{eT} by simply quenching the biradical $\mathbf{4_{BR}}$ signal with gold ions. unfortunately, these experiments proved very difficult because the free radical **6** is very long lived and its spectrum overlaps extensively with 4_{BR}. Figure S2.4.6 †ESI shows the signal decays for the biradical 4_{BR} being quenched by 0.2 mM and 0.3 mM solutions of $HAuCl_4$ and the transient spectra of the samples in the presence and absence of gold. Effectively, quenching $\mathbf{4_{BR}}$ makes the chromophore longer lived; it was clear however that k_{eT} was very fast. Fortunately, the probe technique[22] using methyl viologen as a probe allowed to estimate this rate constant (*vide infra*).

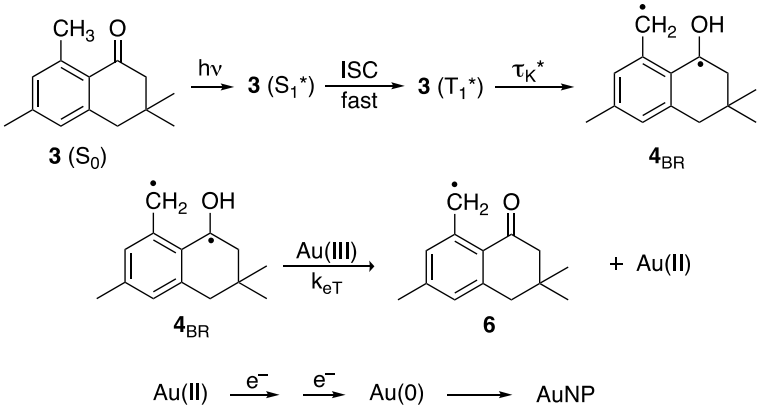

Scheme 2.2.5. Photolysis of **3** and formation of Au NPs.

Figure 2.2.6 shows the spectra obtained immediately after laser excitation (~100 shots) and after some delay. It should be noted that, the AuNP plasmon band, usually located at ~530 nm, is broader than usual and extends to longer wavelengths (see arrows

in Fig.2.2.6). This is an indication of polydispersity and aggregation,[10,11] something that is revealed also by the TEM images (see inset Fig. 2.2.6). These types of images are frequently described as gold nanoflowers,[23,24] and their formation is related to the absence of particle stabilizing agents. Thus, facilitating post-exposure growth and aggregation.

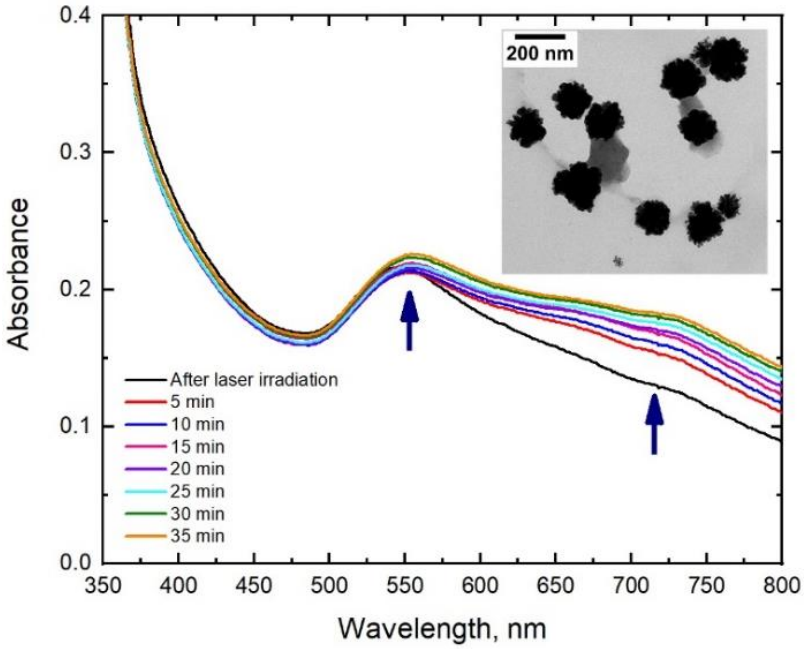

Figure 2.2.6. AuNP spectra obtained immediately after irradiation of sample containing 10 mM **3**, 1 mM $HAuCl_4$, with laser excitation, followed by post-irradiation growth at variable times, Inset: TEM image Au Nanoflowers.

Following several experiments, the synthesis of the nanostructures was repeated using NaCt as an additive. Specifically, to the system containing 10 mM **3** and 1 mM $HAuCl_4$ in 1:1 water:acetonitrile, 0.02 mM, 0.05 mM and 0.5 mM of NaCt were added (same NaCt concentrations from bench scale experiments). Figure 2.2.7 shows the spectra of the AuNPs when adding NaCt as a stabilizer. The inset of Figure 2.2.7 shows the ruby-red colour characteristic of AuNP with its SPR peak at 530 nm. The main change when using NaCt as part of the system, can be evidenced in the TEM images of Figure S2.4.7 (†ESI), where particularly when using 0.05 mM NaCt shows considerable polymorphism. A similar trend can be observed for the additional concentrations of NaCt that were tested, see Figure S2.4.7 (†ESI).

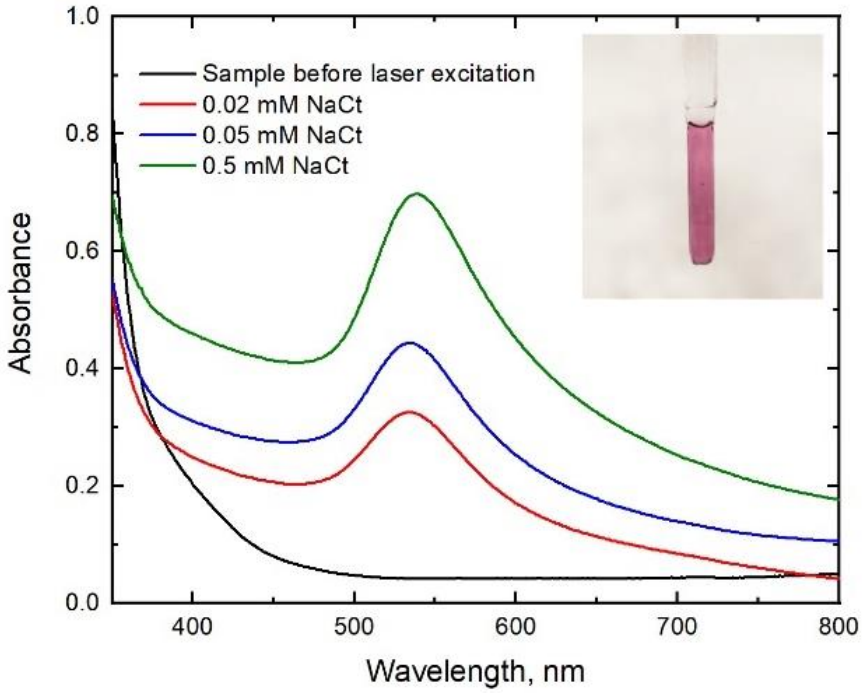

Figure 2.2.7. AuNP spectra obtained immediately after irradiation of sample containing 10 mM **3**, 1 mM $HAuCl_4$, 0.02 mM, 0.05 mM and 0.5 mM of NaCt with 150 ± 20 laser pulses, Inset: Image of the LFP cuvette containing Au NPs using 0.05 mM NaCt.

Additionally, the effect of the initial gold salt concentration in the formation of Au nanostructures was also investigated. In a system containing 10 mM tetralone **3**, we tried different $HAuCl_4$ concentrations such as 0.2 mM, 0.3 mM, 0.5 mM, 1 mM and 2 mM. Particularly, the system containing 10 mM **3** and 0.2 mM $HAuCl_4$ shows a transient absorption spectra of the plasmon nanostructures with a small peak around ~530 nm, along with some triplet excited state of the enol with a band at 390 nm as evidenced in Figure 2.2.8.

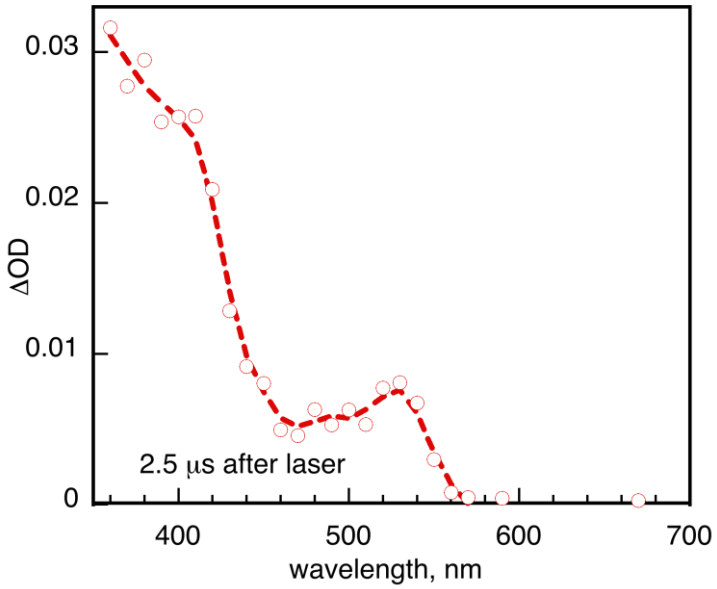

Figure 2.2.8. AuNP spectra obtained 2.5 μs after irradiation of sample containing 10 mM **3**, 0.2 mM $HAuCl_4$, with laser light. Note the SPR band at ~530 nm.

The observation of plasmonic absorbance generated within 2.5 μs of laser excitation is remarkable, as several hundred atoms are required for AuNP to show plasmonic absorbance, and it seems highly unlikely that the AuNP formation kinetics would allow such large aggregates to form in the microsecond time scale. However, we note that the vertical axis is an absorbance change, ΔOD and that this change is quite small (compare with Figures 2.2.6 and 2.2.7). We attribute this absorbance change to the growth of existing nanoparticles, rather than to the creation of new ones, schematically illustrated in equation 4 in Scheme 2.2.6.

$$Au_n + m\,Au^0 \longrightarrow Au_{n+m} \qquad (4)$$

AuNP — Bigger AuNP

with n >> m

Scheme 2.2.6. AuNP formation

Since the extinction coefficient of AuNP is proportional to the number of atoms making the nanoparticle, then a small ΔOD is consistent with a small addition (m) of atoms

to an existing AuNP. We note that the process of AuNP formation is so efficient with tetralone **3**, that we expect some particles to be formed by the LFP monitoring beam and by any earlier laser pulses.

Furthermore, it is worth noting that from these experiments a 'sweet-spot' concentration region was identified when using 0.5 mM or 1 mM concentrations of $HAuCl_4$. Specifically, after irradiating the samples with ~100 laser shots, the absorption profile of each one was measured, see Figure S2.4.9 (†ESI), and particularly, when the system contains minor $HAuCl_4$ concentrations, AuNPs can be slightly formed, as is evidenced in Figure S2.4.10 (†ESI), wherein a small plasmonic peak around ~530 nm can be observed, along with the triplet excited state of the enol with a band at 390 nm, but despite this, the Au concentration is not enough to form a substantial plasmon peak at 530 nm. In contrast, when increasing $HAuCl_4$ concentrations up to 2 mM, the excess of gold competes for light absorption. Radar chart plot of Figure 2.2.9 is useful to visualize rapidly the absorption of each sample containing different $HAuCl_4$ concentrations.

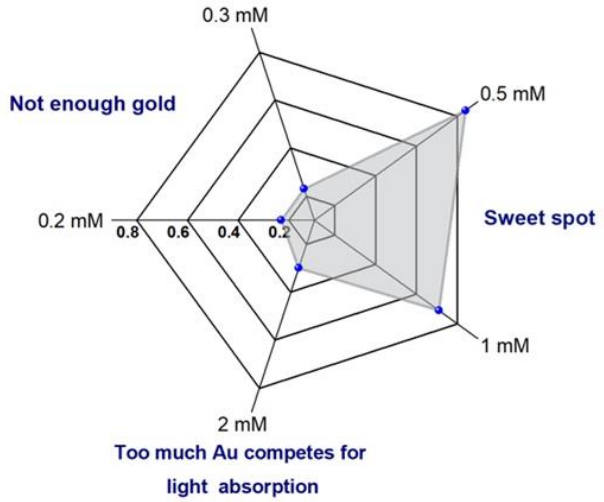

Figure 2.2.9. Radar chart plot for absorbance due to the the formation of AuNPs in samples containing 10 mM **3** and 0.2 mM, 0.3 mM, 0.5 mM, 1 mM, 2mM $HAuCl_4$, monitored at 530 nm after exposure to 100 355 nm laser pulses.

Competition of Au(III) with methyl viologen

When a solution of methyl viologen (MV^{2+}) is added to a system generating biradical **5*** or **4_{BR}**, electron transfer leads to the rapid formation of the corresponding radical cation, as shown in Scheme 2.2.7. $MV^{+\bullet}$ can be readily monitored at 600 nm, as illustrated in Figure 2.2.10.

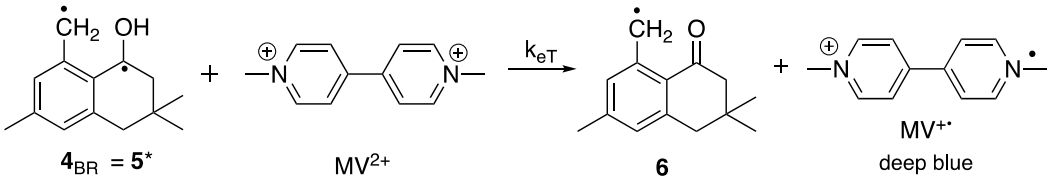

Scheme 2.2.7. Electron transfer from biradical **4_{BR}** to **MV^{2+}**. Note that while **5*** or **4_{BR}** are resonant forms of the same species, the biradical representation is preferred for electron transfer reactions, as it shows better the strongly reducing ketyl radical moiety.

The growth observed in Figure 2.2.10 (blue data) shows the formation of the strongly absorbing $MV^{+\bullet}$ radical cation. The growth can be fitted with first order kinetics and yields k_G^0 = 1.56 x 106 s^{-1}, where the superscript '0' indicates the absence of Au(III). Given the known lifetime of 4_{BR} in this solvent (2.7 μs), it is possible to determine k_{eT} (see equation 5). In this case we estimate is 2.5 x 109 $M^{-1}s^{-1}$, which compares well with rate constants determined for Norrish Type II biradicals.[9]

$$k_G = (\tau^0_{4_{BR}})^{-1} + k_{eT}[MV^{2+}] (5)$$

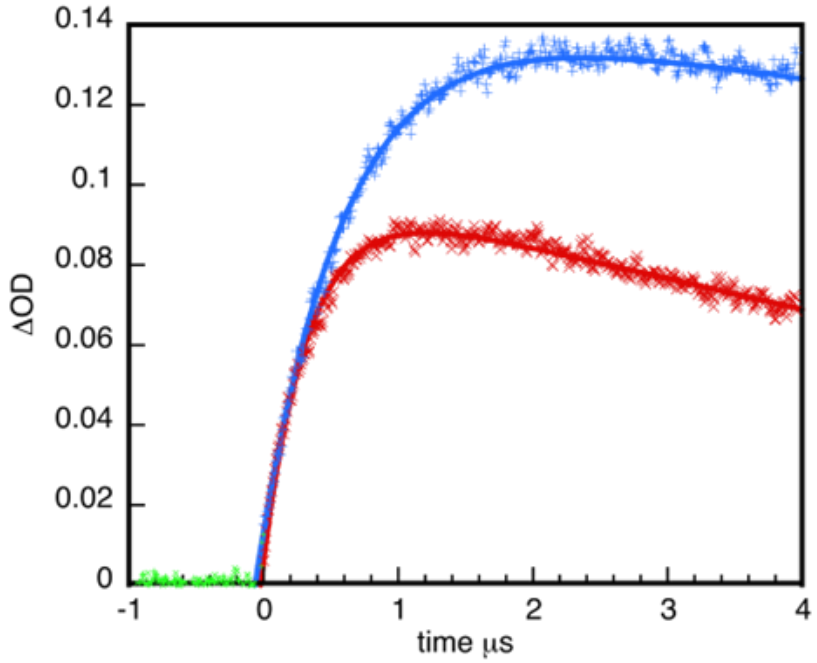

Figure 2.2.10. Kinetic growth of $MV^{+\bullet}$ monitored at 600 nm for a solution in 1:1 water:acetonitrile under nitrogen, containing 10 mM **3**, in the presence of 0.48 mM MV^{2+} (blue curve). The red curve was obtained after adding 0.23 mM $AuCl^{4-}$. The sample was irradiated with a 355 nm pulsed laser.

When 0.23 mM of $AuCl_4^-$ is added, following the MV^{2+} addition, three changes are observed (see Figure 2.2.10, data in red); first, the magnitude of the growth signal is reduced by about 30%, second, the growth kinetics is faster, specifically 2.95 x 106 s^{-1} compared with 1.56 x 106 s^{-1} in the absence of gold and finally the decay of the signal is significantly faster, suggesting Au(III) can accept an electron from $MV^{+\bullet}$. Equation 6 can be modified to incorporate the effect of Au(III) on the trapping of $\mathbf{4_{BR}}$ (k_{Au}).

$$k_G^{Au} = (\tau_{4_{BR}}^0)^{-1} + k_{eT}[MV^{2+}] + k_{Au}[Au(III)] \quad (6)$$

$$k_G^{Au} - k_G = k_{Au}[Au(III)] \quad (7)$$

which leads to kAu = 6.0 x 10^9 $M^{-1}s^{-1}$, in other words almost diffusion controlled. It should be noted that the reaction may be assisted by the fact that the donor ($MV^{+\bullet}$) is positively charged, while the acceptor, $AuCl_4^-$, is negative.

We note that the 30% reduction in $MV^{+\bullet}$ yield is consistent with the kinetic analysis above; however, we have refrained from doing a more quantitative analysis as $AuCl_4^-$ has some absorption at the laser wavelength (355 nm) and it would be rather speculative to try to refine this value.

Fitting of the decay component for $MV^{+\bullet}$ leads to 8.7 x 10^4 s^{-1} in the absence of gold and 4.7 x 10^5 s^{-1} in the presence of 0.23 mM of $AuCl_4^-$. The difference corresponds to a rate constant of ~1.7 x 10^9 $M^{-1}s^{-1}$ for the electron transfer of reaction 8 in Scheme 2.2.8.

$$MV^{+\bullet} + Au(III) \longrightarrow MV^{2+} + Au(II) \qquad (8)$$

Scheme 2.2.8. Electron transfer between $MV^{+\cdot}$ and Au (III).

Experimental

Materials and Methods

Materials. All chemicals (3,3,6,8-tetramethyl-1-tetralone, Gold(III) chloride trihydrate, 1,3-pentadiene, 1-methylnaphtalene, methyl viologen dichloride hydrate) were purchased from Sigma Aldrich and frequently dissoved in HPLC grade acetonitrile and Milli Q water as required.

Standard laboratory techniques. The photochemical generation of AuNP using 3,3,6,8-tetramethyl-1-tetralone was performed under UVA (368 nm) irradiation using a Luzchem LEDi at max power (~ 38600 W m^{-2}, see Figure S2.3.1 for the emission spectrum. UV-Vis spectra were obtained using an Agilent Cary 100 UV-Vis spectrometer.

Time-resolved laser methods. The triplet quenching experiments of 3,3,6,8-tetramethyl-1-tetralone and 5-methoxy-2-tetralone were performed using a Surelite Nd-YAG laser 355 nm (~10-20 mJ/pulse) in a LFP-111 laser-flash photolysis (LFP) system (Luzchem Inc., Ottawa, Canada) and 1×1 cm or 0,7 x 0.7 cm LFP cuvettes from-Luzchem. Samples of 3,3,6,8-tetramethyl-1-tetralone and 5-methoxy-2-tetralone were prepared in 1:1

acetonitrile and Milli Q water mixture with an absorbance of ~0.3 at the laser wavelength. The samples were deaerated with N_2 prior to use, unless otherwise indicated. For emission experiments at 1270 nm, the same LFP system was fitted with a Hamamatsu NIR photomultiplier system. All kinetic experiments were fitted using a user-defined fitting with Kaleidagraph or Origin software.

Conclusions

Tetralone 3 is a highly efficient precursor for the photogeneration of AuNP, with good yields in minutes under UVA irradiation. The reduction is mediated by the biradical involved in the photoenolization of **3**, where its ketyl moiety is a strong reductant. The spectral purity of the plasmon band can be controlled by addition of small concentrations of citrate and analysis of the plots shows that the optimum concentration of citrate is ~0.05 mM. The electron transfer efficiency is so high that considerable ripening (with SPR absorbance increase) occurs in long time scales (minutes to hours) following short UVA exposure. In contrast with other systems where if transient reductants, such as ketyl radicals, fail to reduce gold, they result in reaction byproducts, in the case of tetralone **3**, they simply return to the original tetralone as part of the ground state keto-enol equilibrium. Interestingly, our LFP experiments reveal the growth of SPR signals in the microsecond time scale, an effect that is attributed to the growth of existing nanoparticles, rather that to the formation of new ones.

Conflicts of interest

There are no conflicts to declare.

Acknowledgements

This work was supported by the Natural Sciences and Engineering Research Council of Canada, the Canada Foundation for Innovation, and the Canada Research Chairs Program. We thank Dr. Neeraj Joshi for his assistance with all laser flash photolysis experiments.

2.3. References

1. P. J. Wagner, *Accounts of Chemical Research*, 1971, **4**, 168–177.

2. J.P. Bays, M.V. Encinas and J.C.Scaiano, Macromolecules, 1979, **12**, 348–350.

3. P. J. Wagner, *Pure and Applied Chemistry*, 1977, **49**, 259–270.

4. P. K. Das, V. Encinas, R. D. Small and J. C. Scaiano, Journal of the American Chemical Society, 1979, **101**, 6965–6970.

5. R. W. Redmond and J.C. Scaiano, *Journal of Physical Chemistry*, 1989, **93**, 5347–5349.

6. K. L. McGilvray, M. R. Decan, D. Wang and J. C. Scaiano, *Journal of the American Chemical Society*, 2006, **128**, 15980–15981.

7. S. Jockusch, M. S. Landis, B. Freiermuth and N. J. Turro, *Macromolecules*, 2001, **34**, 1619–1626.

8. J. C. Scaiano, P. Billone, C. M. Gonzalez, L. Maretti, M. L. Marin, K. L. McGilvray and N. Yuan, *Pure and Applied Chemistry*, 2009, **81**, 635–647.

9. R. D. Small and J. C. Scaiano, *The Journal of Physical Chemistry*, 1977, **81**, 828–832.

10. P. Hyde and A. Ledwith, *Journal of the Chemical Society*, 1974, 2, 1768–1772.

11. P. K. Jain, K. S. Lee, I. H. El-Sayed and M. A. El-Sayed, *Journal of Physical Chemistry B*, 2006, **110**, 7238–7248.

12. Y. Yano, M. Nisougi, Y. Yano-Ozawa, T. Ohguni, A. Ogawa, M. Maeda, T. Asahi and T. Zako, *Analytical Sciences*, 2019, **35**, 685–690.

13. J. Dong, P. L. Carpinone, G. Pyrgiotakis, P. Demokritou and B. M. Moudgil, *Kona Powder and Particle Journal*, 2020, **37**, 224–232.

14. B. Nikoobakht, Z. L. Wang and M. A. El-Sayed, *Journal of Physical Chemistry B*, 2000, **104**, 8635–8640.

15. B. Maillard, K.U. Ingold and J.C. Scaiano, *Rate Constants for the Reactions of Free Radicals with Oxygen in Solution*, 1983, 105, 5095–5099.

16. N. H. Werstiuk, ~ H L Casal, J. C. Scaiano and H. L. Casal, *Canadian Journal of Chemistry*, 1984, **62**, 2391–2392.

17. C. Schweitzer and R. Schmidt, *Chemical Reviews*, 2003, **103**, 1685–1757.

18. F. Wilkinson, W. P. Helman and A. B. Ross, *Journal of Physical and Chemical Reference Data*, 1993, **22**, 113–262.

19. P. J. Wagner and I. Kochevar, *Journal of the American Chemical Society*, 1968, **90**, 2232–2238.

20. S. Kapoor and T. Mukherjee, *Chemical Physics Letters*, 2003, **370**, 83–87.

21. P. T. Itakura, K. Torigoe and K. Esumi, *Preparation and Characterization of Ultrafine Metal Particles in Ethanol by UV Irradiation Using a*, 1995, 11, 4129–4134.

22. J. C. Scaiano, R.A. Moss, M.S. Platz, M.J. Jones Jr, *Hoboken: Wiley*, 2004, 847–872.

23. Y. W. Lee, N. H. Kim, K. Y. Lee, K. Kwon, M. Kim and S. W. Han, *Journal of Physical Chemistry C*, 2008, **112**, 6717–6722.

24. D. P. Yang, X. Liu, C. P. Teng, C. Owh, K. Y. Win, M. Lin, X. J. Loh, Y. L. Wu, Z. Li and E. Ye, *Nanoscale*, 2017, **9**, 15753–15759.

2.4. Post-print Version of Supporting Information

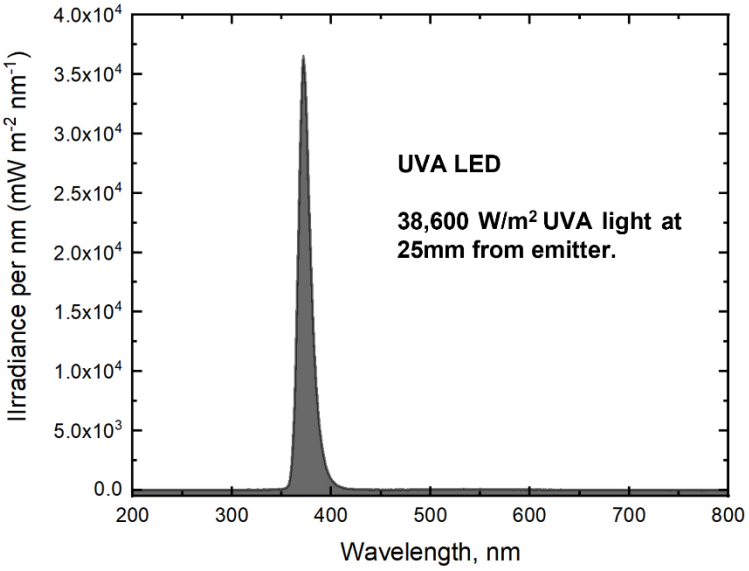

Figure S2.4.1. Spectral Irradiance of 368 nm Luzchem LED.

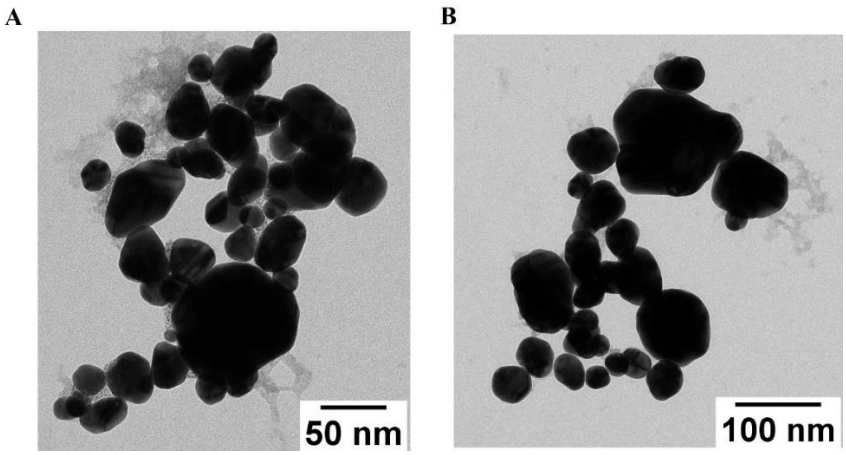

Figure S2.4.2. TEM images of Au NPs using 10 mM **3**, 1 mM $HAuCl_4$, 0.05 mM **(A)** and 0.5 mM **(B)** of NaCt with UVA light (368 nm) for 30 s.

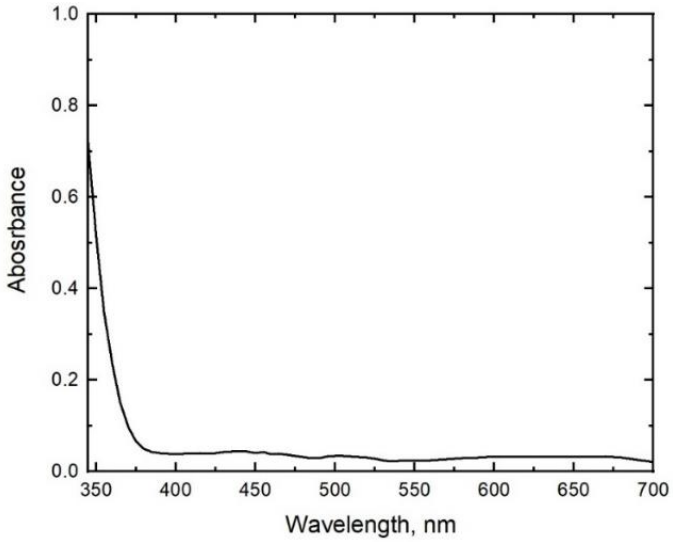

Figure S2.4. 3. UV-Vis absorption spectrum of 20 mM **3** in acetonitrile under N_2.

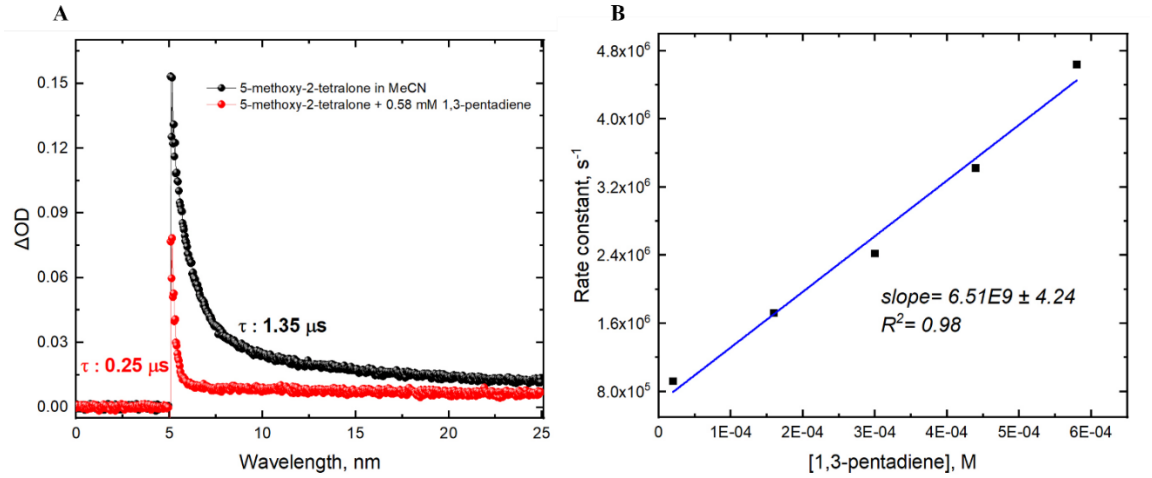

Figure S2.4.4. Signal decay monitored at 400 nm under N_2 of 5-methoxy-2-tetralone in MeCN (black curve, τ = 1.35 μs) and after adding 0.58 mM 1,3-pentadiene (red curve, τ = 0.25 μs) **(A)**. Samples irradiated with a 355 nm laser pulse. Note that the actual lifetime and the yield are affected since the triplet excited state of the tetralone is being quenched by 1,3-pentadiene. Kinetic plot for the quenching of triplet excited state of 5-methoxy-2-tetralone by 1,3-pentadiene **(B)**.

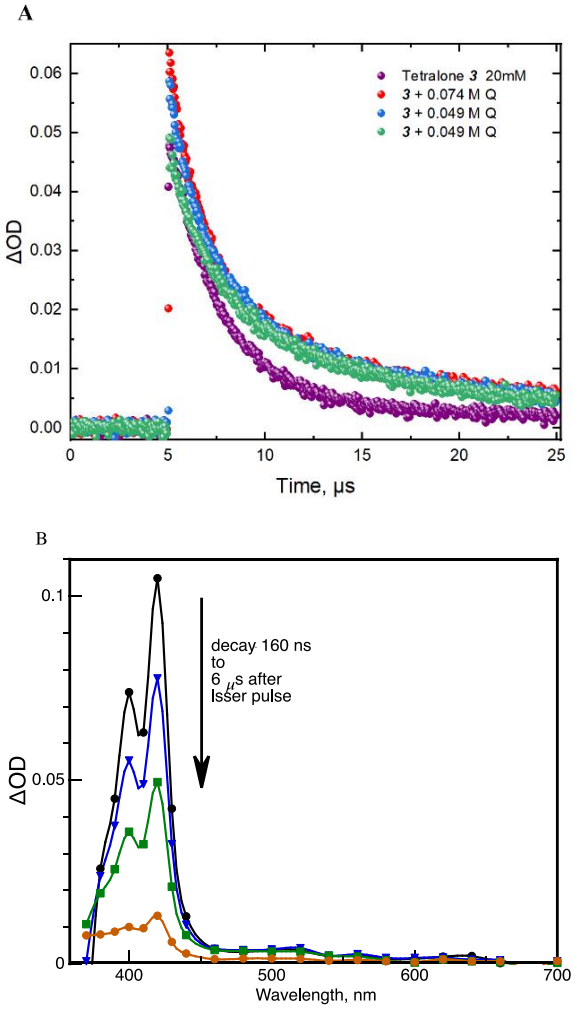

Figure S2.4.5. Transient spectra upon 355 laser excitation of **3** 20 mM (in MeCN) under N_2 (purple decay) and after addition of different concentrations of 1-methylnaphtalene (Q, quencher) **(A)** and transient spectra of sample containing **3** 20 mM and 0.049 M of 1-methylnapthalene showing the 1-Methylaphthalene triplet spectrum (~420 nm) decaying in the microsecond time scale **(B)**.

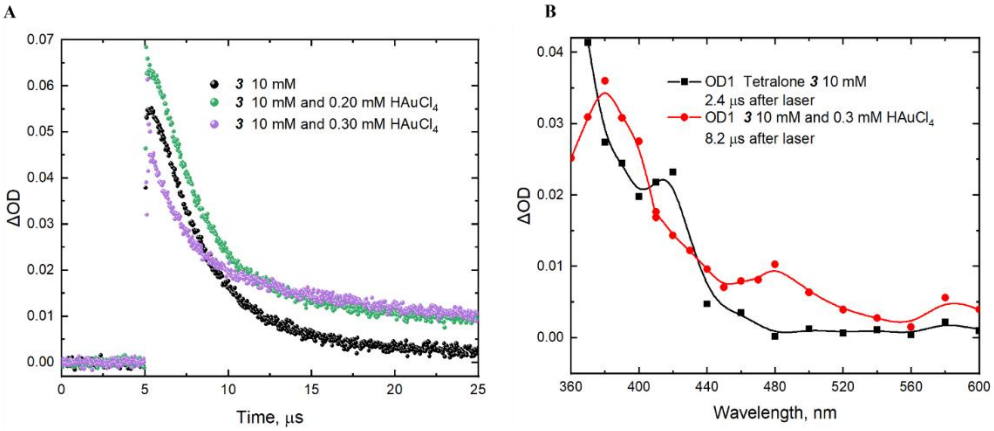

Figure S2.4.6. Biradical 4BR being quenched by $HAuCl_4$. Concentrations of 0.2 mM and 0.3 mM of $HAuCl_4$ were added to a 10mM solution of tetralone **3**. Black decay with a lifetime of 3.4 μs, green and purple decays with lifetimes of 2.9 μs **(A)**. Note that the lifetime is being reduced when adding $HAuCl_4$ solution since gold plays a quencher role of the biradical 4BR). Spectra of samples containing tetralone 3 10 mM (black) and **3** 10 mM and 0.30 mM of $HAuCl_4$ (red) **(B)**.

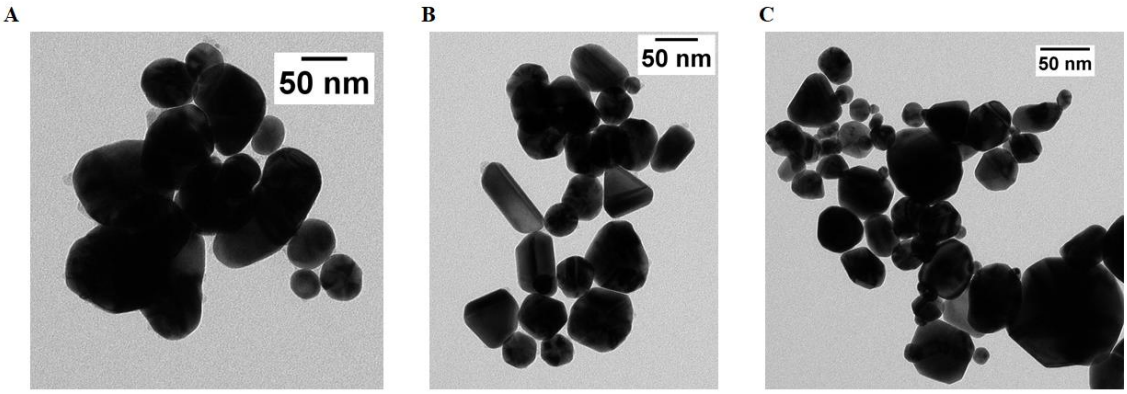

Figure S2.4.7. TEM images of 10 mM **3**, 1 mM $HAuCl_4$, 0.02 mM **(A)**, 0.05 mM **(B)** and 0.5 mM **(C)** of NaCt with laser light.

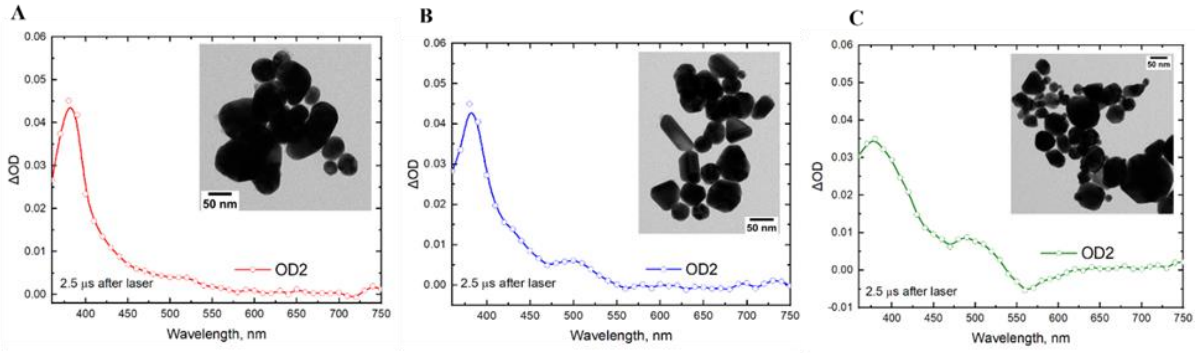

Figure S2.4.8. AuNP spectra obtained 2.5 μs after irradiation of sample containing 10 mM **3**, 1 mM $HAuCl_4$, 0.02 mM **(A)**, 0.05 mM **(B)** and 0.5 mM **(C)** of NaCt with laser light.

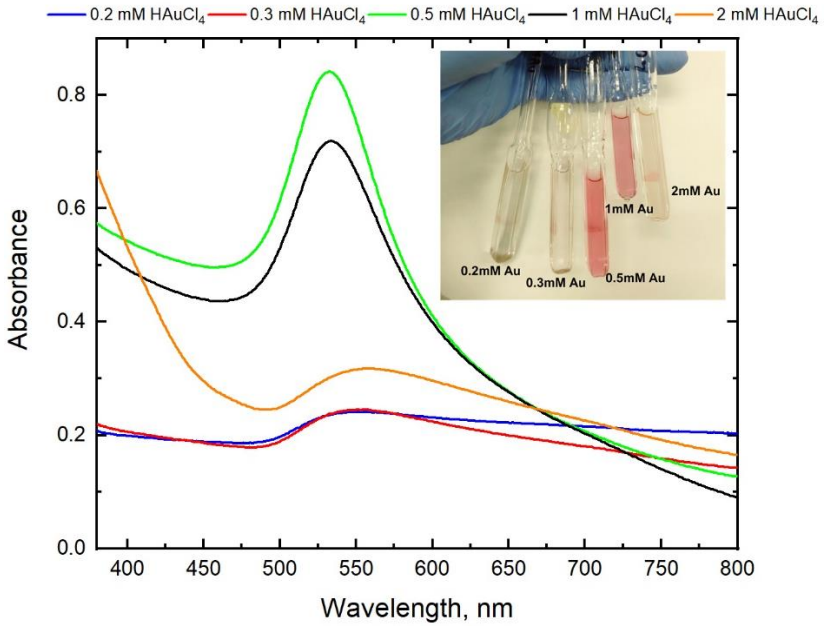

Figure S2.4.9. UV-Vis absorption spectrum of Au NPs using 10 mM **3**, 0.2 mM, 0.3 mM, 0.5 mM, 1 mM, 2mM $HAuCl_4$ after ~100 laser shots.

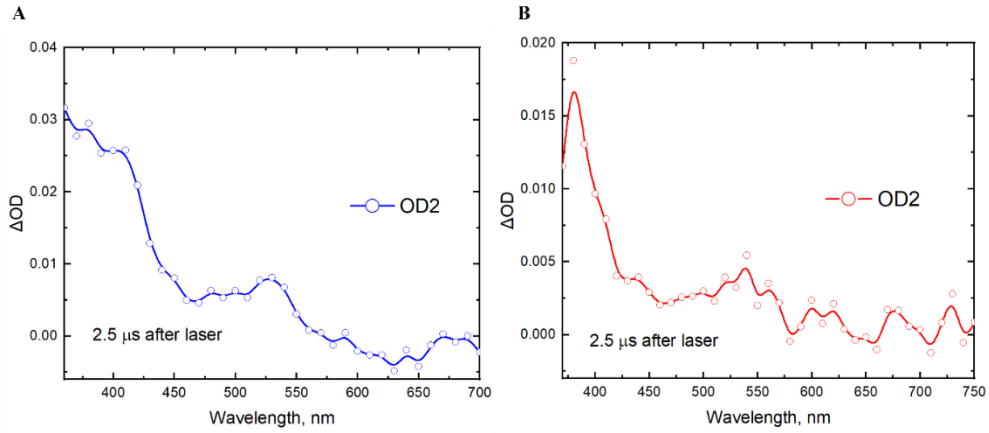

Figure S2.4.10. Transient spectra of Au NPs using 10 mM **3**, 0.3 mM **(A)** and 2 mM $HAuCl_4$ **(B)** after ~100 laser shots.

3. Understanding α-lipoic acid photochemistry helps to control the synthesis of plasmonic gold nanostructures

3.1. Preamble to chapter 3

This chapter explores an approach to polymer science through the photopolymerization of lipoic acid (LA), introducing a novel method to synthesize a cross-linked polymeric matrix of lipoic acid monomers (PALA), which acts as an in-situ stabilizer for the synthesis of gold nanoparticles (AuNPs). In this study we used the substituted tetralone from Chapter 2: 3,3,6,8-tetramethyl-1-tetralone as a photo-initiator, facilitating the reduction of Au (III) to Au(0), along with different concentrations of LA that helped to control the formation of plasmonic gold nanostructures. However, when using light (λ= 368 nm) as part of the polymerization process of LA, 40 min of irradiation for a concentration of 5.6 mM in 1:1 water: acetonitrile, as the suitable media, was enough to at least produce PALA of 5–6 units of monomer. The comprehensive characterization of PALA reveals its dual role as both an in-situ stabilizer and a reducing agent, for the synthesis of AuNPs. PALA demonstrates distinctive solvent swelling behaviour, particularly in non-polar solvents, and undergoes ring-opening crosslinking under UVA irradiation, as evidenced by ^{1}H-NMR spectroscopy. Notably, PALA's structure exhibits characteristics useful to achieving low polydispersity and narrow size distribution for the NPs, highlighting its potential in nanotechnology applications. Through detailed UV-Vis, NMR, HPLC-ESI-MS, and GPC analyses, this chapter explores into the PALA's interaction with AuNPs and its role in modulating their surface properties.

This study represents a significant advancement in understanding the photochemical transformations of LA and highlights the growing importance of PALA in the synthesis of AuNPs. LA was selected as an *in situ* stabilizer for AuNPs due to its carboxylic acid functional group, which makes it compatible with aqueous solutions. Its flexibility, due to being water soluble, makes it easy to incorporate into the proposed synthesis process. By exploring its applications and structural dynamics, this chapter contributes valuable insights into the future development of functional materials and perhaps biomedical

applications utilizing PALA-based nanocomposites, given its precursor properties in the field of medicine and nutrition.

3.2. Postprint Version of Manuscript

First published in: Photochemical and Photobiological Sciences, **2023**, 22, 1299–1307

Abstract

We propose the photopolymerization of Lipoic Acid (LA) as an novel approach to produce a cross-linked polymeric matrix of lipoic acid monomers (PALA) which helps to control the size of plasmonic gold nanostructures when using 3,3,6,8-tetramethyl-1-tetralone as the photo-initiator for the reduction of Au(III) to Au^0. A complete characterization of the polymer is included, and the dual behaviour of LA as an *in-situ* stabilizer and reducing agent is investigated. These findings are relevant to the understanding of the photochemical transformation of this biologically relevant compound and would benefit the increasing use of LA and PALA for the synthesis of various nanomaterials.

Introduction

α-Lipoic acid (LA) is a co-factor of the mitochondrial multi-enzyme complex in human bodies and plays a main role in energy metabolism. LA has attracted attention as a medicine and nutritional supplement including its distinctive antioxidant properties.[1,2,3,4] LA is also used in the cosmetic field[5] since it can be decomposed to afford many products like its reduced form, di-hydrolipoic acid (DHLA) which is capable to reduce cystine to cysteine wherein the latter acts as a precursor of glutathione, an important cellular redox regulation agent.[6] Likewise, the combination of LA and DHLA can be easily absorbed through the cell membrane playing an important role in the inhibition of reactive oxygen species (ROS) at the membrane level and even inside the cell, such as for example, singlet oxygen,[7] superoxide,[8] hydroxyl radicals,[8] among others.

In the nanotechnology field, LA is used as a capping ligand for inorganic nanostructures made of Au, in which the most common ones involve the formation of two

thiolate S-Au bonds (~130 kJ mol^{-1}), frequently by reaction of thiols with the gold surface.[9,10] The case of LA is particularly interesting, as due to its cyclic structure, in which once LA binds to the gold surface produces more stable molecular arrangements because of the formation of two S-Au bonds.[10,11] Despite all the applications in which lipoic acid is being used, it is worth noting that this cyclic disulfide molecule can be easily decomposed with light,[12] and has low thermal stability.[13] LA absorbs in the UVA region and the photodegradation and the products obtained after exposing LA under UV light depend on the irradiation conditions and on the light source. As for thermal degradation of LA, according to literature, the process of heating above the LA's melting point (60.5°C), leads to formation of polymer products. Specifically, to form LA's polymer (PALA), it is highly possible that the cyclic disulfide bond of LA molecules is broken, leading to a linear disulfide structure. In fact, LA has a moderately strained five-membered ring with an absorption band around 330 nm and the formation of PALA results in the reduction of the absorbance of this absorption band.

Many approaches have been reported to prepare polymers containing disulfide linkages in the main chain. Affleck and Dougherty[14] succeeded in the synthesis of a series of cyclic disulfides of many ring members. Polymer-like compounds were obtained mostly when heating at temperatures greater than the boiling point, but the details of the structure were not reported. LA-polymer based products were also reported after studying the photochemical reaction of LA using different solvents.[15,16] Additionally, there are studies that explore the photochemistry of LA,[17,18,19] which conclude that the disulfide bond can be fragmented into diradicals by long-wavelength UV light, triggering the radical-initiated polymerization of LA.

In this contribution we draw our research on interest to examine the photochemical properties of LA since this compound has found widespread use in the synthesis of metal nanostructures given its dual anchoring groups,[20] which strengthen its interaction with metal surfaces such as Au but unfortunately its chemistry is not well understood. We also explore the synthesis of PALA which does not require any light absorbers other than LA and the use of the polymer as an *in situ* stabilizing agent to control the size of plasmonic gold nanostructures when using 3,3,6,8-tetramethyl-1-tetralone as the photo-initiator.[21] In

fact, it is well-known the use of polymers as capping and stabilizing agents helping to avoid the particle agglomeration by providing stabilization effects for the dispersion of nanoparticles (NP).[22,23,24] For example, Gao *et al*[25] studied the effect of polyvinylpyrrolidone (PVP) on the morphology of silver NP and found that with specific amounts of this unbranched polymer, shape variation from Ag triangle NP to Ag sphere NP could be achieved. Several other studies also examine the effect of polymers on nanoparticles.[26,27] However, despite numerous investigations regarding the use of stabilizing agents on metal NP, particularly polymers, the role of PALA in synthesizing AuNP has not been explored in a way that can enhance the understanding of LA chemistry in these processes. Therefore, a combination of bench scale synthesis of PALA, its characterization, and its function as a stabilizing agent when making AuNP, delivers an intimate understanding of LA chemistry which helps to overcome drawbacks associated with conventional methods of nanoparticles preparation which use LA.

Results and discussion

Synthesis of poly(lipoic acid) [PALA]

Irradiation of chloroform solutions of LA using a Luzchem photoreactor equipped with UVA lamps led to a cloudy solution after 40 min of irradiation. For example, in a typical experiment, 4 mL samples of 1 mM and 5.6 mM LA both in chloroform, were irradiated in the photoreactor which was operated with 12 lamps, corresponding to an irradiance of ~25 W/m^2 (Fig. S3.4.1 †ESI). While other solvents like acetonitrile, water-acetonitrile (1:1) and methanol also worked, chloroform proved to be convenient for the polymer synthesis since it leads to a cross-linked polymer, and most of this type of polymers are insoluble in different solvents given their linked chain structure which inhibits solubilization.[28, 29] Figure 3.2.1 shows the spectra obtained after different times of UVA exposure.

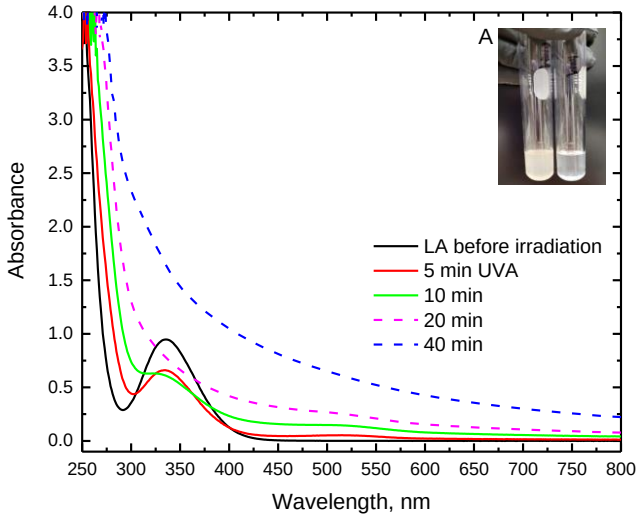

Figure 3.2.1. LA spectra obtained at different irradiation times of 5.6 mM LA solution in chloroform with UVA light. Inset **(A)** shows solutions of LA 5.6 mM (left) and 1 mM (right) after 40 min UVA exposure, both solutions in chloroform.

Using this UVA light source and conditions, led to the rapid bleaching of the band at 330 nm upon 20 min irradiation, with simultaneous increased absorption and light scattering (dashed lines in Figure 3.2.1) indicating the formation of polymers or oligomers, consistent with the turbidity of the samples (Inset, Figure 3.2.1). Based on Figure 3.2.1, after 10 min of UVA irradiation, there is around 30% of yield consumption of LA monomer. Visible light of ~400 (Fig. S3.4.2 †ESI) nm was also tested, and we found that prolonged irradiation affects the structure of LA, by breaking the S-S bond of the ring to produce a mixture of DHLA and PALA.

Characterization of PALA

To establish the properties of the crosslinked polymer, the swelling behaviour was investigated. Dynamic Light Scattering (DLS) was used to relate the hydrodynamic diameter of the particles in solution to the polymer dimensions. Table 3.2.1 shows that PALA exhibited a typical swelling ability in nonpolar solvents (CH_2Cl_2, $CHCl_3$, tetrahydrofuran, etc.) (Fig. S3.4.3 †ESI) and a low swelling ratio (shrink) in polar solvents like water.

Table 3.2. 1. Z-average diameter, DLS measurement of 1 mM and 5.6 mM LA samples in H_2O and $CHCl_3$ before and after specific UVA irradiation times in a Luzchem Photoreactor.

Solvent	**Sample Name**	**Z-avg. Diameter nm**
water	LA_1 mM_H_2O	73.5
water	LA_1 mM_5min UVA	79.7
water	LA_1 mM_10min	80.9
water	LA_1 mM_20min	114.1
water	LA_1 mM_40min	125.1
$CHCl_3$	LA_5.6 mM_$CHCl_3$	370.1
$CHCl_3$	LA_5.6 mM_5min UVA	439.1
$CHCl_3$	LA_5.6 mM_10min UVA	609.1
$CHCl_3$	LA_5.6 mM_20min UVA	2692
$CHCl_3$	LA_5.6 mM_40min UVA	3506

DLS data are gathered in Figure 3.2.2 and obtained by first measuring a sample of 1 mM LA in H_2O (dashed black line), then after UVA irradiation of the sample for 40 min and upon the addition of DMSO to the aqueous system. The exponential curves in Figure 3.2.2A show that the size in the LA solution increases after irradiation with UVA, given that the decay shifts to longer times, which reflects the cleavage of the S-S bond, and thus the initiation of polymerization. Further, in aqueous solution the swelling ability was confirmed because when adding DMSO, the curve shifts even more to the right, which is an indication that the mean size of the particles has increased.

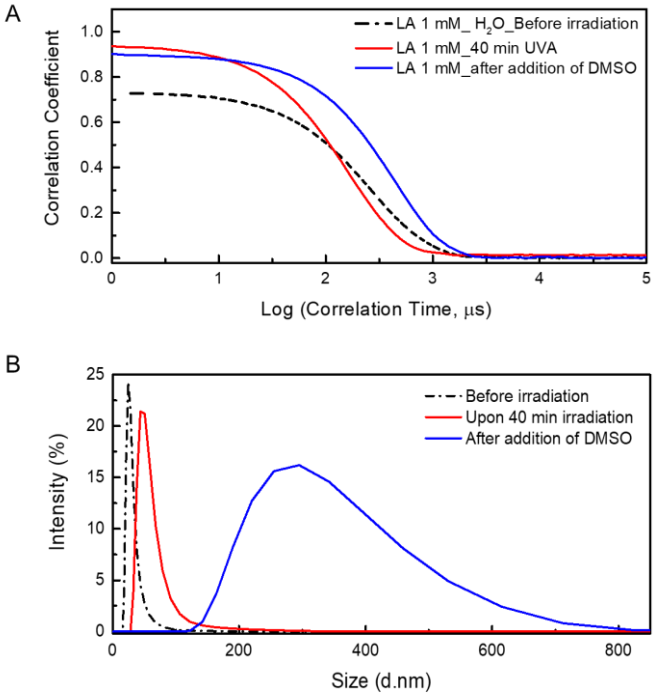

Figure 3.2.2. DLS correlation function measured at 25°C as a function of correlation time: 1 mM LA in aqueous solution, upon UVA exposure (Photoreactor) and after addition of DMSO **(A)**; Number-weighted diameters of same samples **(B)**.

Figure 3.2.2B also shows the particle size distribution which can be compared with the results of Table S3.4.1 (†ESI), wherein i) the Z-average values show that longer irradiation times led to an increase in size, and ii) that the identified particle population, which shows a peak around ~90 nm upon UVA irradiation, has a different peak after the addition in an organic solvent like DMSO (maximum around ~300 nm). This suggests that the penetration of an organic solvent into the polymer network can cause extensive swelling.

In addition, ^{1}H-NMR offered evidence of the ring opening crosslinking driven by UVA irradiation. Figure 3.2.3 shows the ^{1}H-NMR spectra of LA monomer and the polymer after 40 min of irradiation. For LA, (a1, a2) protons display resonances at δ 3.03-3.25 ppm, (b) protons show two peaks at δ 2.47 and 1.92 ppm, indicating the presence of the dithiolane ring. Additionally, the five-carbon straight-chain of LA shows peaks at different resonances for the protons between δ 2.38 and 1.50 ppm. However, after UVA irradiation,

the signals due to the hydrogens of LA decrease as the reaction progresses. Figure 3.2.3B displays that part of the signals, originally contributing to the region of protons (a) and (b), were converted to new signals at δ 3.11 ppm (a) and 2.01 ppm (b) respectively. This suggests that the ring of LA opened, and PALA had been obtained.[30] Further, the location of signals for protons (d), (e), (f), (g) remain unchanged, but were broadened, which we attribute to reduced molecular mobility, compared with LA signals.

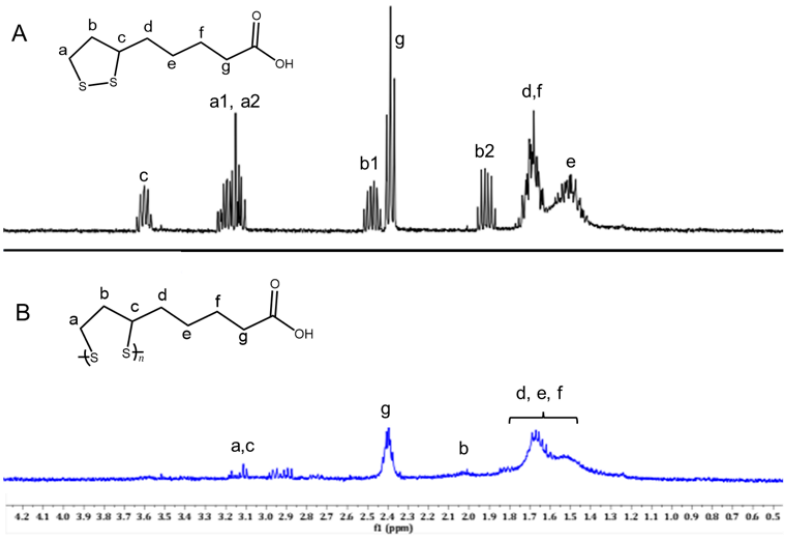

Figure 3.2.3. ^{1}H NMR spectra of LA 5mM in $CDCl_3$ **(A)**, and PALA upon 40 min UVA irradiation **(B).**

Kisanuki *et al.*[31] provided NMR evidence for the polymer obtained by a thermal method, wherein even though the signals are more intense due to the high concentrations used, they showed results of the thermal polymerization of LA in the presence of DHLA, in which the polymer yield was suppressed significantly in the presence of a small amount of the thiol compound, indicating that the thiol acts as an effective chain transfer agent in the polymerization of LA. In this case, when UVA light is involved in the polymerization process, it is highly possible that DHLA is being formed after the initial rupture of the disulfide bond. DHLA proton signals can be identified when performing ^{1}H-NMR of LA at higher concentrations than 5 mM following irradiation times of 40 min or longer. In fact, in Figure 3.2.3, low resonances at δ 2.9-3.0 ppm, δ 1.8 ppm and δ 1.30 ppm show evidence of protons (a), (b), (c) and those from the -S-H- bonds of DHLA respectively.[32] This

suggests the presence of DHLA obtained after irradiating LA can contribute to the polymerization of LA.

Different investigations about the structure of PALA have been recently reported, wherein a polycatenane structure is proposed, [33] and it could be achieved by shorter polymerization times, which leads to low polydispersity as well as narrow size distribution. Based on the UV-Vis and NMR results, we assume that PALA might have a crosslinked structure, consistent with the swelling observed upon DMSO addition.

To elucidate further the structure of the reaction product after UVA light exposure, HPLC-ESI-MS and GPC measurements were performed. Figure S3.4.4 (†ESI) shows the mass spectrum of LA which revealed that the protonated molecular ion (*m/z* 205) was partially fragmented to *m/z* 171 $[M\text{-}H_2S\text{-}H]^-$. However, after using UVA light for 40 min a 5.6 mM sample of LA (Figure 3.2.4A) shows charged species with *m/z* 410.6, 616.8 and 1033.8 detected in the negative ionization mode, due to the presence of the dimer, trimer and tetramer of LA; higher oligomers would not be detectable in our instrument since the masses exceed the detection limit. We speculate that 40 min of UVA light, under the conditions described above, might be enough to produce a polymer with at least 5 or 6 units of LA. Regarding the structure of the polymer, a polycatenane structure can be suggested; the structure is not always recognizable due to the complexity of polymer network[34] and analytical technique limitations.

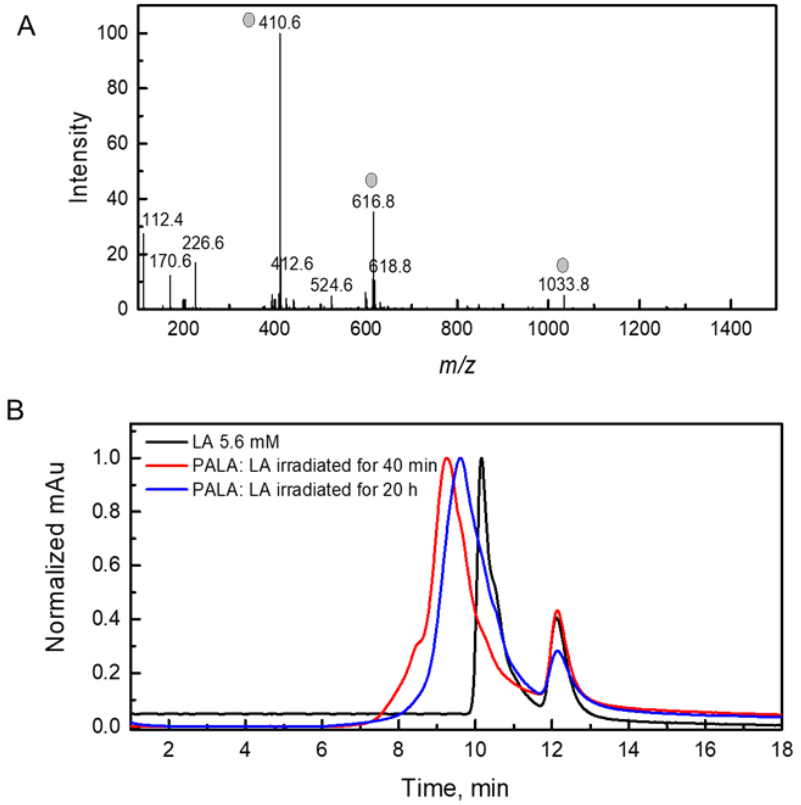

Figure 3.2.4. ESI- MS spectrum of PALA in acetonitrile after 40 min UVA irradiation of a 5.6 mM LA solution **(A)**, GPC traces for LA, 40 min and 20 h UVA irradiation **(B)** in tetrahydrofuran (THF) HPLC grade as solvent.

Gel Permeation Chromatography (GPC) was also used to measure the molecular weight of PALA. Figure 3.2.4B compares three GPC curves of PALA produced after UVA irradiation of LA 5.6 mM for 40 min, about 20 h and LA before irradiation. Clearly, even after 20 h, some LA or low oligomers are still part of the solution, since the peak for the irradiated samples extends up to ~11.5 min, where the band due to LA is ending before any exposure. This, is a confirmation that LA can undergo structural changes under UVA irradiation for at least 40 min. In fact, evidence that LA is being polymerized upon exposure of UVA light can be confirmed from Figure S3.4.5, which shows the UV-Vis profile of the peak at 9.5 min for the LA sample that was irradiated for 40 min, and the peak around 10.5 min for the 5.6 mM LA sample of the GPC curves described in Figure 3.2.4B. The typical

band of LA around ~330 nm, due to its ring, is present before irradiation (Figure S3.4.4.B) and upon 40 min of UVA exposure, such band has disappeared (Figure S3.4.4. A).

The peak shape for both samples in the GPC curves (Figure 3.2.4B) is narrow suggesting a low polydispersity. By using the calibration curve with standard polystyrenes (Figure S3.4.6, †ESI), molecular weight of PALA samples was determined to be ~1316 g mol^{-1} for the sample irradiated for 40 min and ~582 g mol^{-1} for the sample after 20 h of UVA exposure. It is worth noting that this does not lead to an absolute value, but to an estimated molecular weight that was validated with the *m/z* values obtained from HPLC-ESI-MS (Figure3.2.4A). For the small peak around ~12 min of Figure 3.2.4B, it corresponds to an impurity and therefore it should be disregarded.

Interestingly, when using light as part of the polymerization process of LA, 40 min of irradiation for a concentration of 5.6 mM might seem enough to at least produce PALA of 5-6 units of monomer. However, increasing the irradiation time up to 20 h helps to produce more polymer, but this is not reflected in the molecular weight determined by GPC, since the peak for the sample irradiated up to 20 h shifts to longer times with a maximum at ~9.6 min and thus a lower molecular weight (~582 g mol^{-1}). This may seem unusual, yet, we speculate that prolonged irradiation (20 h) leads to increased crosslinking, limiting the solubility in the THF mobile phase and as a result the molecular weight of the soluble fraction is lower. In fact, for the sample irradiated for 20 h, insoluble components were visible by turbidity and deposits the sides of the vials, suggesting high crosslinked polymers were excluded in the GPC samples.

Further, when comparing with thermal polymerization of cyclic disulfides, *e.g.*, 1,2-dithiane, it does not proceed at monomer concentrations below 4.0 M.[35] Thus, the concentration of the monomer is an important factor not only for the thermal polymerization,[36] but for the photopolymerization of cyclic disulfides, wherein specifically for LA, the amount of PALA decreased with a decrease of LA concentration. Even though, concentrations less than 5 mM might work for producing some PALA, the yield is lower compared with higher LA concentrations.

LA acts as a reducing and stabilizing agent

A common way to stabilize gold nanoparticles (AuNP) involves the formation of the thiolate S-Au bond, by performing reaction of thiols with the gold surface,[9] therefore, due to the inherently strong interactions between the AuNP and sulfur,[37] LA interacts and caps the AuNP surface. AuNPs were synthesized using a reported method[21] via reduction with the photoenol from 3,3,6,8-tetramethyl-1-tetralone with a lifetime around ~3 μs, which involves the carbonyl triplet state of the ketone (τ ~1.9 ns), as a precursor. In this particular case, the excited photoenol has biradical character and is useful for the fast synthesis of AuNP. The photolysis of the substituted tetralone was examined in acetonitrile solution using Laser Flash Photolysis (LFP) with a 355 nm laser excitation.[20] Briefly, 2 mL sample of 1 mM $HAuCl_4$ in 1:1 water:acetonitrile containing 10 mM substituted tetralone under nitrogen, was irradiated with a LED source centered at 368 nm (Figure S3.4.7, †ESI), leading to a characteristic plasmon band of AuNP (~550 nm) in less than one minute. A nice characteristic of photoenol reductions is that any intermediates that fail to reduce gold, regenerate the original tetralone precursor.[21] The TEM images show a nanoflower-like shape for the NPs with a plasmon peak that extends to longer wavelengths, which suggests aggregation and increased polydispersity (Figure S3.4.7, †ESI).

In an attempt to control particle growth and aggregation, LA was used as *in situ* stabilizer to control the particle size. Specifically, to the tetralone system described above, 0.2 mM, 0.5 mM, 1 mM, 2 mM of LA were added to the system before irradiation. Figure 3.2.5 shows the spectra of the AuNPs when adding LA as a stabilizer. Surprisingly, when LA was present in concentrations of 1 mM, more irradiation time was needed to see the change in solution colour from light-yellow to ruby red-purple and particularly, the width of the plasmon peak was reduced and shifted towards shorter wavelengths. Additionally, it is worth noting that when concentrations of 2 mM LA and higher were present as part of the reaction, no plasmon peak was observed, but a red shift of the absorbance took place, as shown by Figure 3.2.5.

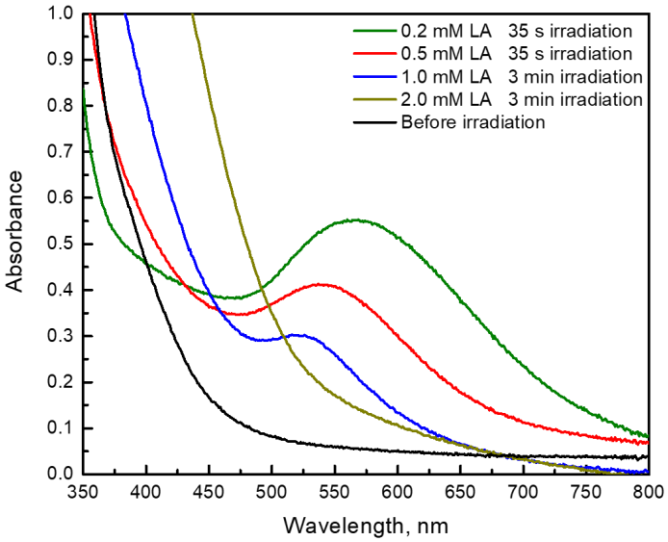

Figure 3.2.5. AuNP spectra obtained immediately after irradiation of 10 mM tetralone, 1 mM $HAuCl_4$, 0.2 mM, 0.5 mM, 1.0 mM, 2.0 mM LA in water-acetonitrile with UVA light (LED at 368 nm) for 35s and 3min of irradiation.

While concentrations of LA between 0.2-1 mM provide a well-defined plasmon peak between 530-575 nm, smaller particle sizes are obtained when increasing the concentration of LA in the system, as we can see in Figure S3.4.8 (†ESI). It is interesting how higher concentrations than 2 mM LA inhibited the formation of the plasmon peak of the nanostructures in this system. According to Bucher *et al.*,[19] LA can undergo photoexcitation when irradiated with UVA light, producing an excited triplet state with a lifetime of τ =75 ns. In this study, LFP was also used to monitor the LA radical species formed after UVA excitation and the results are consistent with a short-lived species like disclosed by Bucher *et al*[19] disclosed. The formation of a dithiyl radical and other radical species were observed in the reaction. Based on this, a question has been raised as whether LA could reduce Au in order to form plasmonic nanostructures. As shown in Figure 3.2.6, when a solution of 1 mM $HAuCl_4$ and 0.5 mM LA was irradiated using a 368 nm LED for a period of 30 min, a sharp plasmon peak is obtained with a maximum at 555 nm, with AuNP having circular and triangular-like shapes and a size around ~85 nm, as shown by the inset. This confirms that LA can reduce Au^{+3}. Furthermore, 0.2 mM and 1 mM LA were also tested along 1 mM $HAuCl_4$ and, remarkably, when having a concentration of 1

mM of LA in the system, the same trends of shifted absorption and no plasmon peak were observed, which confirms that concentrations of 1 mM LA and higher, allow LA to be polymerized under UVA light, wherein the process of polymerization is favored over the reduction of the metal ion.

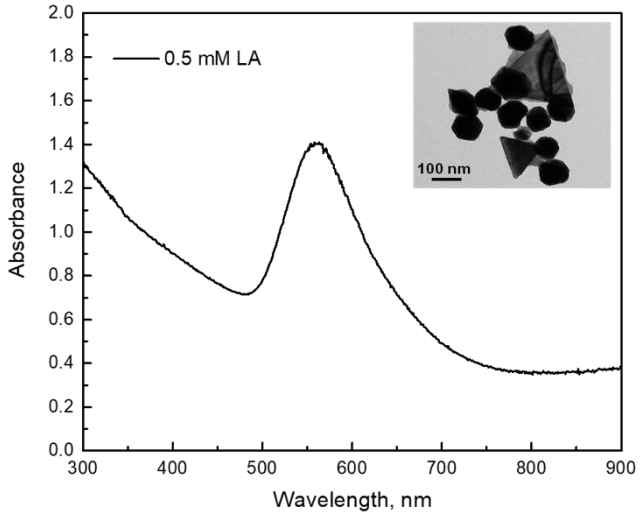

Figure 3.2.6. AuNP spectra obtained immediately after irradiation of sample containing 1 mM $HAuCl_4$, 0.5 mM of LA with a 368 nm LED., Inset: TEM image of Au NPs using 0.5 mM LA, 100 nm size bar.

Based on previous results, when the tetralone with triplet excited state of $\tau \sim 1.9$ ns[21] and the excited species of LA (2 mM or higher concentrations) are generated in the same system, both seem to compete to reduce Au, but due to the polymerization of LA into PALA, neither the tetralone nor the LA can play that role. Of course, higher LA concentrations will also compete with the tetralone for absorption of UVA photons. To the best of our knowledge, this is the first time that PALA oligomers of at least 5-6 monomer units has been observed under direct UVA irradiation. Nonetheless, the assumption that the polymerization of LA is taking place at concentrations higher than 2 mM in a system containing tetralone, might involve the formation of self-assembled structures of PALA encapsulating gold and inhibiting further reduction of the metal ions; this may explain why we do not observe a plasmon peak under these conditions. Therefore, in this particular case, LA acts as an *in-situ* stabilizer when being in concentrations no higher than 1 mM.

However, when going above this concentration of LA, plasmon generation fails, at least in part because tetralone fails to absorb enough light given the competition by LA.

PALA helps to control the size of plasmonic nanostructures

Considering the photochemical properties of LA, and a possible ring-opening polymerization upon UVA exposure, PALA was synthesized after irradiating 1 mM and 5.6 mM solutions of LA in $CHCl_3$ for 20 h using UVA light. The solvent was evaporated for one day in order to add 1:1 water:acetonitrile as this was a suitable media for the synthesis of AuNPs in the presence of the substituted tetralone. In a typical experiment under nitrogen, a 3 mL sample containing 10 mM tetralone (1 mL), 1 mM $HAuCl_4$ (1 mL) and PALA (1 mL), synthesized from 1 mM and 5.6 mM LA, was irradiated with a LED source centered at 368 nm. The PALA in this reaction included the high molecular weight fraction, in spite of its limited solubility. Figure 3.2.7 shows the spectra obtained after 3 min of UVA exposure. With this approach, i.e., by using PALA as an *in-situ* stabilizer in one-pot reaction, the onset of formation of nanoparticles was confirmed from the change in solution colour from light-yellow to purple and dark reddish (inset, Figure 3.2.7), since the substituted tetralone only competes for absorption of UVA photons when LA is present, but when PALA is the stabilizing agent, the substituted tetralone is the only light absorber.

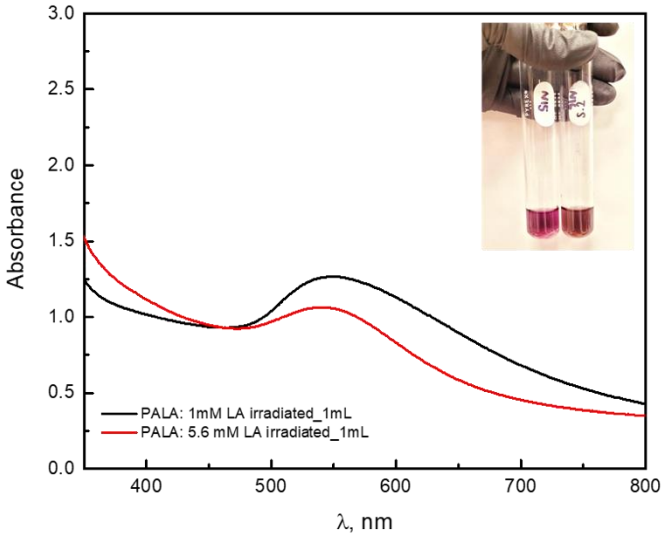

Figure 3.2.7. AuNP spectra obtained after irradiation of sample containing 10 mM tetralone, 1mM $HAuCl_4$, with PALA (1 mL) synthesized upon UVA exposure of 1 mM

and 5.6 mM LA for 20h. Inset: solutions of tetralone, $HAuCl_4$ and PALA synthesized after UVA irradiation of LA 5.6mM (left) and 1mM (right).

We observe that when PALA was synthesized after irradiating 5.6 mM LA with UVA light for 20h, the population of smaller AuNP of ~5-10 nm is higher, but structures of ~40 nm can also be formed (Figure S3.4.10, †ESI). On the other hand, when using PALA obtained upon exposure of LA 1 mM, the shape is also better well defined and particles of around ~20-40 nm are obtained (Figure S3.4.10, †ESI). This suggests that PALA can act as a stabilizing agent, capable of controlling size and agglomeration, passing from a nanoflower like-shape (when only the substituted tetralone and $HAuCl_4$ are part of the reaction) to a plasmonic nanostructures with a more regular shape as we can see in Figure S3.4.9 (†ESI). Likewise, amounts lower than 1 mL of 1 mM and 5.6 mM PALA solutions were used and amounts of 200 µL were tested, and as expected, a reduction in the agglomeration of the nanostructures was also observed with a maximum of 550 nm in the plasmon peak, as shown by Figure 3.2.8 and different sizes of the nanostructures can also be obtained.

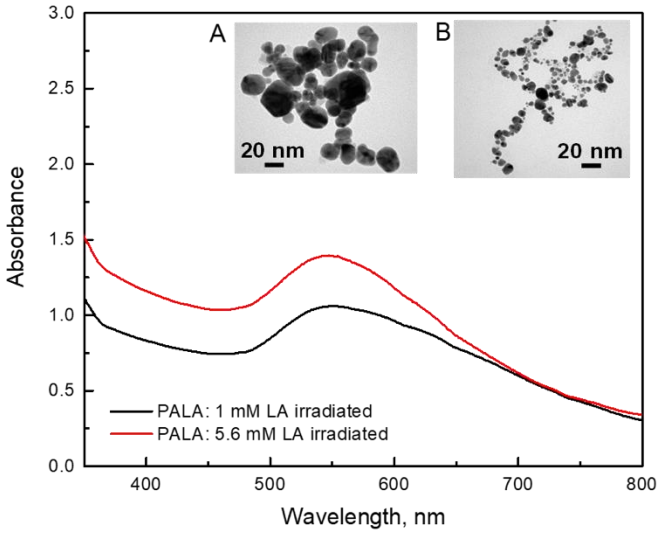

Figure 3.2.8. AuNP spectra obtained after 2-3 min irradiation of 1 mL of 10 mM tetralone, 1 mL of 1 mM $HAuCl_4$ and PALA (200 µL) synthesized upon UVA exposure. Light scattering contributes to a vertical shift of the spectra. Inset: A. TEM image from reaction

containing PALA derived from 20h irradiation of 1 mM LA solution **(A)** and 5.6 mM LA **(B)**.

Thus, amounts of about 200 μL – 1 mL from a solution of PALA derived upon exposure of LA 1 mM and 5.6 mM for 20 h into the system that contains 10 mM substituted tetralone (1 mL) and 1 mM $HAuCl_3$ (1 mL) in 1:1 water:acetonitrile, work to reduce the size of Au nanostructures, if the polymer is used *in-situ*, as in this case only the substituted tetralone will play the role of the photoinitiator. Additionally, polymers such as PALA, can reduce the agglomeration of particles, especially when synthesized after irradiating LA in concentrations higher than 1 mM. This relies on the fact that when increasing the steric hindrance of capping agents, the size of the nanoparticles becomes smaller. Moreover, enhancement in polymer to metal molar ratio from 1:1 to 1:5 results in smaller nanostructures.

Conclusions

In conclusion, beyond its role in biology and its proposed health applications,[38, 39] lipoic acid and its oligomers and polymers (PALA) are of interest in the synthesis of gold nanostructures where they can be used to stabilize gold nanostructures, to control their size and to provide the enhanced stability that the “two-feet” binding approach enables. This can be combined with the use of photoenolizable tetralones that make it possible to generate gold nanostructures easily and quickly. Among photoinitiated molecules capable of reducing gold, tetralones offer the unique advantage that if reaction intermediates fail to reduce gold, they return to the initial tetralone precursor, thus minimizing chemical debris.[21] In addition to its applications in nanoscience, this contribution presents an improved understanding of the photochemistry of lipoic acid, something that may contribute to its biological and health applications.

Experimental

Materials and methods

All chemicals (3,3,6,8-tetramethyl-1-tetralone, Gold(III) chloride trihydrate, Chloroform, Tetrahydrofuran were purchased from Sigma Aldrich. HPLC grade acetonitrile and Milli Q water were used.

Standard laboratory techniques

Synthesis of PALA. The polymer was obtained by using 1 mM and 5.6 mM LA solutions in chloroform. The solutions were irradiated in Pyrex tubes inside of a Luzchem photoreactor equipped with 12 UVA light lamps corresponding to an irradiance of 70-80 W/m^2 (see Figure S3.4.1 for the emission spectrum).

Synthesis of AuNP. The photochemical generation of AuNP using 3,3,6,8-tetramethyl-1-tetralone and Lipoic Acid polymer (PALA) and Lipoic Acid itself was performed under UVA (368 nm) irradiation using a LED at max power (~ 629 W m^{-2}, see Figure S3.3.10 for the emission spectrum) in a Pyrex test tube.

Characterization

UV–Vis spectra of the AuNP were obtained using an Agilent Cary 100 UV–Vis spectrometer. Transmission electron microscopy (TEM) images were collected on a JEM2100F FETEM (JEOL) operating at 200 kV. DLS spectra were obtained with a Malvern Zetasizer Nano with a 633 nm laser (DPSS, 50 mW). ^{1}H NMR spectra were recorded in a Bruker AVANCE II 400 MHz spectrometer using deuterated chloroform as solvent. The MS spectra were analyzed by electrospray ionization tandem mass spectrometry (ESI) (Agilent 6125B single quadrupole LC/MSD system), using acetonitrile as the solvent. Gel Permeation Chromatography with an Agilent PL Gel 5 μm MIXED-C column (Agilent Technologies 380-ELSD and 1260 Infinity) was used to obtain the GPC curves of LA and samples of 5.6 mM LA upon 40 min and 20h of UVA exposure respectively. For Gel Permeation Chromatography, the solvent used was tetrahydrofuran (THF) HPLC grade.

Conflicts of interest

There are no conflicts to declare.

Acknowledgments

This work was supported by the Natural Sciences and Engineering Research Council, the Canada Foundation for Innovation and the Canada Research Chairs program.

3.3. References

1. B. C. Scott, O. I. Aruoma, P. J. Evans, C. O'neill, A. Van Der Vliet, C. E. Cross, H. Tritschler and B. Halliwell, *Free Radical Research*, 1994, **20**, 119–133.

2. H. Moini, L. Packer and N. E. L. Saris, *Toxicology and Applied Pharmacology*, 2002, **182**, 84–90.

3. L. Packer and E. Cadenas, *Journal of Clinical. Biochemistry. Nutrition*, 2011, **48**, 26–32.

4. B. Salehi, Y. Berkay Yılmaz, G. Antika, T. Boyunegmez Tumer, M. Fawzi Mahomoodally, D. Lobine, M. Akram, M. Riaz, E. Capanoglu, F. Sharopov, N. Martins, W. C. Cho and J. Sharifi-Rad, *Biomolecules*, 2019, **9**, 356.

5. K. Kim, J. Kim, H. Kim and G. Y. Sung, *International Journal of Molecular Sciences*, 2021, **22**, 2160.

6. M. Podda, M. Rallis, Maret, G. Cuber, L. Packer and H. Maibachl, *Biochemical Pharmacology*, 1996, 52, 627–633.

7. T. P. A. Devasagayam A'b, M. Subramanian, D. S. Pradhan and H. Sies, *Chemico-Biological Interactions*, 1993, 86, 79–92.

8. Y. J. Suzuki, M. Tsuchiya and L. Packer, *Free Radical Research Communications*, 1991, **15**, 255–263.

9. H. Häkkinen, *Nature Chemistry*, 2012, **4**, 443–455.

10. A. Mahmoud Asadirad, Z. Erno and N. R. Branda, *Chemical Communications*, 2013, **49**, 5639–5641.

11. A. Bard, R. Rondon, D. T. Marquez, A. E. Lanterna and J. C. Scaiano, *Photochemistry and Photobiology*, 2018, **94**, 1109–1115.

12. S. Matsugo, D. Han, H. J. Tritschler and L. Packer, *Biochemistry and Molecular Biology International*, 1996, **38**, 51–59.

13. A.F. Wagner, E. Walton, G.E. Boxer, M.P. Pruss, F.W. Holly, and K. Folkers, 1956, **78**, 5079–5081.

14. J. G. Affleck and G. Dougherty, *Journal of Organic Chemistry*, 1950, 15 865–868

15. Phyllis R. Brown and Jhon O. Edwards, *Journal of Organic Chemistry*, 1969, 34, 3131–3135.

16. Phyllis R. Brown and John O. Edwards, *Journal of Chromatography*, 1969, **43**, 515–518.

17. Bradley D.F. and Calvin M, *Proceedings of the National Academy of Sciences of the United States of America*, 1955, **41**, 563–571.

18. L. J. ; J. A. Barltrop, P. M. Hayes and M. Calvin, *Journal of the American Chemical Society*, 1954, 34, 4348–4367.

19. G. Bucher, C. Lu and W. Sander, *ChemPhysChem*, 2005, **6**, 2607–2618.

20. S. Simoncelli, H. De Alwis Weerasekera, C. Fasciani, C. N. Boddy, P. F. Aramendia, E. I. Alarcon and J. C. Scaiano, *Journal of Physical Chemistry Letters*, 2015, **6**, 1499–1503.

21. M. Cely-Pinto and J. C. Scaiano, *Photochemical and Photobiological Sciences*, 2021, **20**, 1611–1619.

22. C. C. Li, S. J. Chang, F. J. Su, S. W. Lin and Y. C. Chou, *Colloids and Surface A Physicochemical Engineering Aspects*, 2013, **419**, 209–215.

23. C. V. Restrepo and C. C. Villa, *Environmental Nanotechnology Monitoring & Management*, 2021, **15**, 100428.

24. R. Javed, M. Zia, S. Naz, S. O. Aisida, N. ul Ain and Q. Ao, *Journal of Nanobiotechnology*, 2020, **18**, 172.

25. M. Gao, L. Sun, Z. Wang and Y. Zhao, *Materials Science and Engineering C*, 2013, **33**, 397–404.

26. I. Hussain, M. Brust, A. J. Papworth and A. I. Cooper, *Langmuir*, 2003, **19**, 4831–4835.

27. R. G. Shimmin, A. B. Schoch and P. V. Braun, *Langmuir*, 2004, **20**, 5613–5620.

28. A. Alli, B. Hazer and B. M. Baysal, *European Polymer Journal*, 2006, **42**, 3024–3031.

29. Arima T, Hamada T and McCabe J.F., *Journal of Dental Research*, 1995, **74**, 1597–1601.

30. Z. Liu, N. Shen, Z. Tang, D. Zhang, L. Ma, C. Yang and X. Chen, *Biomaterials Science*, 2019, **7**, 2803–2811.

31. Kisanuki A, Kimpara Y, Oikado Y, Kado N, Matsumoto M and Endo K, *Journal of Polymer Science*, 2010, **48**, 5247–5253.

32. N. Wada, H. Wakami, T. Konishi and S. Matsugo, *Journal of Clinical Biochemistry Nutrition*, 2009, **44**, 218–222.

33. K. Endo and T. Yamanaka, *Macromolecules*, 2006, **39**, 4038–4043.

34. Z. Niu and H. W. Gibson, *Chemical Reviews*, 2009, **109**, 6024–6046.

35. K. Endo, T. Shiroi and N. Murata, *Polymer Journal*, 2005, **37**, 512–516.

36. S. J. Clarson and J. A. Semlyen, *Polymer*, 1986, **27**, 91–95.

37. Y. Xue, X. Li, H. Li and W. Zhang, *Nature Communications*, 2014, **5**, 4348.

38. J. W. Trzciński, L. Morillas-Becerril, S. Scarpa, M. Tannorella, F. Muraca, F. Rastrelli, C. Castellani, M. Fedrigo, A. Angelini, R. Tavano, E. Papini and F. Mancin, *Biomacromolecules*, 2021, **22**, 467–480.

39. M. Dzwonek, D. Załubiniak, P. Piatek, G. Cichowicz, S. Męczynska-Wielgosz, T. Stępkowski, M. Kruszewski, A. Więckowska and R. Bilewicz, *RSC Advances*, 2018, **8**, 14947–14957.

3.4. Post-print Version of Supporting Information

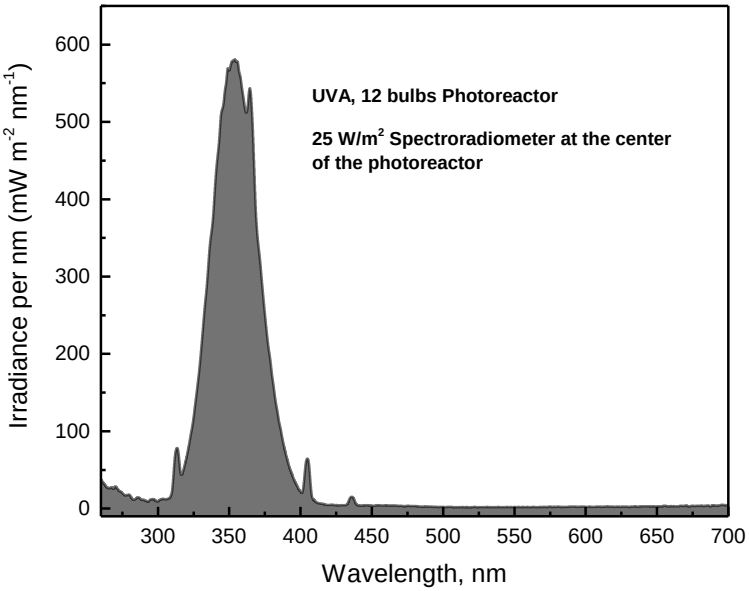

Figure S3.4.1. Spectral Irradiance of a Luzchem photoreactor equipped with 12 UVA light lamps.

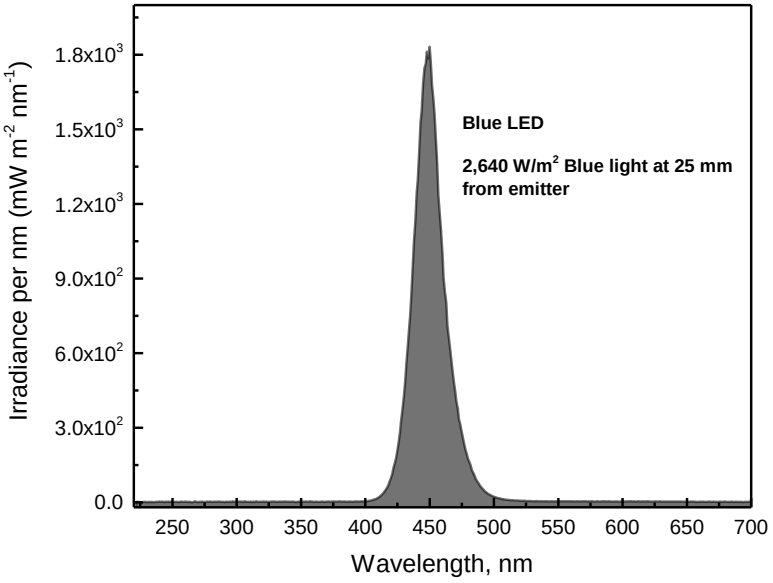

Figure S3.4.2. Spectral Irradiance of blue Luzchem LED.

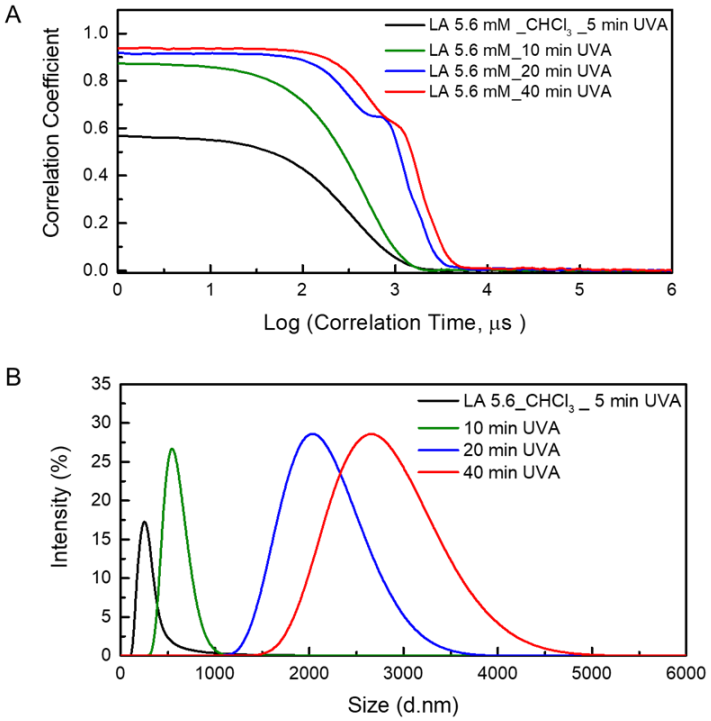

Figure S3.4.3. DLS correlation function measured at 20°C as a function of correlation time: 5.6 mM LA solution in $CHCl_3$ irradiated with UVA light at different times (10 min, 20 min, 40 min) **(A)**; Number-weighted diameters of same sample at different UVA irradiation times **(B)**.

Table S3.4.1. Z-average diameter, DLS measurement of 1mM LA sample in H_2O before, upon specific irradiation times (UVA) and after addition of DMSO as an organic solvent.

Solvent	**Sample Name**	**Z-avg. Diamenter, nm**
H_2O	LA_1 mM_H_2O	73.5
	LA_1 mM_40 min UVA	125.1
	LA_1 mM_Addition of DMSO	301.8

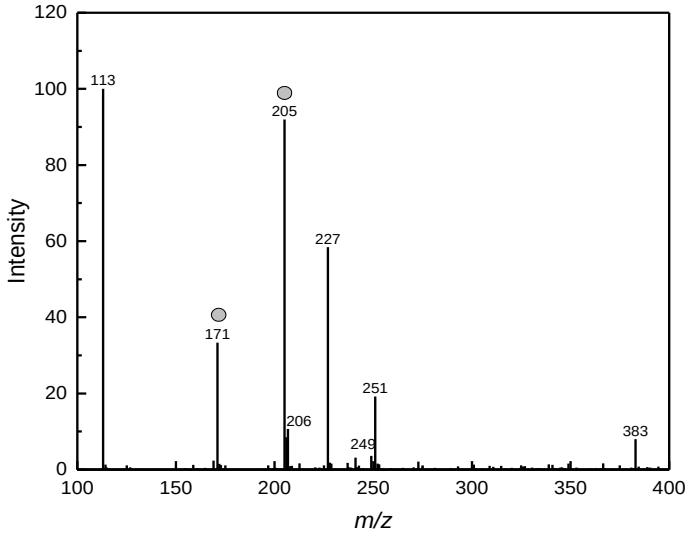

Figure S3.4.4. ESI-MS spectrum of 5.6 mM LA solution in acetonitrile showing characteristic molecular ion m/z 205 and $[M\text{-}H_2S\text{-}H]^-$ m/z 171, negative mode.

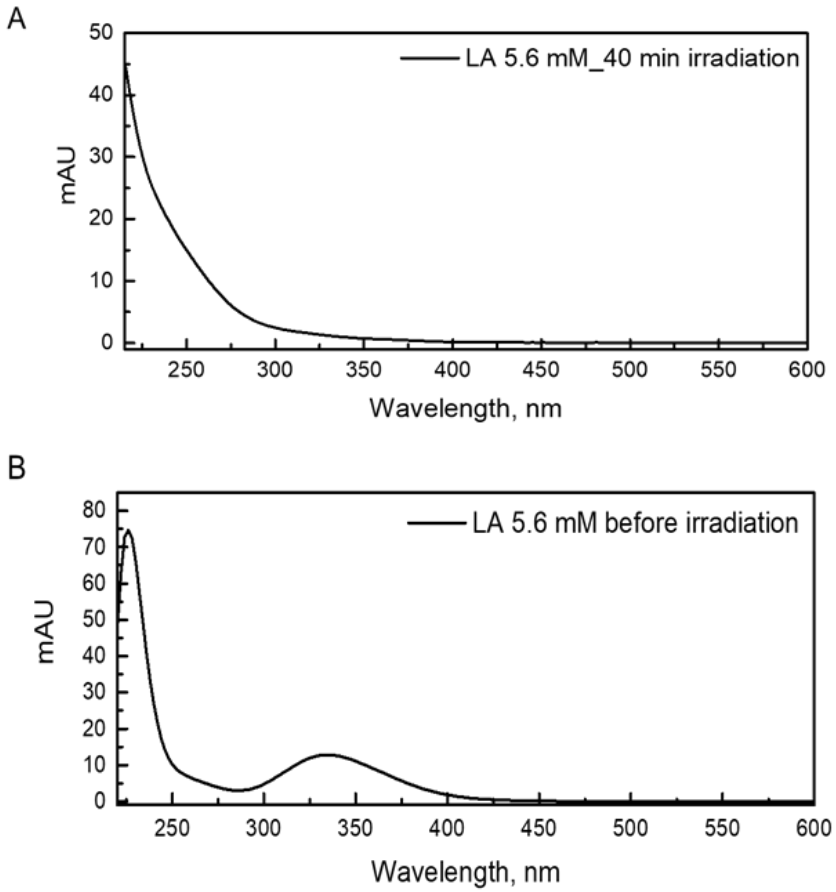

Figure S3.4.5. UV Vis spectra obtained from GPC curves of 5.6 mM LA upon 40 min UVA exposure. From the peak at 9.5 min from GPC Curve of LA irradiated for 40 min with UVA light in Figure 4b, the spectrum in A is obtained and it shows the disappearance of the characteristic band at 330 nm for LA **(A)**. Figure B is obtained from the peak at 10. 5 min from GPC curve of LA 5.6 mM before any irradiation of Figure 4B which clearly shows the band of LA around 330 nm **(B)**.

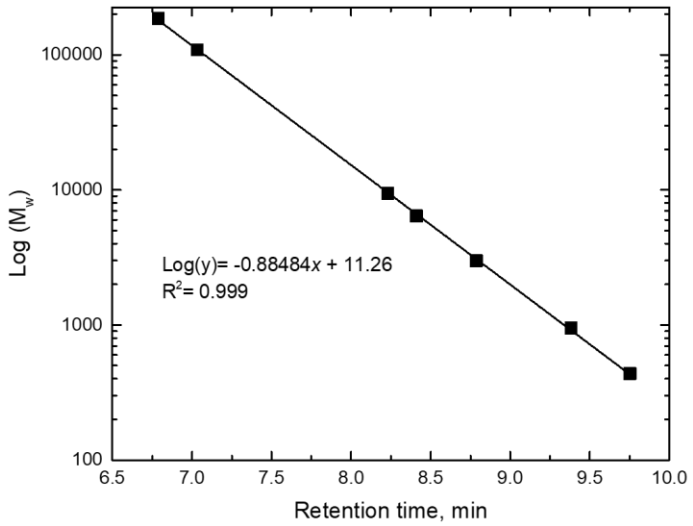

Figure S3.4.6. Gel Permeation Chromatography (GPC) calibration curve GPC using polystyrene standards with Mw of 436, 852, 2790, 6390, 9650, 18300, 109000 and 186000 at 1 mM concentration in THF HPLC grade.

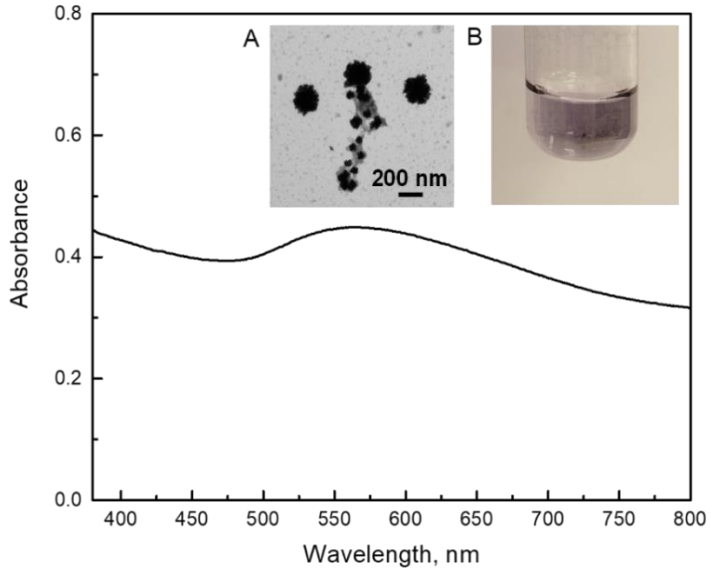

Figure S3.4.7. UV Vis spectrum of AuNP when using 3,3,6,8-tetramethyl-1-tetralone 10 mM and $HAuCl_4$ 1 mM in 1:1 water:acetonitrile, under 35 s UVA LED 368 nm. This

spectrum has a high level of light scattering, leading to a shifted baseline. Inset: TEM image Au NPs **(A)**, colour of AuNPs immediately after irradiation **(B)**.

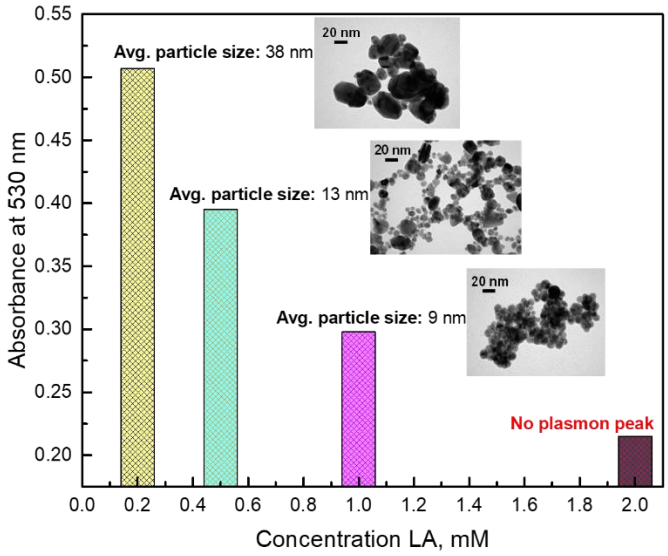

Figure S3.4.8. Absorbance at 530 nm and TEM images of AuNP from the system containing 10 mM substituted tetralone, 1 mM $HAuCl_4$, and different concentrations of LA: 0.2 mM, 0.5 mM, 1.0 mM, 2.0 mM in water-acetonitrile. UVA light (368 nm) was used for 35 s to obtain the AuNP for the systems containing LA concentrations of 0.2 mM, 0.5 mM and 3 min of irradiation for 1.0 mM and 2 mM. The sample with 2 mM LA was also exposed up to 1 h in order to see any changes but no AuNPs were obtaining either. All the TEM images have a scale of 20 nm.

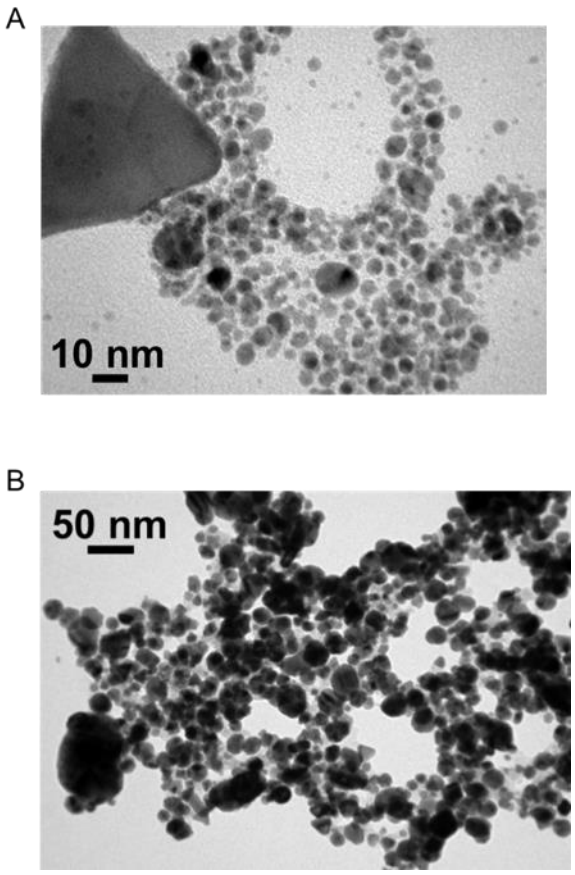

Figure S3.4.9. TEM images of AuNP containing 10 mM substituted tetralone, 1 mM $HAuCl_4$ and 1 mL of PALA synthesized upon UVA exposure (~2-3 min). AuNPs obtaining when the system contains PALA derived from 20 h irradiation of 5.6 mM LA solution **(A)** and 1 mM LA **(B)**.

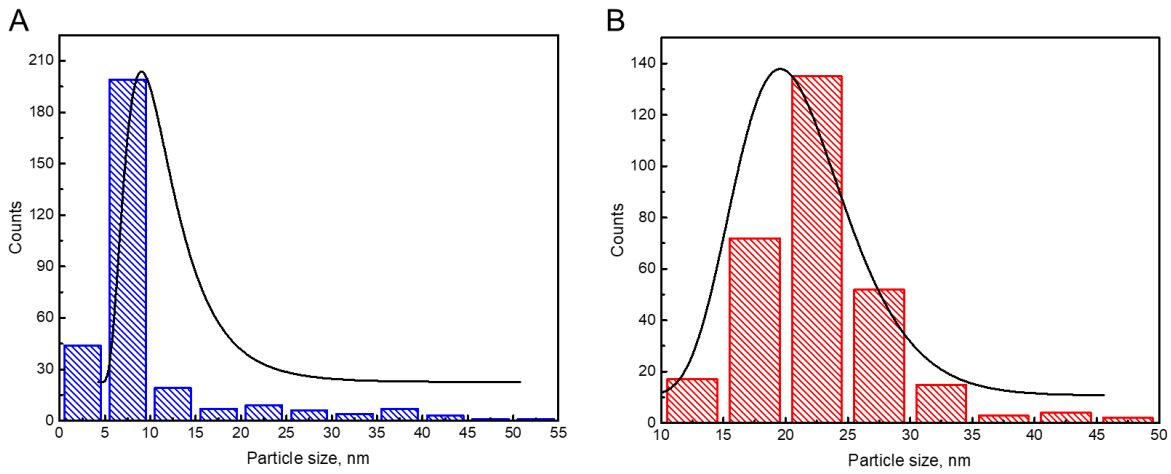

Figure S3.4.10. Particle size distribution histograms for AuNP obtained from the system containing 10 mM substituted tetralone, 1 mM $HAuCl_4$ and 1 mL of PALA synthesized upon UVA exposure (~2-3 min). AuNPs obtaining when the system contains PALA derived from 20 h irradiation of 5.6 mM LA solution **(A)** and 1 mM LA **(B)**. These histograms correspond to the NP depicted in Figure S3.3.9. Particle size distribution histograms were generated by analyzing the area of the AuNPs through individual counting using ImageJ software. These histograms illustrate the number of particles that fall within specific size ranges (in nm).

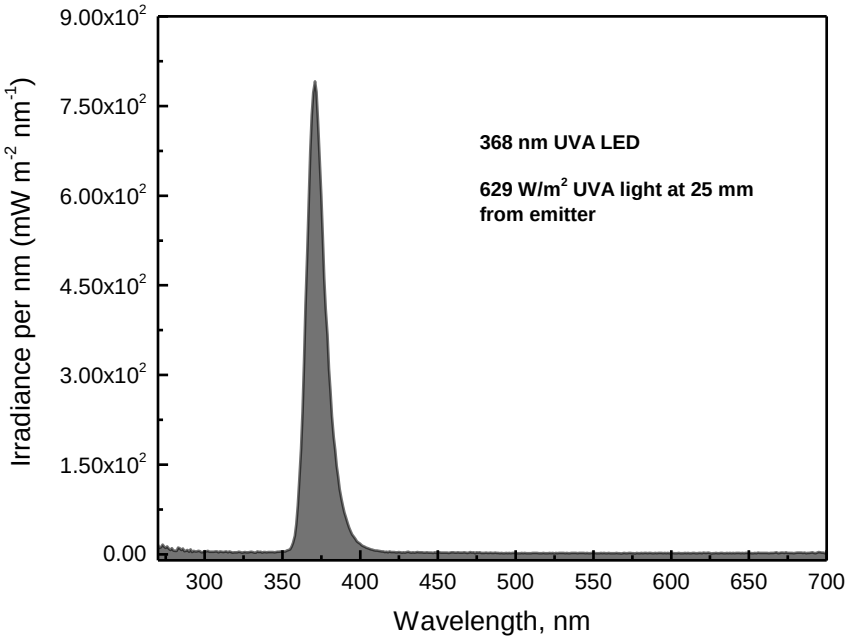

Figure S3.4.11. Spectral Irradiance of 368 nm Luzchem LED.

4. Photocatalytic Semi-Hydrogenation of Alkynes: A Game of Kinetics, Selectivity and Critical Timing

4.1. Preamble to chapter 4

This chapter focuses on the semi-hydrogenation of alkynes, which is a fundamental process in different industries, particularly, in the manufacture of bulk and fine chemicals. This process is essential for converting alkynes into alkenes, a fundamental step in synthesizing complex organic molecules. Ideally, this transformation must be achieved with high efficiency and selectivity to minimize costs and reduce environmental impact. However, a major challenge in this reaction is controlling the hydrogenation process to prevent the over-hydrogenation product corresponding to the alkane. Traditional photocatalysts based on palladium (Pd) have shown a tendency to proceed all the way to the alkane moiety, needing precise reaction timing to stop at the desired alkene product with high selectivity. This precision is difficult to achieve under typical laboratory conditions where reactions are often monitored over hours or even overnight, rather than in real-time with continuous monitoring.

In this chapter, the use of Cu@TiO_2 as a photocatalyst for semi-hydrogenation reactions is studied, when using either ethanol (EtOH) or methanol (MeOH) as hydrogen donors and UVA light. Despite operating at slower kinetics compared to Pd-based catalysts like Pd@TiO_2, Cu@TiO_2 demonstrates remarkable selectivity, achieving conversions with over 95% selectivity towards alkenes. This high selectivity is essential for minimizing waste and optimizing the use of starting materials. However, the reaction time required for Cu@TiO_2 was approximately 16 hours whereas Pd@TiO_2 completed the reaction in just 1 hour, of course, Pd@TiO_2 leads to the formation of the alkane moiety. Therefore, to enhance the kinetics of the reaction while maintaining high selectivity, a novel bimetallic catalyst, CuPd@TiO_2, containing 0.8% copper (Cu) and 0.05% palladium (Pd) was used. Using MeOH as a hydrogen source, CuPd@TiO_2 accelerates reaction rates by 50% compared to Cu@TiO_2, while retaining exceptional selectivity towards alkenes. Importantly, the low Pd content in CuPd@TiO_2 mitigates

concerns over the environmental impact of this metal, an element considered at risk of depletion due to its extensive use in various chemical processes. Unlike conventional catalysts, which often require complex organic ligands to prevent over-hydrogenation products, the bimetallic catalyst studied in this chapter, CuPd@TiO_2, achieves high selectivity through a mechanism that minimizes unwanted side reactions. Additionally, this study also highlights the essential role of light activation in photocatalytic processes such as this one. Light helps to initiate the reaction, and thus the importance of optimizing light conditions to maximize catalytic efficiency was also considered.

In the mechanism proposed in this study when using CuPd@TiO_2, hydrogen atoms generated on the Pd surface are transferred to copper, facilitating the selective conversion of alkynes to alkenes, keeping excellent rates and selectivity at the same time. Consequently, the bimetallic catalyst, CuPd@TiO_2, represents a significant advancement in semi-hydrogenation catalysis, offering a sustainable solution with improved efficiency and selectivity over traditional Pd-based systems.

4.2. Postprint Version of Manuscript

First published in: Nanomaterials, **2023**, 13, 2390.

Abstract

The reaction of semi-hydrogenation of alkynes is important in the fine chemicals and pharmaceutical industries, and it is thus important to find catalytic processes that will drive the reaction efficiently and at a low cost. The real challenge is to drive the alkyne-to-alkene reaction avoiding over-hydrogenation to the saturated alkane moiety. The problem is more difficult when dealing with aromatic substitution at the alkyne center. Simple photocatalysts based on Palladium tend to proceed to the alkane and stopping at the alkene with good selectivity requires very precise timing with basically no timing tolerance. We report here that the goal of high conversion with high selectivity can be achieved with TiO_2-supported copper (Cu@TiO_2), although with slower kinetics than for Pd@TiO_2. A novel bimetallic catalyst, CuPd@TiO_2 (0.8% Cu and 0.05% Pd) with methanol as the hydrogen source can improve the kinetics by 50% with respect to

$Cu@TiO_2$, while achieving selectivities over 95%, and with exceptional timing tolerance. Further, the low Palladium content minimizes its use, as Palladium is regarded as an element at risk of depletion.

Keywords: photochemistry, heterogeneous catalysis, semi-hydrogenation, supported catalysts,

Introduction

Semi-hydrogenation of alkynes to alkenes is one of the most important reactions in several industrial processes. Among the different hydrogenation reactions, the semi-hydrogenation of alkynes to alkenes is particularly challenging and important to the manufacture of bulk and fine chemicals. These reactions are commonly performed over supported Pd catalysts which can be modified by the addition of different metals, including silver,[1] or even using CO which can act as a reversible poison.[2,3] For example, reports have shown that semi-hydrogenation of phenylacetylene has been performed using Pd nanoparticles in the forms of dispersed colloids [4] and supported systems.[5,6] The latter is more commercially attractive for industrial applications given their better handling properties, including post-reaction separation and therefore, the development of heterogeneous catalysts with interesting compositions, high selectivity and catalytic efficiency will contribute to sustainable chemistry.[7] Different approaches have been explored, such as the one disclosed by Soberanas *et al.*,[8] who synthesized solid-supported $Pd\text{-}(CaCO_3)_n$ clusters showing a high catalytic activity for the semi-hydrogenation of internal alkynes compared to terminal alkynes, wherein, for example, internal aliphatic alkynes were faster reacting with the catalyst than the aromatic ones. On the other hand, Wang *et al.*[9] proposed Pd-Se nanocrystals to enable the semi-hydrogenation of phenylacetylene to styrene demonstrating the σ-π associative adsorption of the C≡C bond but suppressing the hydrogenation of C=C bond which results in high selectivity. Zheng *et al.* [10] have also worked with Pd, but in their case, they demonstrate that alloyed Pd-Pb on precipitated calcium carbonate (PCC) supports could be an upgraded version of the Lindlar catalyst that provides promising results for the semi-hydrogenation of

phenylacetylene to styrene. Also, Lv *et al.*,[11] developed a novel alumina supported Pd catalyst for selective hydrogenation of phenylacetylene and less production of the byproduct ethylbenzene given the good dispersion of Pd and strong metal-support interaction capable of creating more active sites for hydrogenation and facilitating the desorption of the alkene.

However, even though different investigations have focused on increasing the selectivity of alkenes using different materials, the conversion of alkynes to alkanes is a straightforward process and can be performed quite efficiently if other moieties other than the target alkyne are not affected in the process. Therefore, heterogeneous photocatalysts based on palladium over TiO_2 could be an alternative to the disclosed ones since they show excellent performance and the control over the light source might help during these processes. Different alternatives directed to depositing metals over TiO_2 have also been explored as an effective approach to different materials in semi-hydrogenation reactions given its photon harvesting capacity and the increased charge separation that helps improve the semiconductor photocatalyst activity.[12] For example, such is the case for TiO_2 decorated with palladium nanoparticles (Pd@TiO_2). Some catalysts, like Pd@TiO_2, are excellent, and while the rate of first step k_1 tends to be faster than k_2, in reality, it is very difficult to stop at the critical point in time that achieves high selectivity. This is conceptually illustrated in Figure S4.4.1, where even if k_1 is 10 times faster than k_2 (panel B), only about 70% selectivity and also about 70% alkene yield is obtained at 99% conversion. In contrast, when k_2 is 100 times slower than k_1 (panel C), the selectivity and yield are about 97% at 99% conversion. In other words, an alkene-selective catalyst must show very slow hydrogenation of alkenes, while having an acceptable rate constant for alkyne hydrogenation.

Figure S4.4.1 is based on a very simple kinetic simulation where the total time is equal to 5 lifetimes for the reagent decay by first-order kinetics, reducing its concentration approximately 150 times. Heterogenous catalysis may not follow as simple a kinetic model, but in any event, Figure S4.4.1 serves to illustrate the point. The expression "critical timing" used in the title relates to cases where it is possible to achieve reasonable selectivity in very fast reactions only if the reaction is stopped at a very precise time while

letting the reaction go for a bit longer (e.g. 20% longer) totally destroys the selectivity. The reality of the organic chemistry laboratory is that reaction times must be somewhat forgiving as reaction times are measured in hours or overnight and rarely on continuous real-time monitoring of the reaction mixture composition.

Based on the above, semi-hydrogenation of alkynes can be a challenging process, as one would like to combine reasonable activity with high selectivity, such as illustrated in Scheme 4.2.1 for the case of 1-phenyl-1-propyne.

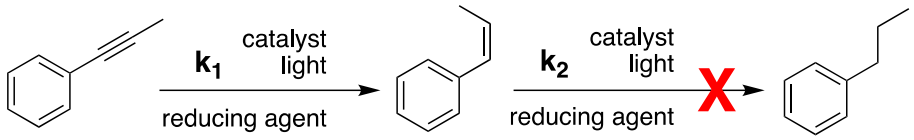

Scheme 4.2.1. Reaction path for semi-hydrogenation of 1-phenyl-1-propyne (PhP) using a photocatalyst. In an ideal situation $k_2 << k_1$.

On the other hand, other than Pd, different metals have been used in these reactions, for example, Cu on TiO_2 (Cu@TiO_2) has shown sharp chemoselectivity when hydrogenated internal alkynes to alkenes without being further hydrogenated to alkanes.[13] However, according to Imai *et al.* when performing photocatalytic semi-hydrogenation of alkynes with Cu-Pd on TiO_2 (CuPd@TiO_2), the reaction works very well with aliphatic systems, but for example for 1-phenyl-acetylene in 2-propanol the selectivity is reduced to 66% due to ongoing hydrogenation to ethylbenzene.[14]

In this sense, the time of the reaction might be improved using a combination of two different elements. Additionally, beyond the hydrogenation kinetics on the surface of the catalyst, it is important to consider that selectivity is also controlled by the adsorption strength and configuration of the reactants and intermediates on the surface of catalysts,[15] and those are parameters to consider when performing these reactions. Consequently, the ideal catalyst should prevent the over-hydrogenation of the formed alkene while keeping acceptable reaction rates, selectivity, and reactivity of the catalysts in these reactions.

Here we compare catalysts based on Pd or Cu on TiO_2 (Pd@TiO_2 and Cu@TiO_2) as well as the mixture of both metals on TiO_2 (CuPd@TiO_2), with the last one prepared by

galvanic exchange. We examine several alkynes, but frequently concentrate detailed studies on 1-phenyl-1-propyne. All measurements have included a detailed time profile showing the evolution of the reaction, avoiding end-point studies where conversions and selectivity measurements can reflect a poor choice of reaction times, or irradiance values. The solvents and hydrogen donors are ethanol (EtOH) and methanol (MeOH) and the reactions are driven by UVA irradiation, a spectral region largely absorbed by TiO_2.

Results and discussion

We have tested three different catalysts and several alkynes. For selected combinations we have also examined the adsorption of the alkynes on the different materials, something that earlier work has shown to be very important.[15] Finally, we look at the catalytic properties of the materials, and in all cases, we examine in detail the time dependence. As Figure S4.4.1 illustrates, both conversion and selectivity are critically dependent on time and thus end-point analysis is not particularly informative.

Catalyst synthesis

Pd@TiO_2: Based on a reported synthesis.[16,17,18] Approximately 15 mg of metal precursor salt ($PdCl_2$) was mixed together with TiO_2 (~500 mg) in 150 mL of Milli-Q water and sonicated for 20 minutes. The slurry was irradiated in a Luzchem photoreactor equipped with 14 UVA bulbs for 24h with vigorous stirring in a crystallizing Pyrex® dish with a Pyrex® cover. The slurry was centrifuged and washed with Milli-Q water for four times to remove unreacted metal precursor salt and dried overnight in a desiccator under vacuum. The obtained powder has a dark grey colour.

Cu@TiO_2: Based on a reported synthesis,[19] 33 mg of $CuCl_2 \cdot 2H_2O$ were mixed together to TiO_2 (~500 mg) and 80 mg of Irgacure-2959 in 130 mL of Milli-Q water and purged with argon for 15 minutes. After this, the slurry was irradiated in a Luzchem photoreactor equipped with 14 UVA bulbs for 24 h with vigorous stirring. The slurry was filtered and washed with Milli-Q water at least seven times to remove unreacted metal precursor salt and dried overnight in a desiccator under vacuum. The powder has an intense beige colour with green tones.

CuPd@TiO_2: The catalyst was done through galvanic replacement synthesis which relies on the spontaneous redox reaction between the atoms of a substrate (Cu@TiO_2 previously synthesized) and the salt precursor ($Pd(acac)_2$ in this case) of another metal. Specifically, 0.28 mg of $Pd(acac)_2$ was mixed with 20 mL of Milli-Q water and sonicated for 15 min. After completing this, 10 mL of the solution was taken and mixed with 50 mg of Cu@TiO_2. The slurry was purged with argon for 15 min and vigorously stirred overnight. The slurry was filtered and washed with Milli-Q water at least seven times and dried overnight in a desiccator under vacuum. The powder has a similar colour to the one from Cu@TiO_2.

Characterization

PdNP morphologies were approximately spherical. Transmission electron microscopy (TEM) images and a histogram for PdNPs are displayed in Figure 4.2.1. Additionally, for Cu@TiO_2 and CuPd@TiO_2, Scanning electron microscopy (SEM) and Energy-dispersive X-ray spectroscopy (EDS) *were* used to determine the presence of Cu and Pd in the catalysts. The TEM image of Pd@TiO_2 nanoparticles in panel A of Figure 4.2.1 shows a mean particle size of 3.0 ± 0.2 nm. On the other hand, according to EDS results of panels B and C of Figure 4.2.1, for Cu@TiO_2 and CuPd@TiO_2 the *presence* of Cu was identified for both catalysts, but the peak of Pd for CuPd@TiO_2 was not possible to identify since the loading of this metal was too little (Table 4.2.1). X-ray photoelectron spectroscopy (XPS) analyses of Pd@TiO_2 and Cu@TiO_2 have been conducted and published in previous publications, suggesting the presence of PdO with a small contribution of more reduced palladium species for Pd@TiO_2,[18] and satellite peaks of Cu (II).[20] In this context, it is important to highlight that Cu@TiO_2 primarily contains CuO, which corresponds to Cu (II). When the material is excited through irradiation, Cu(I) is generated, indicating that copper has been reduced. While this suggests that reduction to Cu(I) has occurred, it does not rule out the possibility of Cu(0) also being present.

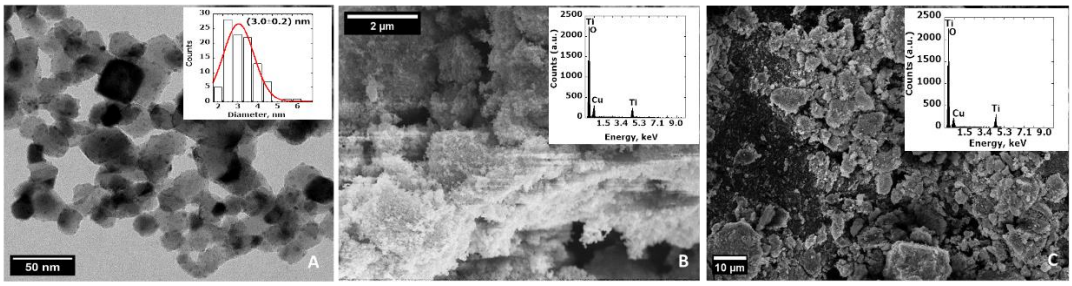

Figure 4.2.1. (A) TEM image of Pd@TiO_2 nanoparticles (histogram made with 100 particles (size bar is 50 nm). The mean particle size is 3.0 ± 0.2 nm. **(B)** SEM and EDS results for Cu@TiO_2. EDS results show the peaks for Ti, O and Cu, confirming the presence of Cu in the catalyst. **(C)** SEM and EDS results for CuPd@TiO_2. EDS results show the peaks for Ti, O and Cu, which corroborate the presence of Cu in the catalyst. However, the peak for Pd was not possible to identify since the loading of this metal was too low (0.05% according to ICP).

The metal loadings were determined by Inductively Coupled Plasma Optical Emission Spectroscopy (ICP-OES) analysis and are disclosed in Table 4.2.1.

Table 4.2.1. ICP-OES analysis of the catalysts before performing the adsorption experiments and semi-hydrogenation reactions.

Material	**Metal loading (%)**
Pd@TiO_2	2.0 wt % Pd
Cu@TiO_2	0.9 wt % Cu
CuPd@TiO_2	0.8 wt % Cu & 0.05 wt % Pd

Alkyne adsorption on selected materials

Alkyne adsorption experiments are essential when looking at catalyzed reactions given that they might occur at the catalyst surface. In the present work, adsorption experiments were performed using two representative alkynes, 900 ppm solutions of phenylacetylene (PhA) and 1-phenyl-1-propyne (PhP) are stirred for 40 minutes in the presence of 10 mg of each material in EtOH. Preliminary experiments showed that 40

minutes was an adequate time to reach a plateau, that is, adsorption equilibration. A representative plot is shown in Figure 4.2.2 and Table 4.2.2 summarizes the relevant data. Figure S4.4.4 also shows the results for PhP.

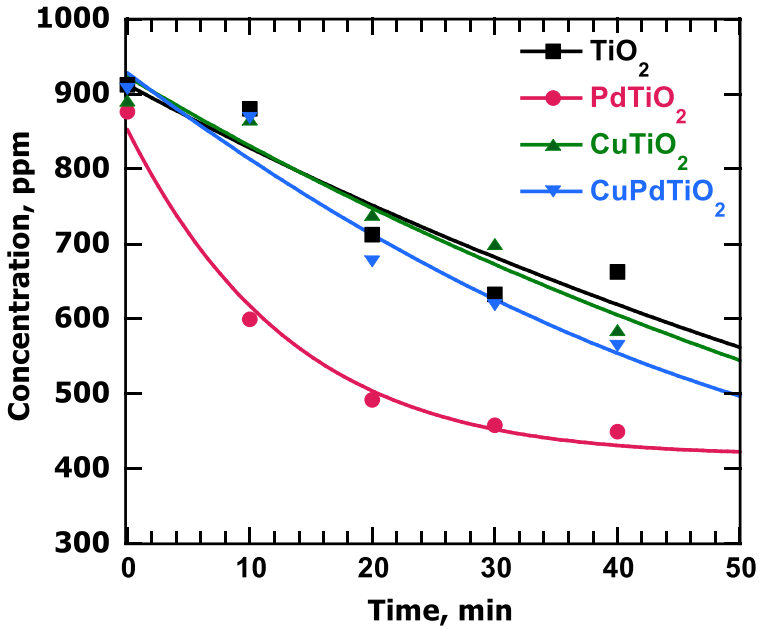

Figure 4.2.2. Adsorption experiments of PhA using the synthesized catalysts. Conditions: 10 mg Catalyst; 1 mL of 900 ppm alkyne solution in Ethanol; Stirring times: 0 min, 10 min, 20 min, 30 min, 40 min. Aliquots were taken every certain time and filtered before using GC-MS to monitor the area under the peak of PhA (3.70 min retention time identified by Gas Chromatography GC, Figure S4.4.2. Figure S4.4.3 shows the mass spectra of the alkynes) at different times. Calibration curves for every alkyne were necessary to determine the concentration of the alkyne at the mentioned times using 3,5-Di-tert-butyltoluene as an external standard.

Examination of Table 4.2.2 shows that the metals play a key role in enhancing the adsorption properties of the TiO_2-supported systems. Note for example that in the case of PhP, 2% palladium content is enough to triple the amount of alkyne adsorbed when compared with TiO_2 itself. This data shows that there is a significant number of sites over the Pd catalyst which strongly adsorb the alkyne molecules. On the other hand, the effect

of copper is also clear, but not as large as that of palladium. Additionally, the bimetallic catalyst exhibits similar adsorption to the one shown by Cu@TiO_2 even if the alkyne is internal. Also important, when preparing samples for catalysis studies, one must wait at least 30 minutes to ensure that the adsorption equilibrium has been reached. Unfortunately, this information is rarely included in literature reports, but it is essential to understand different types of reactions, like semi-hydrogenation ones.

Table 4.2.2. Adsorption capacity of the catalysts when being in contact with PhA and PhP after 40 min of stirring.

Material	**Phenylacetylene (PhA)**	**1-phenyl-1-propyne (PhP)**
TiO_2	27%	13%
Pd@TiO_2 (2% Pd)	49%	37%
Cu@TiO_2 (0.9% Cu)	34%	19%
CuPd@TiO_2 (0.8% Cu & 0.05% Pd)	37%	20%

Semihydrogenation of alkynes with single-metal TiO_2 catalysts

Scheme 4.2.2 shows the alkynes examined in this work. Among these, PhA and PhP were examined in more detail.

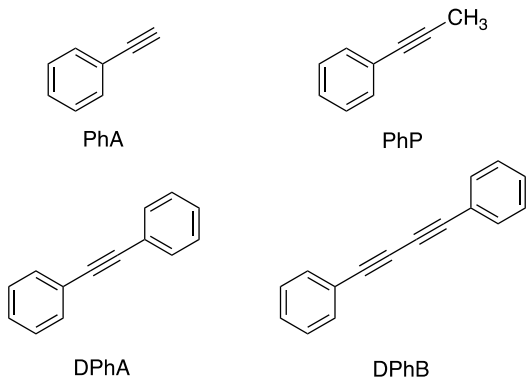

Scheme 4.2.2. Alkynes studied in this research.

All our studies involved irradiation with an LED UVA source centered at 370 nm (FWHM ~30 nm) with adjustable irradiance (Figure S4.4.5). Under typical exposure conditions (4 cm from the emitter), the irradiance at 100% power was ~320 W/m^2, although when using Pd@TiO$_2$ most studies were performed at 25% power (~87 W/m^2) (Figure S4.4.6). Figure 4.2.3 shows the conversion against time for the 4 alkynes at 6 mM studied when the catalyst was Pd@TiO$_2$ and the hydrogen donor was EtOH.

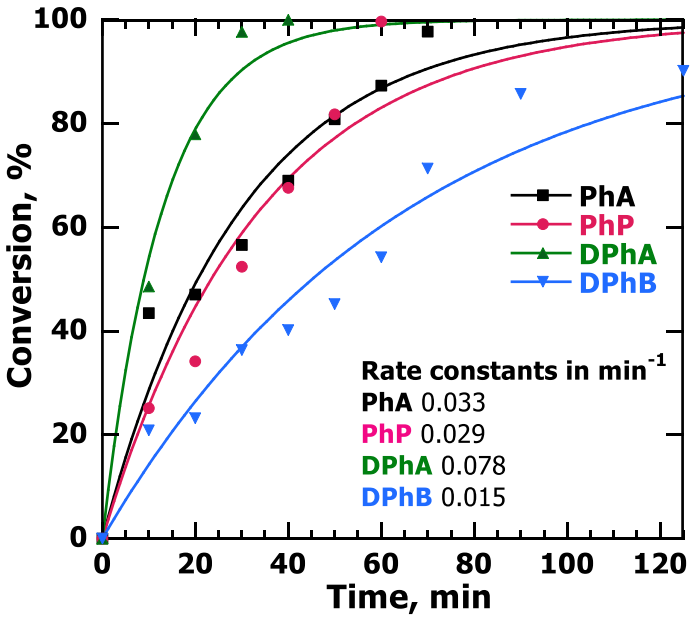

Figure 4.2.3. Conversion of alkynes after performing hydrogenation reactions using alkyne solutions in EtOH at a concentration of 6 mM, under argon and irradiated with UVA

light at 25% power and with 10 mg Pd@TiO_2 suspended in 8 mL. Under these conditions, the order of relative consumption rates changes, with DPhA showing the fastest consumption while DPhB is the slowest one. Note that before these experiments, semi-hydrogenation reactions using 900 ppm as the main concentration for the alkynes were also performed. In this case, the molar concentrations were not the same for all alkynes (Figure S4.4.7), but rather the mass concentration was matched.

It is interesting to examine the performance of the alkynes with Pd@TiO_2 and EtOH as a solvent, as a function of time. This is illustrated for PhP in Figure 4.2.4. The reaction is quite fast, reaching completion in under 80 minutes and a maximum yield of predominantly *cis* alkene at about 60 minutes when the remaining PhP is 4% and the selectivity towards alkenes is more than 90%, with about ~10% of 1-phenylpropane already formed at this point. Concerning the isomers formed in these reactions, in Figure S4.4.8, there is evidence that traces of the *trans*-isomer (retention time of 5.22 min in the GC chromatogram) are also formed, but the major product is the *cis*-compound (retention time of 4.90 min). Mechanistically, the reaction involves strong coordination between H (from the H source, in this case, the solvent) with Pd atoms in crystal lattices, thus the population of Pd sites had been proposed to govern the hydrogenation events on the metal surface.[21]

Continuing with the analysis of Figure 4.2.4, it is worth highlighting that at times slightly longer than that required for alkyne consumption the selectivity is reduced to 70% at 70 minutes and an additional 20 minutes reduces it to less than 20% (see '%Sel int' in Figure 4.2.4). This brings in the concept of *critical timing* where in this case it is not possible to achieve reasonable selectivity given that the reaction is very fast and thus stopping it at a very precise time might be difficult when working with Pd@TiO_2. It is possible to use Palladium catalysts for semi-hydrogenation, but the time at which the reaction must be stopped requires critical timing and an error of just a few minutes induces extensive over-hydrogenation to the alkane product.

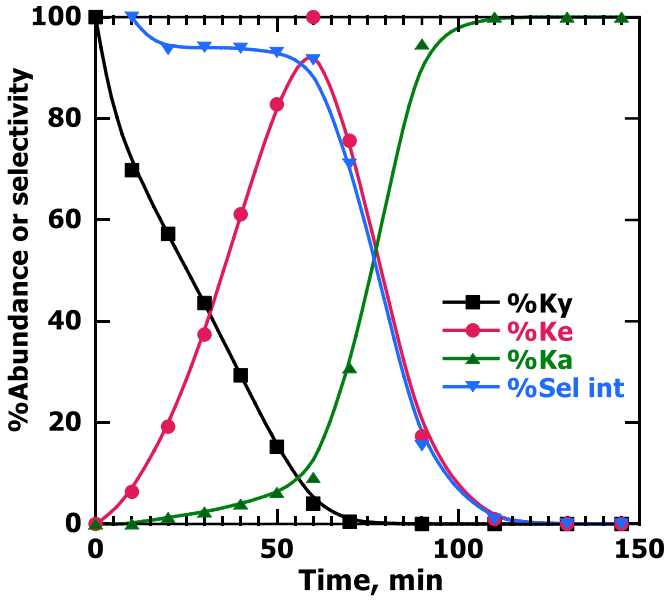

Figure 4.2.4. Abundance of the PhP (%Ky), along with alkenes (%Ke) and alkane (%Ka) and selectivity towards the alkenes (%Sel int) vs. time for 8 mL of a 6 mM solution in EtOH of PhP stirred with 10 mg of Pd@TiO_2. The reaction was performed in a Pyrex test tube with a rubber cap and irradiated with 25% UVA power under Ar. At 60 minutes the abundance of the alkyne is more than 95% and the selectivity towards alkenes is 91%. Only 10 minutes longer makes the selectivity 70% at 70 minutes.

The problem of critical timing occurs in spite of the fact that alkenes show less affinity for adsorption on the Pd@TiO_2 catalyst than alkynes. To prove this hypothesis, we tested the adsorption of DPhA vs. *cis* and *trans*-stilbene on Pd@TiO_2. Figure 4.2.5 shows these results obtained after stirring for 40 minutes 1 mL of a 900 ppm solution for DPhA with 10 mg of Pd@TiO_2. 41% of adsorption is achieved since at 40 min the concentration of the alkyne was reduced from 900 ppm to 520 ppm. Moreover, for the *cis* and *trans* isomers of stilbene, after 40 min, the adsorption on the surface catalyst is only 5% and 9%, respectively. Consequently, the adsorption of the alkyne on the catalyst surface is more efficient compared with the alkenes. For the semi-hydrogenation of alkynes, the literature suggests that alkynes adsorb more selectively on a metal surface, retarding alkene adsorption and hindering its hydrogenation to an alkane, as long as alkynes are still present

in the reaction mixture;[22] these results might help to understand the semi-hydrogenation process.

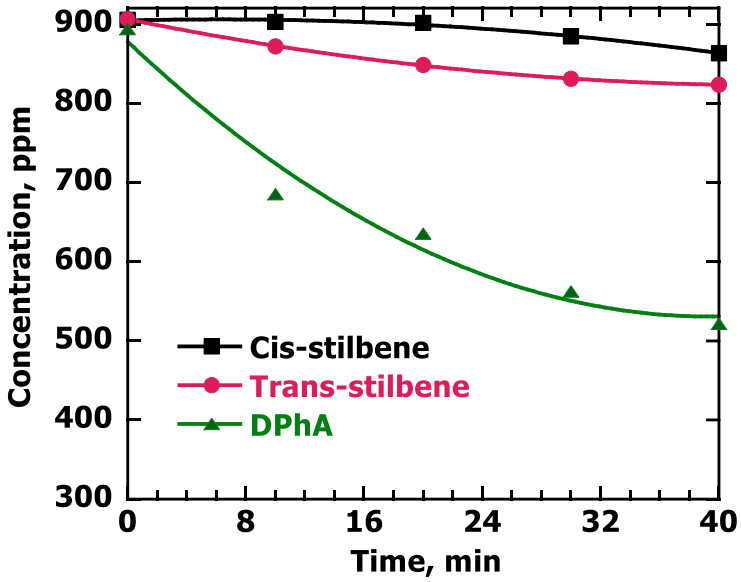

Figure 4.2.5. Adsorption of DPhA, cis and trans-stilbene on Pd@TiO_2. Solutions of the compounds in EtOH (900 ppm) and 10 mg of Pd@TiO_2 were stirred for 0, 10, 20, 30 and 40 min. Aliquots of the solution were taken at these times and filtered before analyzing them by GC-MS. The chromatograms provided by GC-MS were analyzed using calibration curves to determine the concentration of the compounds, where 3,5-di-tert-butyltoluene was used as an external standard.

The issue of critical timing illustrated in Figure 4.2.4 for PhP is not unique and similar problems are found for the other alkynes studied in this work (Figure S4.4.9) and summarized in Table 4.2.3. The loss of selectivity is rapid and large which makes stopping the reaction at a critical time essential. Even 15 minutes will make the loss of selectivity quite large. For PhP, illustrated in Figure 4.2.4, a difference of 15 minutes with respect to t_{95}, will reduce the selectivity to 59%, while stopping 15 minutes too soon will reduce the conversion and yield to 78%.

Table 4.2.3. Conversion and selectivity for the alkynes in Chart 1 over time for 8 mL of 6 mM solutions in EtOH stirred with 10 mg of Pd@TiO_2 in Pyrex tubes and irradiated with 25% UVA power under Ar.

Item ↓ / Molecule →	**PhA**	**PhP**	**DPhA**	**DPhB**
Time for 95% conversion, t95	67 min	60 min	28 min	114 min
Selectivity at 95% conversion	95%	88%	79%	48%
Selectivity at 1.5 x t_{95}	52%	19%	11%	<1%
Selectivity at 2 x t_{95}	23%	<0.5%	<0.2%	~0

We have also examined the effect of catalyst loading, illustrated in Figure S4.4.10 for PhP. We note that a reduction by five in the catalyst loading (2 mg rather than 10 mg of Pd@TiO_2) only reduces the rate of consumption by a factor of two. However, the issue of critical timing discussed in relation to Figure 4.2.4 and Table 4.2.3, remains unchanged. In general, small deviations from the critical time can cause large reductions in selectivity. Further, stopping early is not a solution either because the conversion curve is very steep and early stops lead to reduced conversion and yields.

The situation with Cu@TiO_2 as a catalyst was very different from that with Pd@TiO_2. The paragraphs and figures that follow elaborate on these differences. In brief, the copper catalyst is slower than palladium, but in terms of critical timing it is very forgiving, and over-hydrogenation is not a problem. In the qualitative context of Figure S4.4.1, one would estimate that $k_2 < 0.001\ k_1$. Initial experiments in this section were performed with 6 mM PhP and PhA in EtOH using 100% lamp power since when using 25%, the reaction can take days. Figure 4.2.6 shows the time evolution of the reaction over an extended period of time and with 100% lamp power. Even doubling the time required for 100% conversion, the yield of alkanes is minimal.

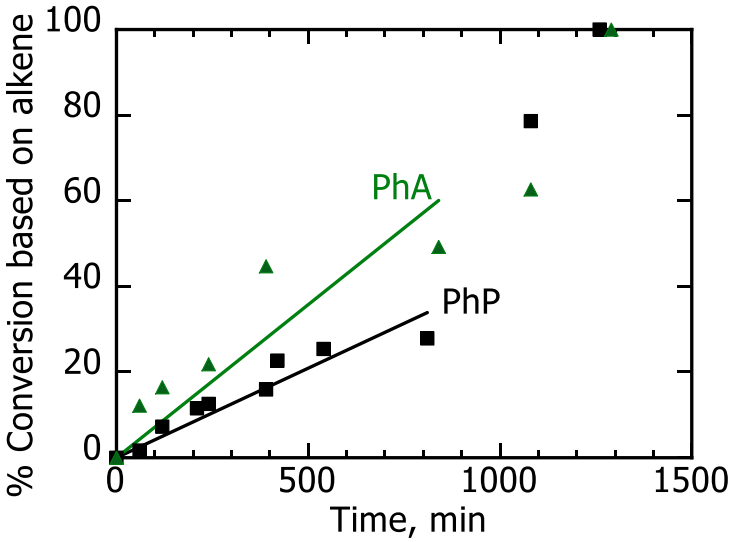

Figure 4.2.6. Conversion vs time for PhA (green) and PhP (black). The samples consisted of 8 mL of 6 mM solutions in EtOH of the alkynes stirred with 10 mg of Cu@TiO_2 in different Pyrex tubes and irradiated with 25% UVA power under Ar. The fitting corresponds to low conversion (<50%) data and show that PhA is 70% faster than PhP. The cis-alkene was essentially the only product with selectivities exceeding 98% for the first 1000 minutes.

For Cu@TiO_2 in EtOH there is no formation of 1-phenylpropane even at longer times in comparison with the results obtained with Pd@TiO_2 (compare with Table 4.2.3). Copper shows a major improvement in the selectivity of the alkynes even if the reaction is extended for 20 h. Accordingly, over-hydrogenation is not a problem, yet, the reaction time is around 10 times longer than that for Pd@TiO_2. Thus, the issue of longer reaction rates needs improvement.

In an attempt to improve the kinetics, we tried using a different solvent that may help maintain the selectivity towards the alkenes and reduce reaction times.[23] According to this, MeOH was used as the hydrogen donor/solvent given its promising results in catalytic hydrogenation reactions. Hence, keeping the same conditions of the semi-hydrogenation reactions, Figure 4.2.7 shows the time profiles for PhP and PhA when performing the semi-hydrogenation reactions in EtOH and MeOH.

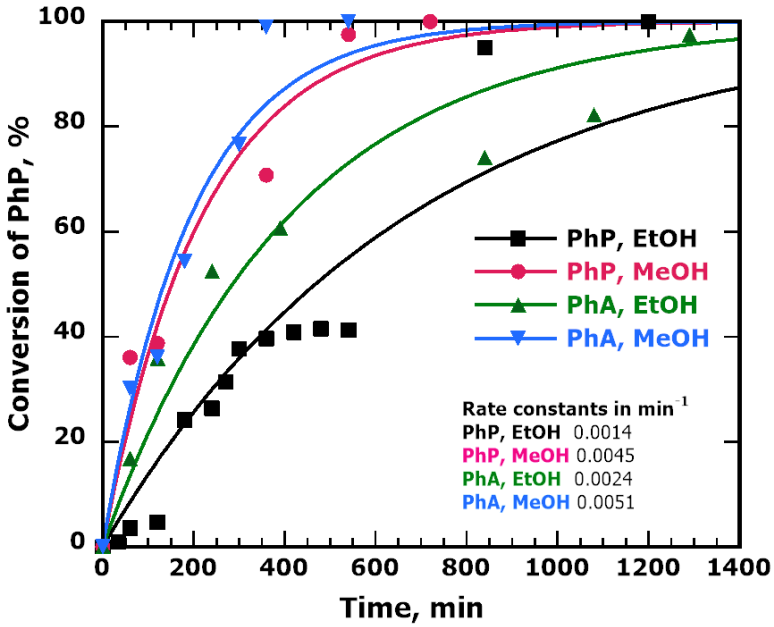

Figure 4.2.7. Conversion of PhA and PhP in MeOH and EtOH vs. time. 8 mL of 6 mM solutions in MeOH and EtOH of the alkynes were stirred with 10 mg of Cu@TiO_2 in different Pyrex® containers and irradiated with 100% UVA power under Ar. The data were fit with an exponential forced fit to start at zero and levelling of at 100%; the curves are mostly presented to help the reader visualize data trends.

The results of Figure 4.2.7 show that MeOH, as both the hydrogen donor and solvent, increases the rates of reaction. These results show that the rate of alkyne-to-alkene reaction when using Cu@TiO_2 and MeOH, can be improved while avoiding over-hydrogenation to the saturated alkane moiety. Control experiments have also been performed and Figure S4.4.12 shows the results for the reaction of PhP in MeOH with TiO_2 itself where after 540 min (9h) of reaction less than 5% of PhP was consumed and barely around ~1% of *cis*-1-phenyl-1-propene is produced. This confirms that decorating TiO_2 with a metal improves the photocatalytic activity of the material for these reactions as the previous results have shown.

Semi-hydrogenation of alkynes with the bimetallic CuPd@TiO_2 catalyst

The motivation to test a bimetallic catalyst relates to the excellent selectivity of Cu@TiO_2 and the excellent kinetics of Pd@TiO_2. Based on previous results, we wondered if light-initiated incorporation of palladium to the Cu@TiO_2 catalyst may help with the kinetics without significant loss of selectivity, and without creating an important critical timing issue. With this in mind, we prepared CuPd@TiO_2 by galvanic replacement, with a loading of 0.8% copper and 0.05% palladium. The catalyst was tested in MeOH suspension with solutions of 6 mM PhP in MeOH and two different catalyst loadings, 10 mg and 5.4 mg, which are shown in Figure S4.4.11. The choice of MeOH reflects the observation of improved kinetics shown in Figure 4.2.7. In order to compare the different catalysts, we selected 6 mM of PhP and 10 mg of the catalyst under the conditions specified in the caption of Figure 4.2.8. Please note that the CuPd@TiO_2 catalyst was prepared from a sample of the same Cu@TiO_2 material used in the experiment.

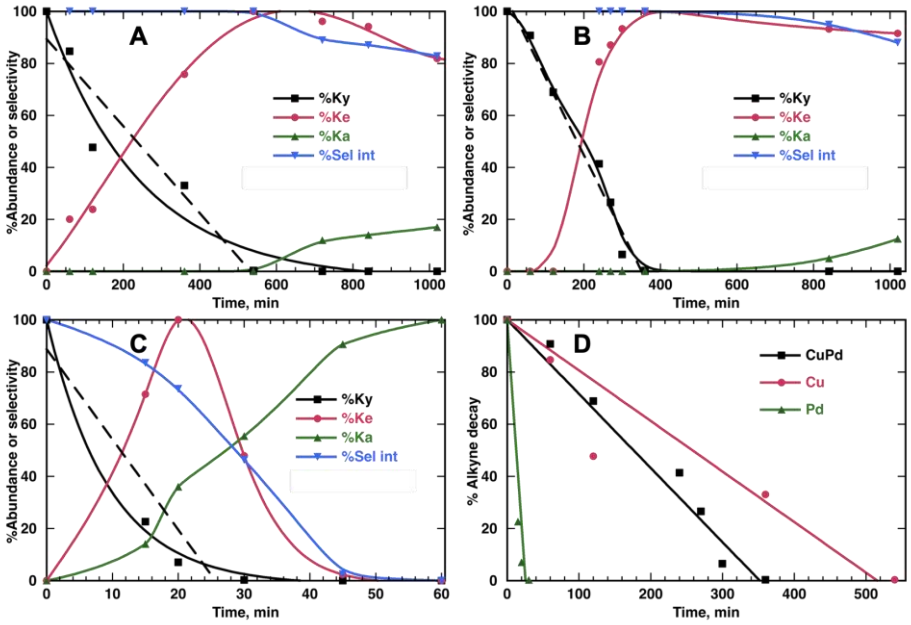

Figure 4.2.8. (A) Comparison of catalytic performance for 8 mL of 6 mM PhP solution in MeOH stirred with 10 mg of catalyst and irradiated with 25% UVA power under Ar, for Cu@TiO_2; **(B)** CuPd@TiO_2; **(C)** Pd@TiO_2. Panel D compares the different consumption

slopes (100% to 5%) for the alkyne with the different catalysts. The kinetic data are also summarized in Table 4.2.4.

Table 4.2. 4. Comparison of catalyst performance under the conditions of Figure 4.2.8.

Catalyst	Alkyne rate of consumption (min^{-1})	Selectivity at 95% alkyne conversion	Selectivity at twice the time for 95% conversion
$Cu@TiO_2$	0.19	>99%	84%
$CuPd@TiO_2$	0.29	>99%	97%
$Pd@TiO_2$	3.94	88%	<1%

Table 4.2.4 shows that incorporating traces of Pd (see Table 4.2.1) is enough to increase the rate by 52% with respect to $Cu@TiO_2$, and even it still remains much slower than $Pd@TiO_2$. The observed performance of the bimetallic $CuPd@TiO_2$ catalyst improves over previously reported catalysts, including the Lindlar Pd catalyst and other systems where, for example, the addition of organic ligands is needed to avoid over-hydrogenation of alkenes to alkane.[24,25] In this line of thought and in agreement with previous reports based on Pd bimetallic catalysts,[26, 27] the possible absence of substantial Pd agglomeration result in weak adsorption toward alkene on the catalyst surface and high alkene selectivity. It is also remarkable that Panel B in Figure 4.2.8 shows better long-term selectivity than Panel A. Surprisingly a small amount of Pd not only increases the rate of reaction but causes a selectivity improvement. Additionally, it is worth highlighting that the light source is essential for photocatalytic reactions like these ones. According to the results of Figure S4.4.13, when the reaction for PhP and 10 mg of $CuPd@TiO_2$ is performed without light, for at least 9h, there is no consumption of the alkyne nor production of the alkenes. The above also indicates that photothermal effects do not contribute to the reaction.

The mechanism by which palladium improves reactivity without a decrease in selectivity is probably similar to that for palladium on gold, where it is believed that hydrogen atoms generated on Pd leak into the second metal where the reaction takes place.[28] In this case, H-atoms from the solvent, either EtOH or MeOH, generated on Pd

would be transferred to copper that controls the selectivity of the reaction as it is depicted in Figure 4.2.9.

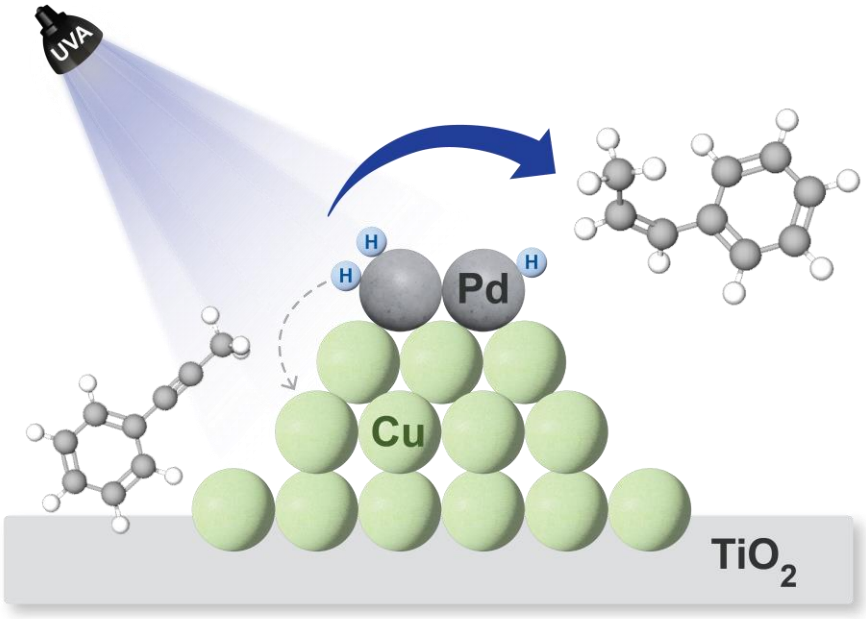

Figure 4.2.9. Plausible scenario to understand the activity shown by CuPd@TiO_2. Figure inspired by similar concepts in the literature.[28] Hydrogen atoms generated from MeOH (solvent) on Pd surface are transferred to Cu. This hydrogen transfer controls the reaction's selectivity, allowing for the formation of *cis*-alkenes.

Therefore, introducing Pd, which can rapidly speed up the reaction, on Cu/TiO_2 catalyst, which has been shown to be much more chemoselective, helps to improve the selectivity towards alkenes in this photocatalytic reaction and the critical timing control is forgiving when reaction times are measured in hours or overnight.

Materials and Methods

Materials

Chemicals and materials were sourced from multiple suppliers for the experimental work. The initiator Irgacure-2959 was a gift from BASF, while the alkynes, solvents

(spectrophotometric grade > 99.8%), $PdCl_2$, $CuCl_2 \cdot 2H_2O$ and $Pd(acac)_2$ were purchased from Sigma Aldrich. TiO_2 P25 was purchased from Univar Canada. The MilliQ water was obtained by purification of deionized water using a Thermo Scientific™ Barnstead™ GenPure™ water purification system (conductivity 18 MΩ/cm).

Instruments

The photocatalytic performance of the catalysts at the bench scale was examined in Pyrex® test tubes. The reaction mixture was stirred and irradiated by an UVA Kessil lamp PR160-370 nm controllable LED at different powers (25% and 100%). The synthesis of the catalysts was performed by using a Luzchem photoreactor equipped with 14 UVA bulbs. Transmission Electron Microscope (TEM) images were acquired at the University of Ottawa's Materials Characterization Facility (MatChar) with a JEM2100F FETEM (JEOL) field emission transmission electron microscope. Particle sizes were determined with ImageJ analysis. Scanning electron microscopy (SEM) and Energy-dispersive X-ray spectroscopy (EDS) images were acquired at the NanoFab Facility at the University of Ottawa with a Zeiss GeminiSEM 500 column using a Schottky thermal field emitter filament for imaging between 0.1 and 30 kV for sub-nanometer resolution imaging and with a Bruker EDS detector suitable for X-ray detection for spot identification of the composite. The metal loading of catalysts was determined by Inductively Coupled Plasma Emission Spectrometry (ICP-OES), using an Agilent Vista Pro ICP Emission Spectrometer. Characterization of the semi-hydrogenation reactions and its products was performed by using a mass spectrometry in an Agilent 6890-N Gas Chromatograph with an Agilent 5973 mass selective detector.

Semi-hydrogenation Reactions

The reactions were performed in 15 mL Pyrex® test tubes with a rubber cap. In a typical reaction, 8 mL of 900 ppm or 6 mM alkyne solutions in EtOH stirred with 10 mg of catalyst ($Pd@TiO_2$, $Cu@TiO_2$) and irradiated with 25% or 100% UVA light source at 4 cm from the test tube. The reaction mixture was purged with argon. Similar preparations were also made using methanol as the solvent and using either the mentioned catalysts or $CuPd@TiO_2$. Aliquots were taken at regular intervals and filtered using syringe filters with

a PTFE membrane in order to remove the catalyst before using an Agilent 6890-N Gas Chromatograph with an Agilent 5973 mass selective detector to monitor the reactions and identify the peaks of the reactants and products. Every time the aliquots were taken, purging the reaction with Ar was necessary in order to assure the inert environment. Calibration curves for every alkyne were necessary to determine the concentration of the alkyne at the mentioned times using 3,5-di-tert-butyltoluene as an external standard.

Conclusions

Semi-hydrogenations always present significant challenges as the interplay of kinetics and selectivity determine the performance of the catalyst. The reality of the organic laboratory is that reactions are not stopped at exact times and reaction end points are frequently controlled by convenience, such as the case of "overnight reactions". Reactions that can lose their yield or selectivity over short periods of time are simply impractical. Such is the case of Pd@TiO_2 as a catalyst, where critical timing is essential to preserve high yields and selectivity. In contrast, Cu@TiO_2 and CuPd@TiO_2 offer excellent selectivity without critical timing requirements. The latter is about 52% faster than Cu@TiO_2 and to our surprise, not only preserves the selectivity, but also offers a small improvement (Compare Figure 9. Panels A and B). Thus, for alkyne semi-hydrogenation we recommend CuPd@TiO_2 as a catalyst and methanol as the solvent. These results open the way to synthesize highly active and selective catalysts inspired by the reality of timing control of semi-hydrogenation processes at bench scale. However, future work should focus on further exploration to optimize even more the time of the reaction to complete the semi-hydrogenation process in less time but without losing great selectivity and still have control over the critical point between passing from an alkene molecule to an alkane.

Supplementary Materials: The following supporting information can be downloaded at: https://www.mdpi.com/article/10.3390/nano13172390/s1: Figures S4.4.1–S4.4.13: showing GC-MS characterization, results for adsorption experiments of PhP at 900 ppm, spectral irradiance of the UVA source employed in the semi-hydrogenation reactions under

different conditions, TEM images and the corresponding size histogram SEM/EDS analysis, conversion of alkynes and selectivity towards alkenes at different conditions.

Author Contributions: The concept for this research was proposed by JCS. All the experimental work was performed by MCP with help from BW who performed and interpreted ICP studies. The preparation of the manuscript and interpretation of the results was a joint effort between the authors. All authors have read and agreed to the published version of the manuscript.

Funding: This research was funded by the Natural Sciences and Engineering Research Council of Canada, the Canada Foundation for Innovation, the Canada Research Chairs Program.

Data Availability Statement: Original data are available from the corresponding author upon reasonable request.

Acknowledgments: The undergraduate student Rhiannon Hendley helped initially in the adsorption experiments of the alkynes on Pd@TiO_2.

Conflicts of Interest: The authors declare no conflict of interest.

4.3. References

1. H. Zea, K. Lester, A. K. Datye, E. Rightor, R. Gulotty, W. Waterman and M. Smith, *Applied Catalysis A General*, 2005, **282**, 237–245.
2. S. A. Nikolaev, L. N. Zanaveskin, V. V Smirnov, V. A. Averyanov and K. L. Zanaveskin, *Russian Chemical Reviews*, 2009, **78**, 231–247.
3. A. Borodziński and G. C. Bond, *Catalysis Reviews Science and Engineering*, 2008, **50**, 379–469.
4. S. Domínguez-Domínguez, Á. Berenguer-Murcia, D. Cazorla-Amorós and Á. Linares-Solano, *Journal of Catalysis*, 2006, **243**, 74–81.
5. S. Domínguez-Domínguez, Á. Berenguer-Murcia, B. K. Pradhan, Á. Linares-Solano and D. Cazorla-Amorós, *Journal of Physical Chemistry C*, 2008, **112**, 3827–3834.

6. R. V Chaudharl, R. Jaganathan, D. S. Kolhe, G. Emlg and H. Hofmann, *Industrial and Engineering Chemistry product Research and Development*, 1986, **25**, 375–379.

7. S. Song, K. Li, J. Pan, F. Wang, J. Li, J. Feng, S. Yao, X. Ge, X. Wang and H. Zhang, *Advanced Materials*, 2017, **29**, 1–6.

8. J. Ballesteros-Soberanas, J. C. Hernández-Garrido, J. P. Cerón-Carrasco and A. Leyva-Pérez, *Journal of Catalysis*, 2022, **408**, 43–55.

9. M. Wang, L. Liang, X. Liu, Q. Sun, M. Guo, S. Bai and Y. Xu, *Journal of Catalysis*, 2023, **418**, 247–255.

10. Y. Zheng, L. Gu, Y. Li, J. Ftouni and A. Dutta Chowdhury, *Catalysts*, 2022, **13**, 50.

11. J. Lv, D. Wang, X. Guo, W. Ding and W. Yang, *Catalysis Communications*, 2023, **181**, 106715.

12. R. Huang, J. Wu, M. Zhang, B. Liu, Z. Zheng and D. Luo, *Materials & Design*, 2021, **210**, 110040.

13. H. Kominami, M. Higa, T. Nojima, T. Ito, K. Nakanishi, K. Hashimoto and K. Imamura, *ChemCatChem*, 2016, **8**, 2019–2022.

14. S. Imai, K. Nakanishi, A. Tanaka and H. Kominami, *ChemCatChem*, 2020, **12**, 1609–1616.

15. X. Zhao, L. Zhou, W. Zhang, C. Hu, L. Dai, L. Ren, B. Wu, G. Fu and N. Zheng, *Chem*, 2018, **4**, 1080–1091.

16. A. Hainer, N. Marina, S. Rincon, P. Costa, A. E. Lanterna and J. C. Scaiano, *Journal of the American Chemical Society*, 2019, **141**, 4531–4535.

17. A. Elhage, A. E. Lanterna and J. C. Scaiano, *ACS Catalysis*, 2017, **7**, 250–255.

18. A. Elhage, A. E. Lanterna and J. C. Scaiano, *Chemical Science*, 2019, **10**, 1419–1425.

19. B. Wang, A. E. Lanterna and J. C. Scaiano, *ACS Catalysis*, 2021, **11**, 4230–4238.

20. B. Wang, J. Durantini, J. Nie, A. E. Lanterna and J. C. Scaiano, *Journal of the American Chemical Society*, 2016, **138**, 13127–13130.

21. Q. Fan, S. He, L. Hao, X. Liu, Y. Zhu, S. Xu and F. Zhang, *Scientific Reports*, 2017, **7**, 42172.

22. S. A. Nikolaev and V. V. Smirnov, *Catalysis Today*, 2009, 147, S336–S341.

23. J. Sklyaruk, V. Zubar, J. C. Borghs and M. Rueping, *Organic Letters*, 2020, **22**, 6067–6071.

24. S. G. Kwon, G. Krylova, A. Sumer, M. M. Schwartz, E. E. Bunel, C. L. Marshall, S. Chattopadhyay, B. Lee, J. Jellinek and E. V. Shevchenko, *Nano Letters*, 2012, **12**, 5382–5388.

25. D. Albani, M. Shahrokhi, Z. Chen, S. Mitchell, R. Hauert, N. López and J. Pérez-Ramírez, *Nature Communications*, ,2018, **9**, 2634.

26. G. X. Pei, X. Y. Liu, X. Yang, L. Zhang, A. Wang, L. Li, H. Wang, X. Wang and T. Zhang, *ACS Catalysis*, 2017, **7**, 1491–1500.

27. F. P. Da Silva, J. L. Fiorio, R. V. Gonçalves, E. Teixeira-Neto and L. M. Rossi, *Industrial & Engineering Chemistry Research*, 2018, **57**, 16209–16216.

28. P. Serna, P. Concepción and A. Corma, *Journal of Catalysis*, 2009, **265**, 19–25.

4.4. Post-print Version of Supporting Information

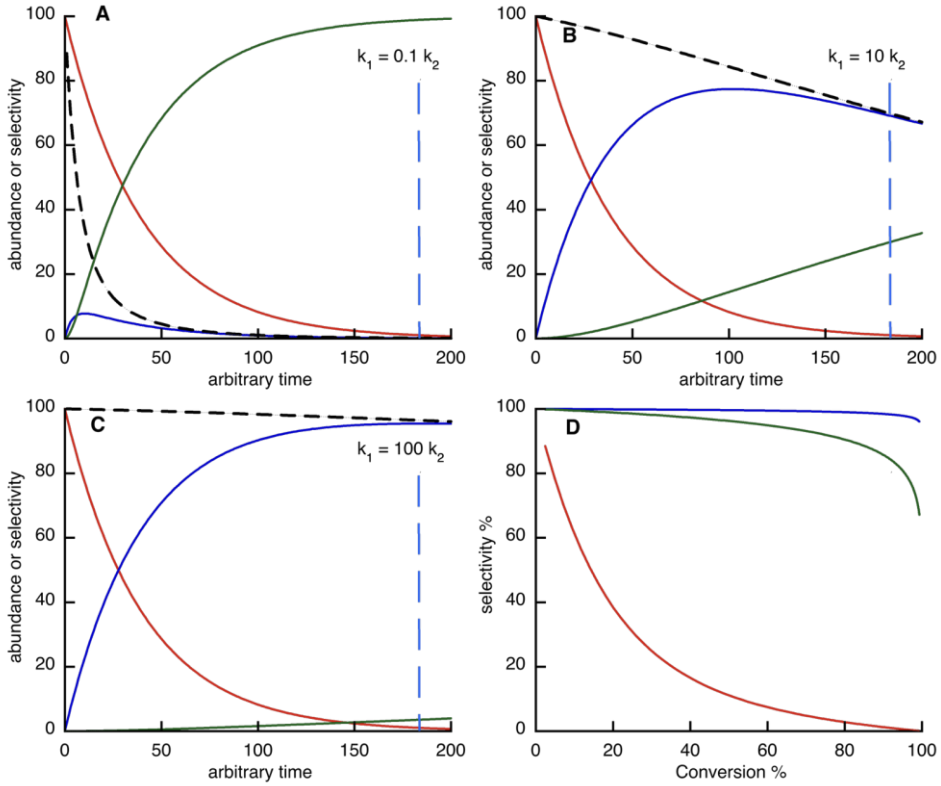

Figure S4.4.1. Illustrating the effect of the relative values of k_1 and k_2 on the selectivity of a reaction. For panels A, B and C: The vertical blue dashed line corresponds to 99% conversion. Red line for alkyne, blue for alkene, green for alkane and black dash for % alkene selectivity. Panel D shows the selectivities against percent conversion, in red for $k_1 = 0.1\ k_2$, in green for $k_1 = 10\ k_2$ and in blue for $k_1 = 100\ k_2$.

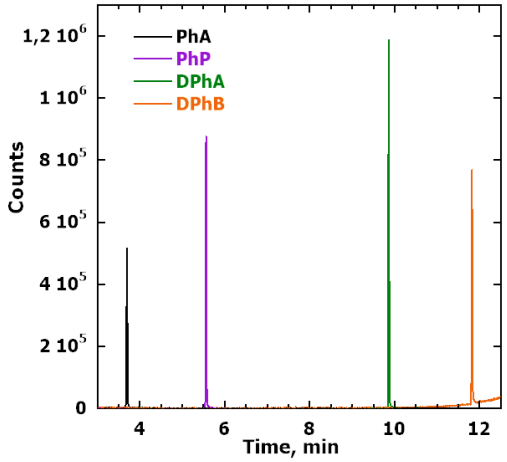

Figure S4.4.2. Chromatograms showing the peaks of the alkynes used in this research. The alkynes have the following retention times: PhP (5.56 min), PhA (3.70 min), DPhA (9.86 min), DPhB (11.82 min).

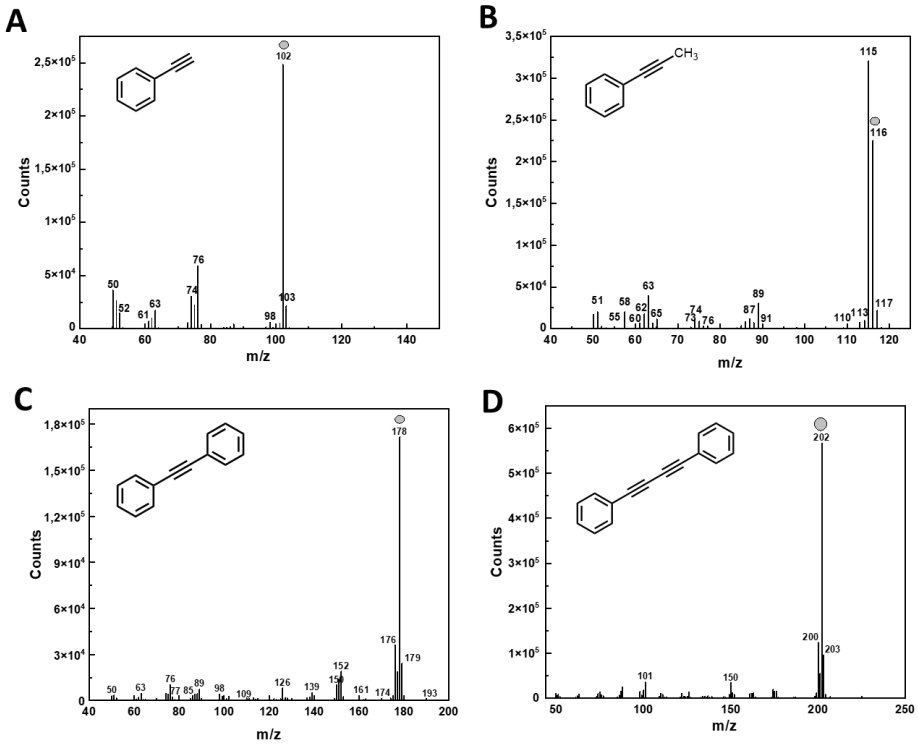

Figure S4.4.3. Mass spectra of the alkynes. Each spectrum shows (●) the molecular ion of the molecules.

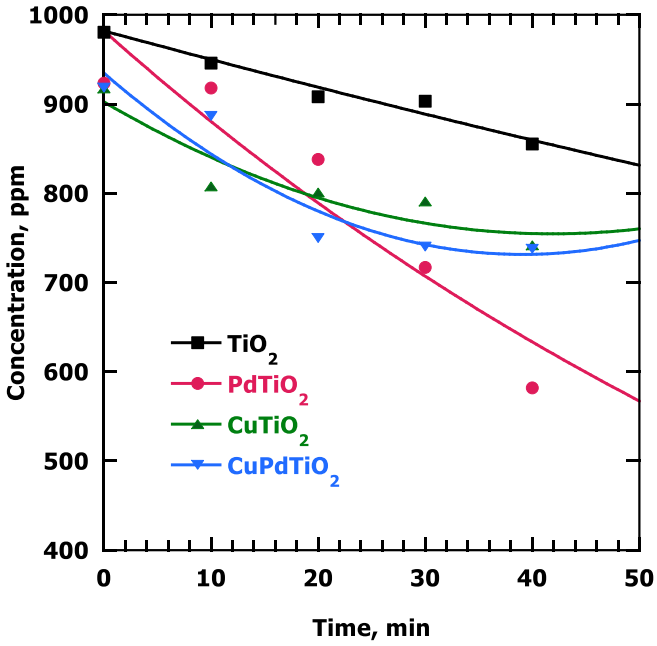

Figure S4.4.4. Adsorption experiments of PhP using the catalysts used. Conditions: 10 mg Catalyst; 1 mL of 900 ppm alkyne solution in EtOH; Stirring times: 0 min, 10 min, 20 min, 30 min, 40 min. Aliquots were taken at selected times and filtered before using GC-MS to monitor the areas of PhP (5.56 min retention time identified by GC, Figure S1) at different times. Calibration curves for every alkyne were necessary to determine the concentration of the alkyne at the mentioned times using 3,5-di-tert-butyltoluene as an external standard.

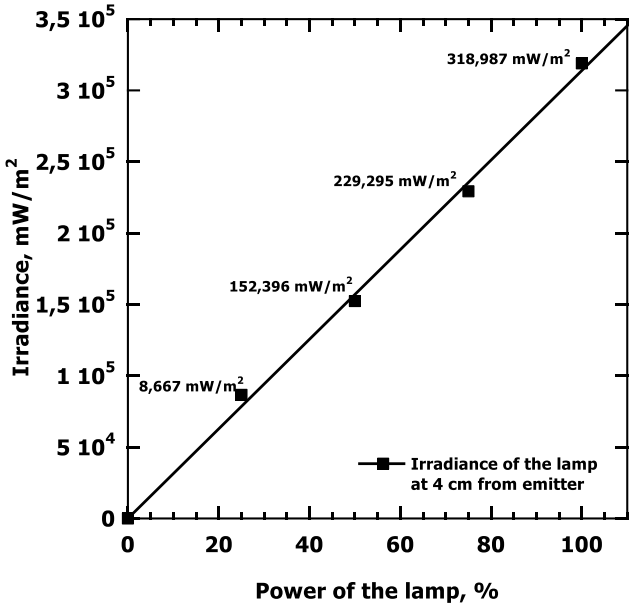

Figure S4.4. 5. Irradiance of LED UVA source at different power of the used lamp.

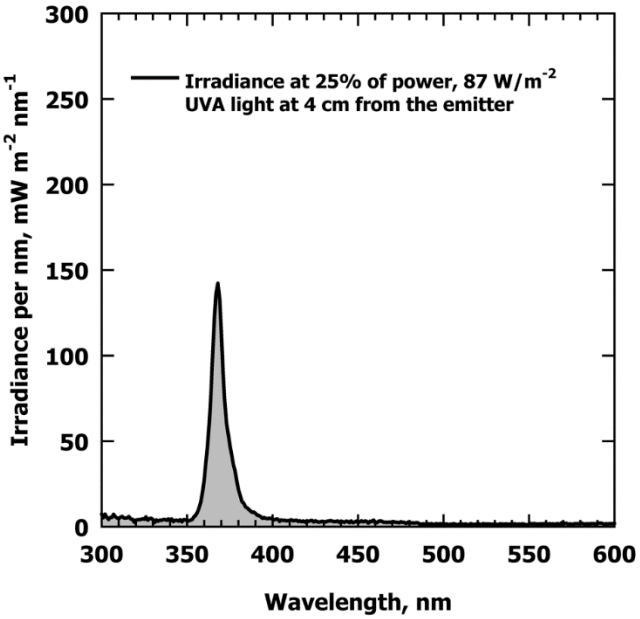

Figure S4.4. 6. Spectral Irradiance of UVA lamp used for semi-hydrogenation reactions; determined with a Luzchem spectroradiometer.

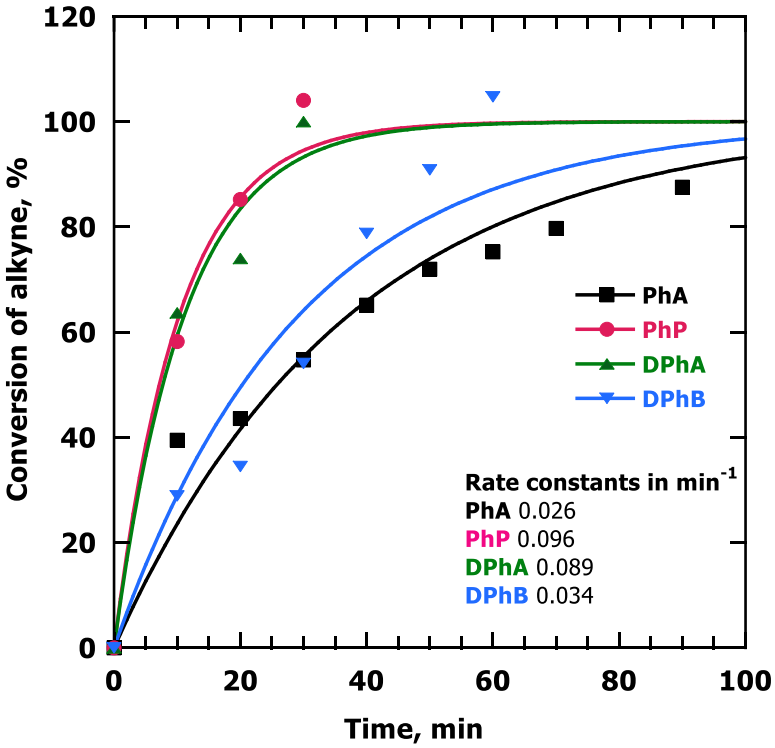

Figure S4.4.7. Conversion of alkynes after performing hydrogenation reactions using alkyne solutions in EtOH at a concentration of 900 ppm, under argon and irradiated with UVA light at 25% power and with 10 mg Pd@TiO_2 suspended in 8 mL. Under these conditions, the order of relative consumption rates changes, with PhA showing the slowest consumption along DPhB while PhP is the fastest one. Note that when working in ppm, the concentration for all the alkynes ranges from 5.0 to 8.8 mM.

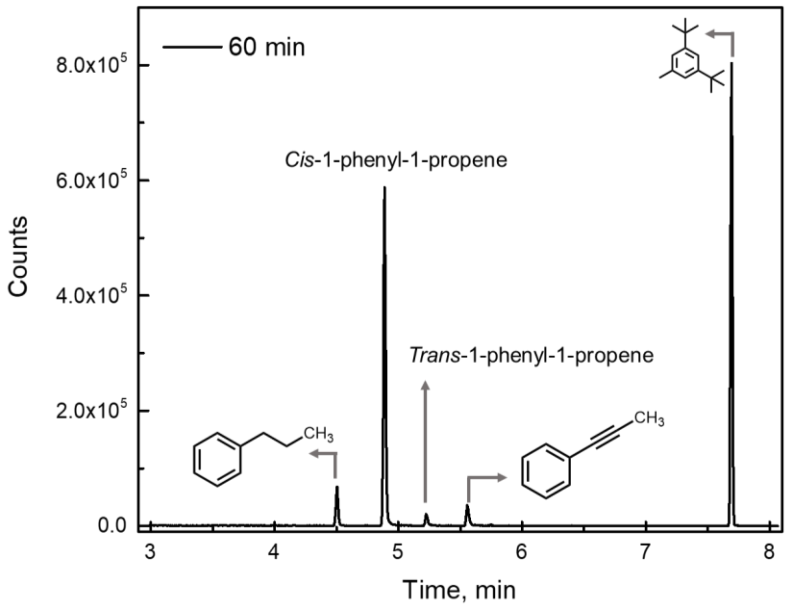

Figure S4.4.8. GC-chromatogram at 60 min of semi-hydrogenation reaction of PhP 6mM in EtOH using 10 mg of Pd@TiO_2 under Ar. At this point of time, 95% of the 1-phenyl-1-propyne (retention time of 5.56 min) has been consumed and *cis*-1-phenyl-1-propene (retention time of 4.90 min) is already formed. *Trans*-1-phenyl-1-propene (retention time of 5.22 min) is also formed but in trace amounts. For this chromatogram, a 0.1 mL aliquot of the reaction was taken. The solution was filtered to remove the catalyst and dissolved in 0.8 mL dichloromethane (DCM). Furthermore, 0.1 mL of a 2.4 mM solution of 3,5-Di-tert-butyltoluene (retention time of 7.7 min) was added to the vial as an external standard.

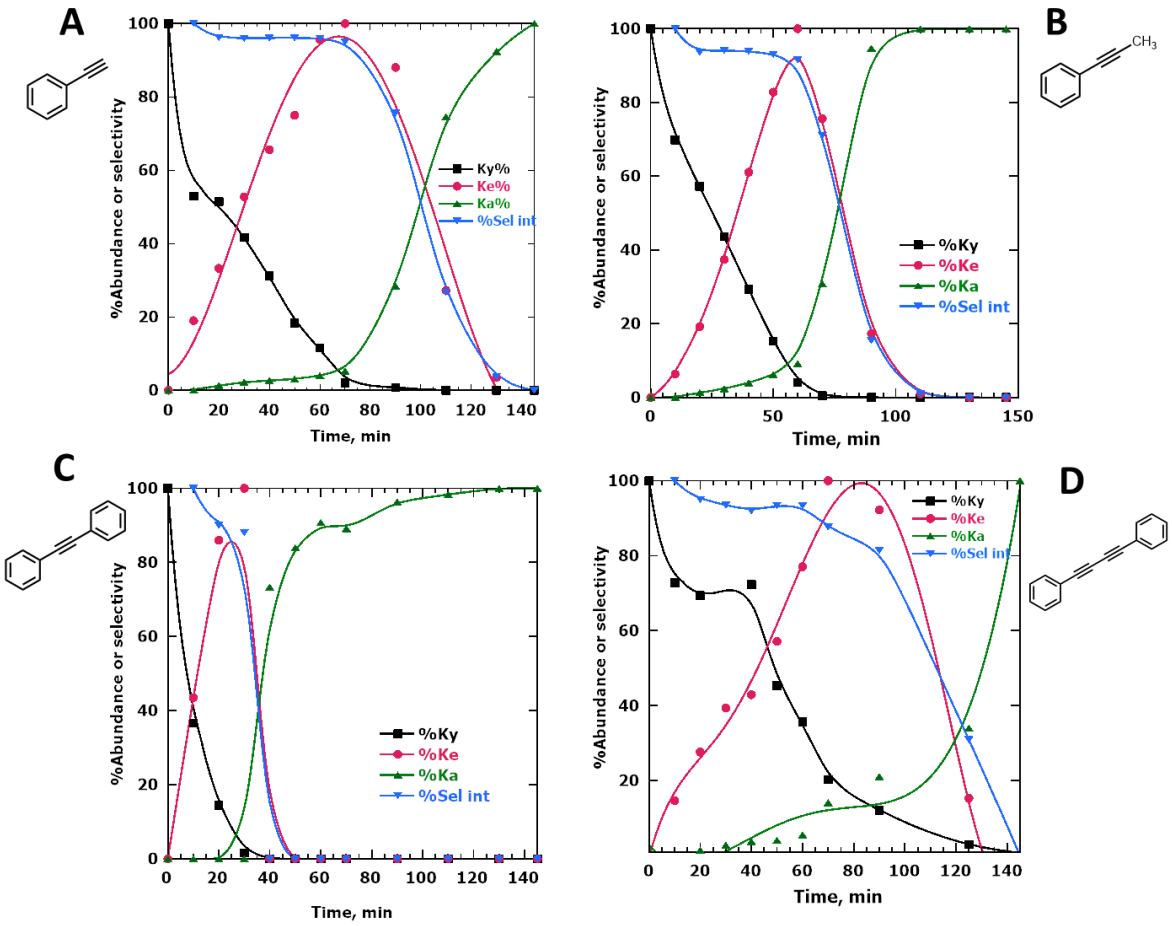

Figure S4.4.9. Abundance of the alkynes (%Ky), its respective alkenes (%Ke) and alkane (%Ka) or selectivity towards the alkenes (%Sel int) vs. time. 8 mL of 6 mM solutions of the alkynes in EtOH were stirred with 10 mg of Pd@TiO_2 in Pyrex tubes and irradiated with 25% UVA power under Ar. (A) PhA, (B) PhP, (C) DPhA, (D) DPhB.

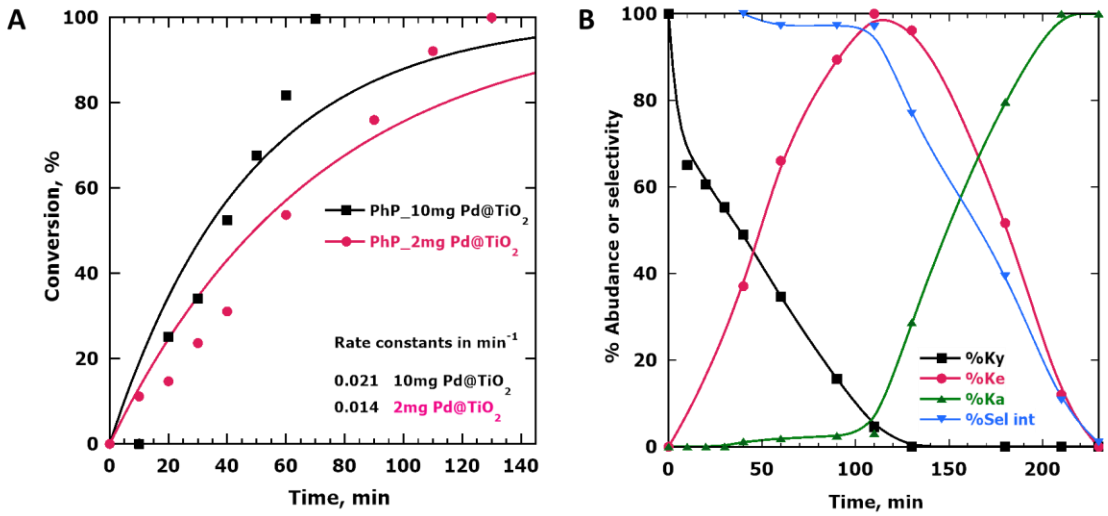

Figure S4.4.10. (A) Conversion of PhP after performing semi-hydrogenation reaction using a 6 mM alkyne solution in EtOH, under argon, irradiated with UVA light at 25% power, with 10 mg and 2 mg of Pd@TiO_2 suspended in 8 mL of solution; **(B)** Abundance of PhP (%Ky), its alkenes (%Ke) and alkane (%Ka) or selectivity of *cis*-1-phenyl-propyne (%Sel int) vs. time; 8 mL of a 6 mM solution in EtOH of PhP was stirred with 10 mg and 2mg of Pd@TiO_2 in different Pyrex® containers and irradiated with 25% UVA power under Ar.

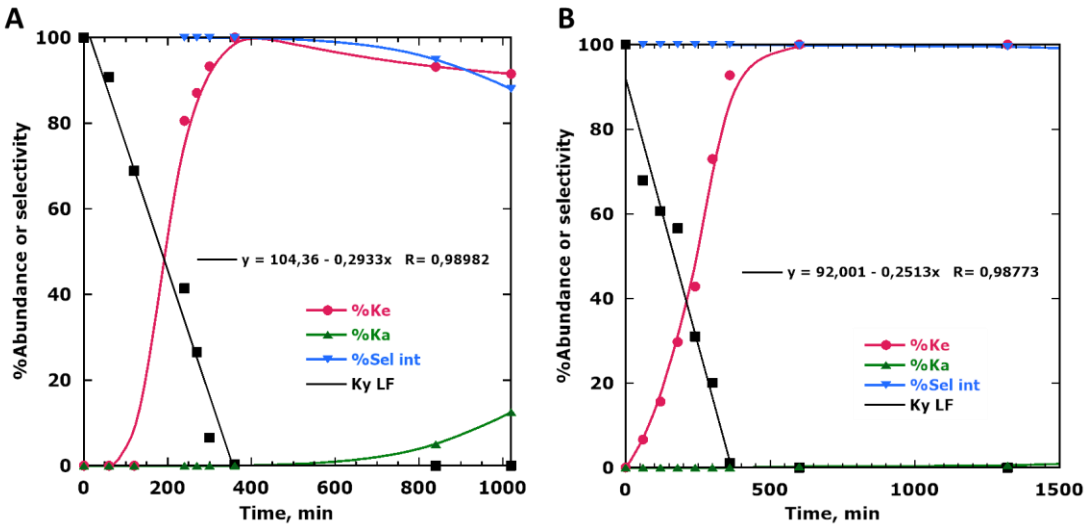

Figure S4.4.11. (A) Abundance of PhP (%Ky), its respective alkene (%Ke) and alkane (%Ka) or selectivity towards the alkene (%Sel int) vs. time. 8 mL of 6 mM alkyne solution in MeOH was stirred with 10 mg of CuPd@TiO_2 and irradiated with 25% UVA power under Ar; **(B)** Abundance of PhP (%Ky), its respective alkene (%Ke) and alkane (%Ka) or selectivity towards the alkene (%Sel int) of PhP 6mM in MeOH using 5.4 mg of CuPd@TiO_2.

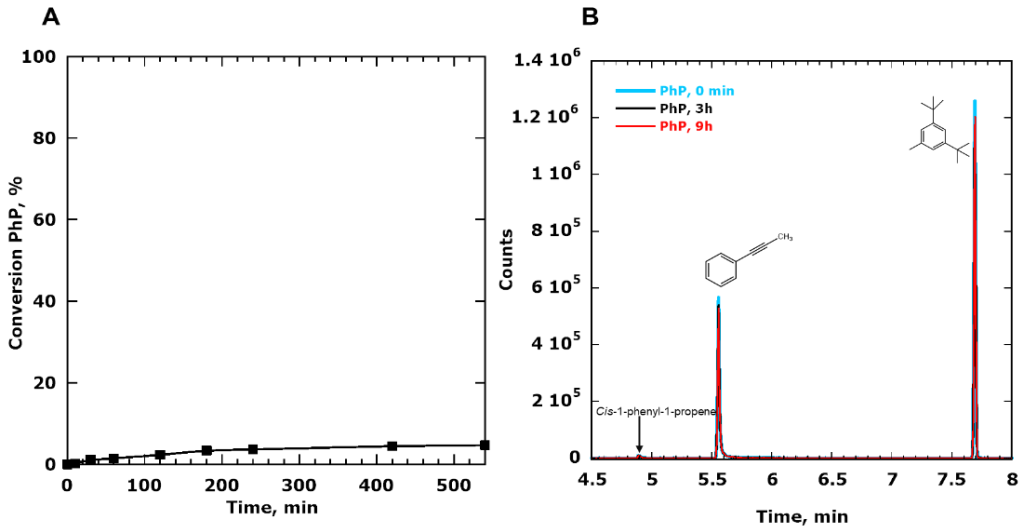

Figure S4.4.12. (A). Conversion of PhP after performing a control reaction using a 6 mM alkyne solution in MeOH, under argon, irradiated with UVA light at 100% power, with 10 mg of TiO_2 suspended in 8 mL of solution. At 540 min (9h) of time, 4.6% of the 1-phenyl-1-propyne has been consumed. Aliquots were taken at different times to monitor the reaction through GC-MS.**(B)** GC-chromatograms at 0 min, 3 h and 9 h of the reaction using PhP 6 mM in MeOH and 10 mg of TiO_2 under Ar. At 540 min (9 h) the intensity of the peak for the 1-phenyl-1-propyne (peak at 5.56 min) has been decreased a little and the *cis*-1-phenyl-1-propene is barely formed (peak at of 4.90 min). For these chromatograms, a 0.1 mL aliquot of the reaction was taken. The solution was filtered to remove the catalyst and dissolved in 0.8 mL dichloromethane (DCM). Furthermore, 0.1 mL of a 2.4 mM solution of 3,5-di-tert-butyltoluene (retention time of 7.7 min) was added to the vial as an external standard.

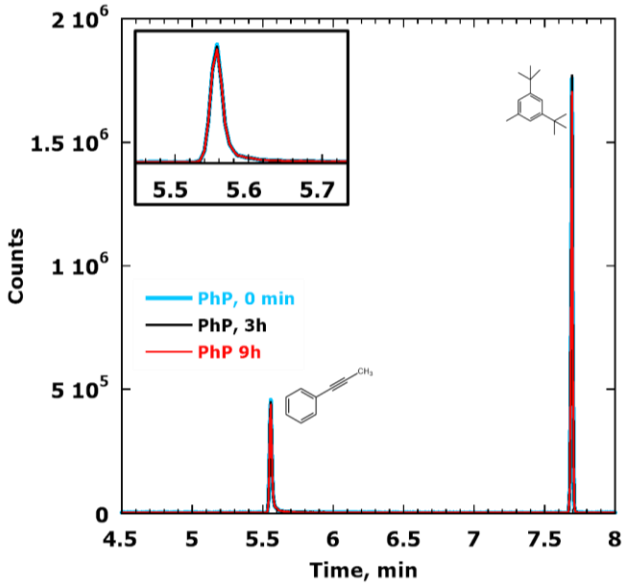

Figure S4.4.13. GC-chromatograms at 0 min, 3h and 9h of semi-hydrogenation control reaction of PhP 6 mM in MeOH using 10 mg of CuPd@TiO_2 under Ar without light. After 540 min (9h), the 1-phenyl-1-propyne (retention time of 5.56 min) has not been consumed. Usually, when light is used as part of the reaction, at 9h of reaction, all the alkyne was consumed and around 98% of *cis*-1-phenyl-1-propene (retention time of 4.90 min) was produced (Figure S4.4.11A). The inset of the figure shows a zoom-in of the PhP peak to show that it remains the same after 9h of reaction. For these chromatograms, a 0.1 mL aliquot of the reaction was taken. The solution was filtered to remove the catalyst and dissolved in 0.8 mL dichloromethane (DCM). Furthermore, 0.1 mL of a 2.4 mM solution of 3,5-di-tert-butyltoluene (retention time of 7.7 min) was added to the vial as an external standard.

5. Magnetic catalyst for efficient One-Pot Synthesis of Schiff Bases from Benzyl Alcohol and Nitro Compounds under UV irradiation

5.1. Preamble to Chapter 5

Chapter 5 explores the versatility and industrial importance of imines, specifically Schiff bases, which are highly valued for their wide applications. This chapter focuses on developing efficient methods for synthesizing Schiff bases using photocatalytic processes, wherein benzyl alcohol and nitrobenzene were used as starting materials and TiO_2, $Pd@TiO_2$, $Cu@TiO_2$ and $Fe_3O_4@TiO_2$ were used as photocatalysts. This approach aims to simplify the production of these types of imines using easily accessible and affordable chemicals, which is crucial for industries focused on scaling up and keeping costs low.

This study uses photoirradiation at a specific wavelength (370 nm) and the chosen catalysts can harness light energy to drive chemical reactions, specifically targeting the one-pot synthesis of Schiff bases under a controlled, inert atmosphere. Among the catalysts studied, $Fe_3O_4@TiO_2$, the magnetic catalyst stands out for its exceptional performance. It achieves a high production rate of 6.8 mmol h^{-1} within the first six hours of irradiation and reaches over 99% yield of the desired imine (N-benzylamine) after 20 hours. This catalyst's effectiveness is attributed to a series of catalytic reactions facilitated by the photocatalytic oxidation of benzyl alcohol to benzaldehyde and the simultaneous reduction of nitrobenzene to aniline. These intermediates then undergo catalytic condensation on the active sites of the TiO_2-metal interface, ultimately forming the Schiff base. Furthermore, the magnetic properties of the magnetic catalyst offer practical advantages in separation processes, enhancing efficiency and reducing processing times. The catalyst's reusability was also studied, demonstrating improved performance during subsequent uses, which highlights its potential for sustainable chemical transformations.

Regarding the mechanism of the reaction, we believe the way the catalyst works depends on the metal loaded to TiO_2. For example, with $Fe_3O_4@TiO_2$, it is possible that the process involves transferring electrons efficiently facilitating the Fe^{3+}/Fe^{2+} cycling. This happens because Fe^{3+} interacts with TiO_2, accelerating the nitrobenzene to aniline

conversion. Knowing this helps us design better catalysts and set up reactions for making chemicals more effectively. However, it is important to highlight that to the best of our knowledge, the role of iron in catalytic processes, particularly when it interacts with TiO_2, remains a subject of ongoing research, presenting intriguing possibilities.

Recent research shows that combines UVA and blue light (450 nm) significantly enhances the photocatalytic process, doubling the Schiff base yield and increasing benzaldehyde production. The catalyst's reusability under dual-wavelength exposure further enhances results. This approach demonstrates the promise of color-coordinated catalysis for advancing sustainable chemistry (*Catalysts, 2024, 14(9), 612*).

Overall, this chapter suggests that photocatalytic methods using metal-decorated TiO_2 catalysts, such as Fe_3O_4@TiO_2, hold significant promise for advancing sustainable and efficient chemical synthesis processes in industrial scale. This not only helps the environment, but also highlights its efficacy, while simultaneously mitigating risks associated with resource depletion, particularly evident when working with elements at risk, such as Palladium.

5.2. Pre-submission Version of Manuscript

This manuscript is currently in the process of submission.

Abstract

The versatility and significance of imines (Schiff bases) make them highly attractive for various industrial applications. Achieving high production rates using readily available and inexpensive reagents is crucial for optimizing production. This study investigates photocatalytic routes for the one-pot synthesis of Schiff bases using alcohol and an aromatic nitro compound as reagents. Utilizing photoirradiation at 370 nm with TiO_2 loaded with various metals, we demonstrate exceptional efficiency in the one-pot synthesis of Schiff bases under an inert atmosphere. Notably, our newly developed Fe_3O_4@TiO_2 magnetic catalyst offers an excellent option for synthesizing the corresponding imine (N-benzylamine), achieving a remarkable production rate of 6.8 mmol h^{-1} during the first 6 hours of irradiation, and reaching over 99% yield after 20 hours.

This success is attributed to a series of catalytic reactions involving the photocatalytic oxidation of benzyl alcohol to benzaldehyde and the simultaneous *in situ* reduction of nitrobenzene to aniline. Subsequent catalytic condensation of these products, facilitated by the active sites at the TiO_2-metal interface, ultimately yields the desired imine. The magnetic catalytic system exhibits outstanding performance, representing a promising alternative for sustainable and efficient chemical transformations. Besides this, its magnetic properties confer an advantage in separation processes, enhancing efficiency, and substantially decreasing processing times.

Manuscript

Introduction

Schiff bases are condensation products of primary amines with carbonyl compounds like aldehydes or ketones.[1,2] Its common structural feature is the azomethine (imine) group with a general formula of RN=CR' (R' ≠ H) where R and R' can be alkyl, aryl, or heterocyclic groups which can be substituted in various ways. The term Schiff base originates from Hugo Schiff, a German chemist, who in 1864 reported the first synthesis of imines and introduced a new class of organic compounds.[3,4]

These organic compounds are extensively used in different fields, and they serve multiple purposes such as dyes, catalysts, and intermediate species in organic synthesis. They can even work as polymer photostabilizers providing very good long-term stability for Polyvinyl Chloride (PVC) films through UV absorption or screening, peroxide decomposition, and radical scavenging mechanisms.[5] These compounds have also demonstrated diverse biological activities including antibacterial and antifungal activities, for example, Jarrahpour *et al*.[6] confirmed a moderate activity against tested gram-positive bacteria *Staphylococcus aureus* when using an azo Schiff base such as 2-hydroxy-3-methoxy-5 (4-methoxyphenylazo)benzaldehyde, while de Souza *et al*.,[7] proved effectiveness against *Mycobacterium tuberculosis* H37Rv, exhibiting a minimum inhibitory concentration (MIC) value of 8 μg/mL when using a Schiff base such as N-(salicylidene)-2-hydroxyaniline. On the other hand, a wide range of Schiff bases have been evaluated as adaptable ligands capable of coordinating a range of metal ions across various

coordination geometries and oxidation states and some metal complex derivatives of 2N-salicylidene-5-(p-nitrophenyl)-1,3,4-thiadiazole (HL) with Co(II), Pd(II), Rh (III) and Au (III) ions, respectively, showed moderate activity against *Staphylococcus aureus*, *Salmonella typhi,* and *Escherichia coli* strains and a slightly higher activity compared to the ligand HL *per se*.[8]

This versatility extends their applicability not only as effective antibacterial agents but also as catalysts in various homogeneous reactions, heterogeneous reactions, Heck reaction, Henry reaction, carbonylation reaction epoxidation reactions,[9] among others. Therefore, it is clear that the discovery of Schiff bases opened up opportunities across a broad spectrum of scientific disciplines. Furthermore, in different scientific reports,[1,10] Schiff bases can be synthesized through simple and versatile methods, such as the condensation reaction between primary amines and carbonyl compounds, wherein specifically, there is a nucleophilic addition of the NH_2 group from the amine (B) compound to the C=O of the aldehyde or ketone (A), resulting in the creation of a hemiaminal[11] compound (C) under reflux conditions, while simultaneously eliminating water. Subsequently, dehydration occurs, leading to the production of an imine (compound D) as shown in Scheme5.2.1:

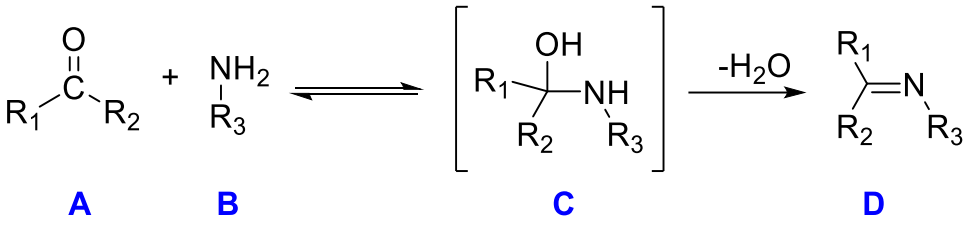

Scheme 5.2.1. Thermal Schiff Base synthesis

However, as widely acknowledged, many traditional organic transformations and syntheses involve high temperatures and sometimes, high pressures, resulting in considerable energy consumption and environmental harm. Consequently, it is essential to seek cleaner and more efficient organic synthesis methods as alternatives to conventional industrial practices. Photocatalysis has emerged as a promising technique, garnering widespread interest for its potential contributions to clean energy generation and environmental remediation. Photocatalytic synthesis of imines has been explored using

homogenous catalysts, for instance, Saranya *et al.*,[12] showed an efficient catalytic approach for the selective synthesis of imines (yields between 30-90%) in air at room temperature using diruthenium(II) complexes [(η6-p-cymene)$_2$Ru$_2$Cl$_2$(μ-L)] as a catalyst, 4-methoxybenzyl alcohol and p-anisidine as starting materials. Using heterogenous Pt@TiO_2, Shiraishi *et al.*[13] observed yields of up to 84% for N-benzylideneaniline using Pt@TiO_2 using benzyl alcohol and aniline as initial substances. As noticed from these reports, the initial reactants are primary amines and alcohols. Specifically, the utilization of anilines as substrates raises concerns due to their susceptibility to autooxidation.[14] Although this degree of autooxidation will depend on the chemical stability of the arylamine and other substitutions on the benzene ring. An alternative approach involves employing nitroarenes as reactants, culminating in a one-pot synthesis of imines via the oxidative coupling of an alcohol and a nitroarene. This method uses stable and cost-effective reactants while reducing the required synthetic steps.

This approach was previously reported by Selvam *et al.*[15] who observed the production of Schiff bases from the photoirradiation (λ = 300 nm) of TiO_2 loaded with Pd nanoparticles (2 wt%) in an aqueous solution of benzyl alcohol and nitrobenzene at room temperature for 4h. However, due to the strong hydrogenation ability of palladium, the products had higher selectivity towards secondary amines.[16] At this point, it is essential to recognize that even though Pd nanomaterials are widely used as efficient catalyst materials owing to their high specific surface area, abundant active sites, and superior catalytic activity, their continuous use raises concerns about their environmental impact.Click or tap here to enter text.Despite their valuable catalytic and optical properties, the increasing exposure of Pd nanomaterials to the ecological environment poses challenges. [17]

Similarly, Wu et *al.*,[18] reported a one-pot reaction utilizing $Cd_xZn_{1-x}S$ as a catalyst. Under visible light, the authors observed a maximum Schiff base yield of 55.2% after 4h. Nevertheless, these reactions were done under high N_2 pressure and with a large catalyst loading (6 mg/mL), which reduces the feasibility of scaling up Schiff base production. Despite this, unlike Pd, the utilization of Cadmium in such syntheses, while yielding decent results, raises concerns due to its inherent toxicity, posing substantial risks to both human health and the environment. Consequently, as highlighted by these scientific reports, the

metals employed in these investigations not only contribute to environmental degradation but also exacerbate the precarious status of certain metals, which are increasingly vulnerable to depletion. For example, Hayes *et al.,*[19] demonstrated in their study that elements such as Sc, Co, Ge, Sb, and Pd, among others, have a percentage critically higher than 60% and have a supply chain that is vulnerable to disruption. These elements serve an essential function in the manufacturing of different products, and thus their absence would have significant consequences. Thus, it becomes imperative to explore alternative materials.

To develop better environmentally friendly alternatives, we propose exploring the photocatalytic activity of four TiO_2-based heterogeneous catalysts for the synthesis of Schiff bases. We chose widely used photocatalysts such as P25 and Pd@TiO_2 and compared their activity with new alternatives involving first-row transition metals like Fe and Cu on TiO_2 (Fe_3O_4@TiO_2 and Cu@TiO_2). Aiming at practical industrial applications and greener alternatives, we tested our catalysts in a one-pot approach for the synthesis of imines, starting from nitrobenzene and benzyl alcohol. Our initial efforts showed that Fe_3O_4@TiO_2 exhibits similar activity to Pd@TiO_2 and TiO_2 catalysts. Considering the experimental results, along with concerns about element depletion and the environmental impact of certain chemicals, iron presents itself as a viable option. Additionally, Fe_3O_4 nanoparticles exhibit superparamagnetism, enabling magnetic separation in the presence of a magnetic field. The reactions were driven using UVA irradiation, the spectral region largely absorbed by TiO_2. We also measured the time profile evolution of the reaction, showing production rates of up to 6.8 mmol/h, which is more than ten times higher than previously reported. These findings suggest that the reaction conditions are ideal for scaling up.

Experimental details

All chemicals were purchased from Sigma Aldrich and used as received unless otherwise stated. TiO_2 P25 was purchased from Univar Canada.

Catalyst Synthesis

Fe_3O_4@TiO_2: Magnetic TiO_2 NPs were synthesized by in situ precipitation of Fe_3O_4 on TiO_2 NPs. In brief, a 0.32 mg/mL aqueous solution of commercial P25 was added to a 3-neck round bottom flask. To this solution, 0.56 g of $Fe(NO_3)_3 \cdot 9H_2O$ and 0.32 g of $FeSO_4 \cdot 7H_2O$ were added, to obtain a proportion of 2:1 of Fe (III) to Fe(II). The solution was purged for 10 min and then heated at 85°C and kept at this temperature for 10 min under N_2 flow, to equilibrate the temperature. To this solution, 360 µL of NH_4^+ was added dropwise and the resulting dark solution was kept under N_2 for another 10 min. The resulting material was separated using an external magnet washed five times with Milli-Q water and dried under vacuum.

Pd@TiO_2: Based on a reported synthesis.[20] Approximately 15 mg of metal precursor salt ($PdCl_2$) was mixed with TiO_2 (~500 mg) in 150 mL of Milli-Q water and sonicated for 20 min. The slurry was irradiated in a Luzchem photoreactor equipped with 14 UVA bulbs for 24 h with vigorous stirring in a crystallizing Pyrex® dish with a Pyrex® cover. The slurry was centrifuged and washed with Milli-Q water four times to remove unreacted metal precursor salt and dried overnight in a desiccator under vacuum. The obtained powder had a dark grey colour.

Cu@TiO_2: Based on a reported synthesis.[20] A total of 55 mg of $CuCl_2 \cdot 2H_2O$ were mixed with TiO_2 (~300 mg) and 95 mg of the benzoin-type photoinitiator Irgacure-2959 in 130 mL of Milli-Q water and purged with argon for 15 min. After this, the slurry was irradiated in a Luzchem photoreactor equipped with 14 UVA bulbs for 24 h with vigorous stirring. The slurry was filtered and washed with Milli-Q water at least seven times to remove unreacted metal precursor salt and dried overnight in a desiccator under vacuum. The powder had an intense beige colour with green tones.

Catalyst Characterization

Transmission electron microscopy (TEM) images were collected on a JEM2100F FETEM (JEOL) operating at 200 kV. Diffuse reflectance measurements were carried out

using an Agilent Cary 7000 UV-Vis-NIR Universal Measurement Spectrophotometer coupled with an Agilent praying Mantis accessory. The metal composition of the materials was determined by Inductively Coupled Plasma Optical Emission Spectrometry (ICP-OES), using an Agilent Vista Pro ICP Emission Spectrometer. Approximately 10 mg portions were accurately weighed in triplicate and digested with *aqua regia*. Solutions were further diluted and measured by ICP-OES. The following emission lines were used for quantification when applicable: Fe 238.20 nm, Pd 340.45 nm, and Cu 327.39 nm. Powder X-ray diffraction analysis was carried out at room temperature utilizing a Bruker D8 Endeavor Polycrystalline X-Ray Diffractometer (PXRD) in Bregg Brentano geometry, using Cu Kα radiation (λ = 1.5418 Å), powered at 40 kV and 25 mA (1kW). Diffractograms were collected by a LynxEye XE-T 1-D silicon strip detector with 192 channels, with 2θ range from 20° to 90°.

Photocatalytic activity

The photocatalytic performance of the synthetized catalysts was performed by adding 5 mL of fresh solution of nitrobenzene (0.1 M) in benzyl alcohol in a Pyrex glass tube, loaded with 10 mg of the catalyst. The solution was sonicated and purged for 10 min with N_2. Irradiation was done using a UVA LED (λ=370 nm) with an irradiance power of 13.5 $mW.cm^{-2}$ (Figure S5.4.1.). Samples were irradiated and stirred for up to 6 h. The catalysts were removed using a hydrophilic PTFE syringe filter, with 0.2 µm pore size. Quantification of products was performed by mass spectrometry in an Agilent 6890-N Gas Chromatograph with an Agilent 5973 mass selective detector, 3,5-Di-tert-butyltoluene (4 mM in Dichloromethane as the solvent) as an external standard. The timed events feature was used within the setpoint control of the local user interface (OFF at 6.20 min/ON at 8.70 min) to prevent an excessive concentration of Benzyl Alcohol from reaching the detector.

Results and Discussion

Catalyst Characterization

In this work, we selected four TiO_2-based catalysts to evaluate possible photocatalytic routes for one-pot imine synthesis. Transmission electron microscopy

(TEM) was used as a powerful tool to learn more about the nanoparticles, their morphology, and spatial distribution. Figure 5.2.1 shows the TEM images of the catalysts, unveiling the distinctive spherical morphology of the nanoparticles (NPs). Upon closer examination of Figure 5.2.1, it becomes evident that the NPs were deposited onto the catalyst surface. This deposition is particularly visible in panel B, for Pd@TiO_2, where the TEM image distinctly shows the presence of diminutive particles decorating the TiO_2 surface. The same scenario is visible for panels C and D. Previous publications in our group,[20] have shown that the mean particle size of the metallic NPs is around 3.0 ± 0.2 nm. Since the distinction between two metal-oxide in TEM is challenging due to the similar electron densities, we could not measure the diameter of the Fe_3O_4 over P25. However previous publications from our group, using the same synthetic route, produced NPs with diameters around 12.5 ± 3 nm.[21]

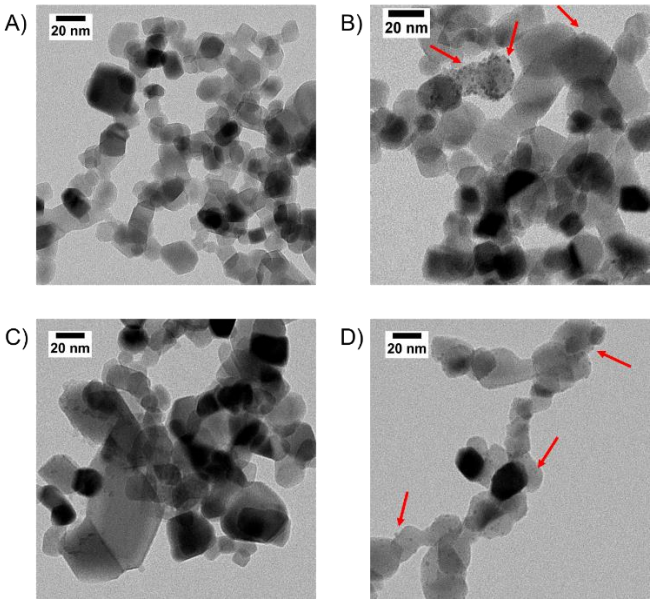

Figure 5.2.1. Representative TEM images of TiO_2 **(A)**, Pd@TiO_2 **(B)**, Fe_3O_4@TiO_2 **(C)** and Cu@TiO_2 **(D)**. Red arrows indicate representative Pd and Cu nanoparticles on P25. Scale bar: 20 nm.

For the bimetallic nanoparticles (NPs), metal loadings were determined using inductively coupled plasma optical emission spectroscopy (ICP-OES) analysis, as shown in Table 5.2.1. Synthesis via photo-deposition resulted in lower metal loadings of 2% and 3% for Pd and Cu, respectively. Iron oxide on TiO_2 was synthesized by co-precipitation on

the semiconductor surface, yielding a 12% loading. The higher loading of iron oxide was intentional, aiming to explore magnetite's catalytic properties, and its magnetism, which facilitates catalyst removal. Indeed, after synthesis, Fe_3O_4@TiO_2 demonstrated a response to an external magnetic field, as shown in Figure S5.4.2.

Table 5.2.1. Metal loading of the three bimetallic catalysts evaluated in this work. Metal quantification was done using ICP-OES following Fe, Pd, and Cu emission lines.

Material	**Metal Loading (%)**
Fe_3O_4@TiO_2	12 wt % (± 0.93) Fe
Pd@TiO_2	2.0 wt % (± 0.85) Pd
Cu@TiO_2	3.0 wt % (± 0.94) Cu

Moreover, X-ray diffraction (XRD) helped us to provide insights into the crystalline structures of the synthesized materials. For our tests, P25 was the source of titanium dioxide. P25 is formed from TiO_2 nanoparticles, with a diameter between 10-50 nm (Figure 5.2.1A), composed of 80 % anatase and 20 % rutile phase.[22] The diffractogram of P25 (Figure 5.2.2) confirms its crystalline structure. Peaks assigned for anatase and rutile are identified as A and R, respectively, according to ICCD cards n° 01-083-5916 and 01-076-1940. In the diffractogram, for all the metal-loaded TiO_2 catalysts the same peaks assigned to TiO_2 (P25) can be identified (Figure 5.2.2). From the diffractogram of Cu@TiO_2, we could identify the structure of the Cuprite (Cu_2O) (ICCD: 96-900-7498), a cubic-shaped crystal formed from the oxidation of Cu^0. The diffractogram peaks assigned to Cu_2O can be found at 2θ values 36.4°, 42.3°, and 61.4°, relative to the crystal planes (111), (020), and (022), respectively.

On the other hand, XRD of Fe_3O_4@TiO_2 reveals the formation of cubic magnetite (Fe_3O_4), according to ICCD card n° 04-009-8439, using the peaks corresponding to the planes (220), (311), (400) and (511), at 2θ values of, 29.9°, 35.3°, 43.0°, and 56.9° to detect the crystal form. As for Pd@TiO_2 we can observe the dominance of TiO_2 peaks, with the only identifiable peak for Pd being at 2θ of 40.01°, which corresponds to the (111) plane of cubic Pd (ICCD: 96-153-4922).

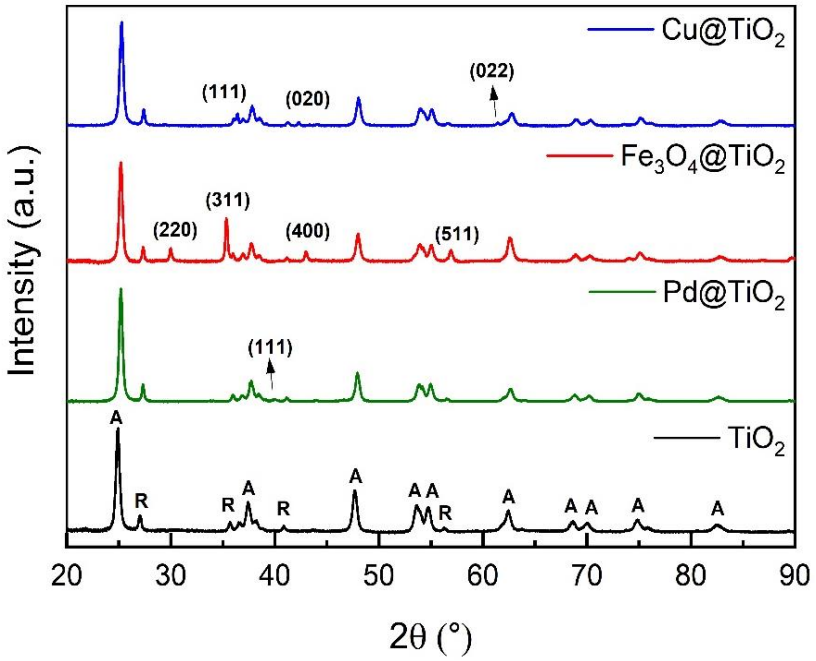

Figure 5.2.2. XRD patterns of the catalysts used: TiO_2 (P25) (black), Pd@TiO_2 (green), Fe@TiO_2 (red) and Cu@TiO_2 (blue). Numbers in parenthesis correspond to the characteristic (h k l) interplanar planes for each crystalline phase. A: anatase TiO_2 and R: rutile TiO_2

In addition, diffuse reflectance measurements were carried out for all the catalysts to study their optoelectronic properties. Measurements were recorded between 200 nm and 800 nm using the diffuse reflectance mode. The addition of the metal on P25 did shift the catalyst absorbance into the visible range (Figure S5.4.3), a change that is more pronounced on Fe_3O_4@TiO_2, due to the higher loading percentage.

Selecting the Optimal Catalyst: Exploring variations for enhanced reaction performance

At the beginning of our studies, we aimed to evaluate whether the system chosen yields imines using benzyl alcohol and nitrobenzene as reagents. Benzyl alcohol was chosen as an alkylation surrogate for aldehydes due to its cost-effectiveness. Previous research has demonstrated that an excess of benzyl alcohol enhances the reaction, thus we employed it as a solvent, facilitating potential solution reusability.[23,24]

Across all reactions, the primary products observed included benzaldehyde (BenzA), and N-Benzylideneaniline (Schiff-base). Additionally, the GCMS trace shows a few peaks at 12.21 min and 13.50 min that appeared to be contaminations as they are shown in the chromatogram before the reaction started. A representative chromatogram is depicted in Figure 5.2.3 when using Fe_3O_4@TiO_2 as the catalyst. The mass spectra of the products shown in Figure 5.2.3 can be seen in Figure S5.4.4. Specifically, a tandem process occurred wherein the nitroarene undergoes reduction to form an aromatic amine through interaction with the alcohol, concurrently oxidizing the alcohol to yield the aldehyde (BenzA). Following this process, the aldehyde (BenzA) and the amine (aniline) coupled to produce the corresponding imine (Schiff Base, N-Benzylideneaniline). The presence of BenzA demonstrates the successful oxidation of the Benzyl alcohol for all catalysts (Figure S5.4.5-S5.4.7) and its high abundance is attributed to the chosen stoichiometry.

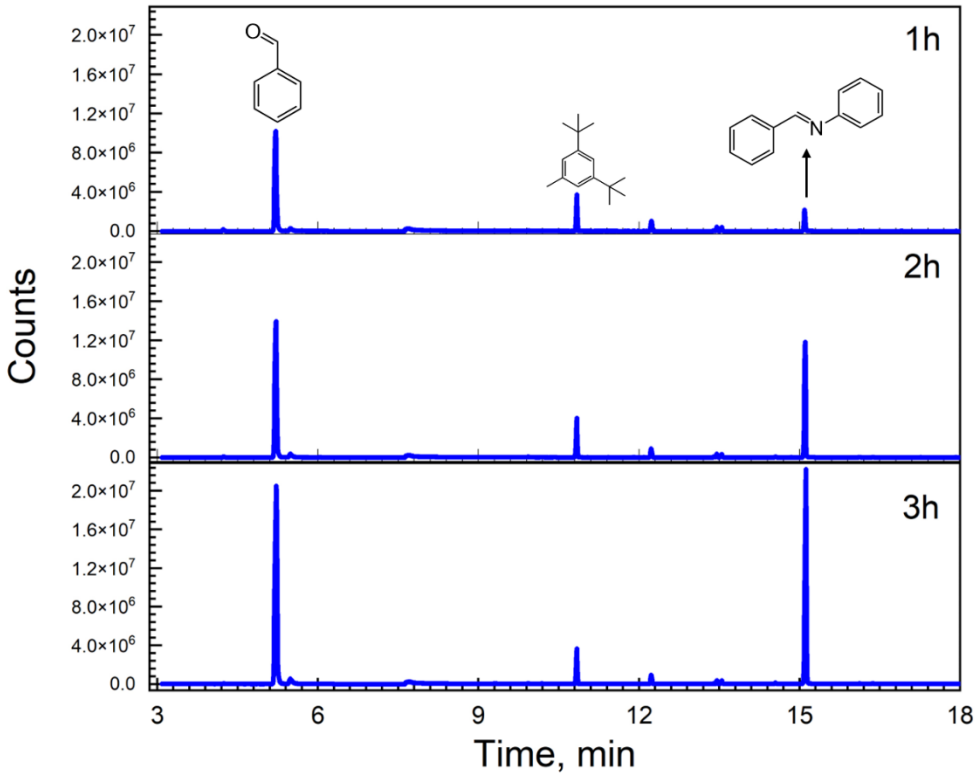

Figure 5.2.3. Chromatograms showing the peaks obtained after performing the reaction with nitrobenzene 0.1 M in benzyl alcohol and 10 mg of Fe_3O_4@TiO_2. 5 mL of solution was irradiated for 3h under UVA irradiation and continuous stirring. Samples were taken

every hour and filtered using a PTFE syringe filter. 3,5-Di-tert-butyltoluene was used as an external standard (peak at 10.84 min) The products have the following retention times: BenzA (5.17 min), 3-Benzylaniline (3-BA) (12.21 min), Schiff Base (15.10 min). The timed events feature of the local user interface was used (Turned off at 6.20 minutes and activated at 8.70 minutes) to prevent the risk of a high concentration of Benzyl Alcohol reaching the detector.

Aniline is also one of the products, although is at low concentrations, indicating our catalysts' ability to successfully oxidize the Benzyl alcohol while reducing the nitrobenzene to aniline. In our study, gas chromatography analysis revealed a challenge in detecting the aniline peak due to its proximity to the retention time of the solvent (benzyl alcohol) when nitrobenzene was employed as the substrate. However, our subsequent experiment using 3-nitroanisole (3-NA) keeping benzyl alcohol as the solvent and Fe_3O_4@TiO_2 as the catalyst, yielded more distinct results as depicted in Figure 5.2.4. In this particular case, although *m*-anisidine was present in relatively low concentrations, was discernible in the chromatogram (retention time of 9.63 min), indicative of our catalysts' proficiency in facilitating the oxidation of benzyl alcohol while concurrently reducing nitro compounds to amines. This observation underscores the importance of substrate selection and catalyst design in optimizing reaction outcomes, providing valuable insights for the development of efficient catalytic systems.

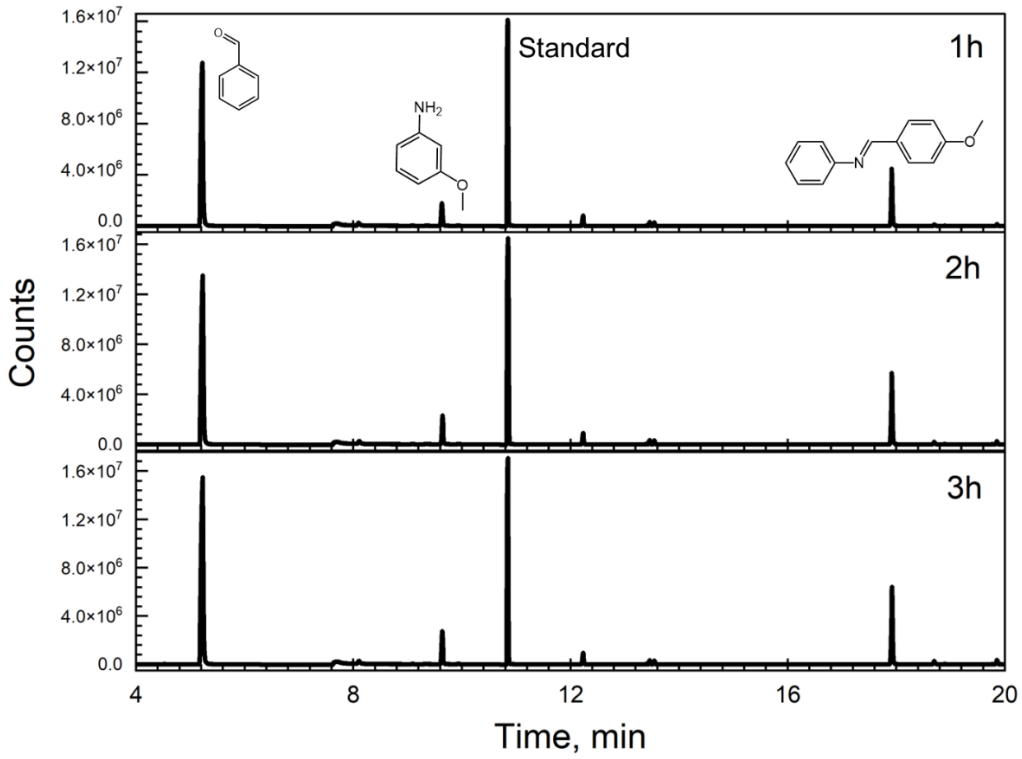

Figure 5.2.4. Chromatograms showing the peaks obtained after performing the reaction with 3-nitroanisole 0.1 M in benzyl alcohol and 10 mg of Fe_3O_4@TiO_2. 5 mL of solution was irradiated for 3h under UVA irradiation and continuous stirring. Samples were taken every hour and filtered using a PTFE syringe filter. 3,5-Di-tert-butyltoluene was used as an external standard (peak at 10.84 min) The products have the following retention times: BenzA (5.17 min), *m*-anisidine (9.63 min), Schiff Base N-(4-Methoxybenzylidene)aniline (17.94 min). The timed events feature of the local user interface was used (Turned off at 6.20 minutes and activated at 8.70 minutes) to prevent the risk of a high concentration of Benzyl Alcohol reaching the detector.

As evidence, Figure 5.2.4 demonstrates the continued success of this study, namely, the synthesis of the Schiff base. However, a comparison of the results depicted in Figures 5.2.3 and 5.2.4 reveals a notable distinction: following a 3-hour reaction period, the peak intensity observed when using nitrobenzene as the starting substrate is higher than that of 3-nitroanisole. This difference can be explained due to the electronic effects. In fact, when

comparing the electron density contributions of the nitro group in molecules like nitrobenzene to that of the methoxy group on the aromatic ring, the electron-donating effect of the methoxy group is stronger. [25] This leads to a lower electron density around the nitro group in 3-anisole, which indicates that the electronic effect of substituents on the aromatic ring is also an important factor for reaction rates. Additionally, as stated by Hirao *et al.*,[26] analyzing the electronic structure and the distribution of electron density within the benzene ring is important to determine the reactivity of the ortho, meta, and para positions of the substituted benzene ring when being exposed to an electrophile. In this case, the presence of a methoxy group likely enhances electron density within the ring. However, it is reasonable to think that this alteration in electron density might potentially modify the molecule's reactivity towards the electrophilic carbonyl of benzaldehyde, altering its susceptibility to form the Schiff base.

We then proceeded to compare the photocatalytic activity of four TiO_2-based catalysts. In our comparative analysis, we subjected the samples to irradiation for up to 3 hours and observed varying imine yields dependent on the catalysts employed. As evidenced in Figure 5.2.5, Pd@TiO_2 exhibited a maximum production of 26.9 mmol (27 %) after 3h of irradiation (Figure 5.2.5). Remarkably, Pd@TiO_2 was the only catalyst capable of yielding the fully reduced product, N-Benzylaniline. This observation is highlighted in Figure S5.4.6 where a distinct peak began to appear around 15.65 min at the 2-hour mark. This is a result of the strong hydrogenation ability of noble metals, which decreases the selectivity towards the desired imine.[15,16,27] TiO_2 had a similar Schiff base, producing 28.7 mmol (Figure 5.2.5). Prior publications had showcased the potential of TiO_2 for the tandem imine formation from alcohols and nitroarenes.[28,29] In particular, P25 takes advantage of rutile's high photocatalytic reduction of nitrobenzene coupled with the higher concentration of Lewis acid sites on anatase which facilitates the condensation of BenzA and aniline.[28]

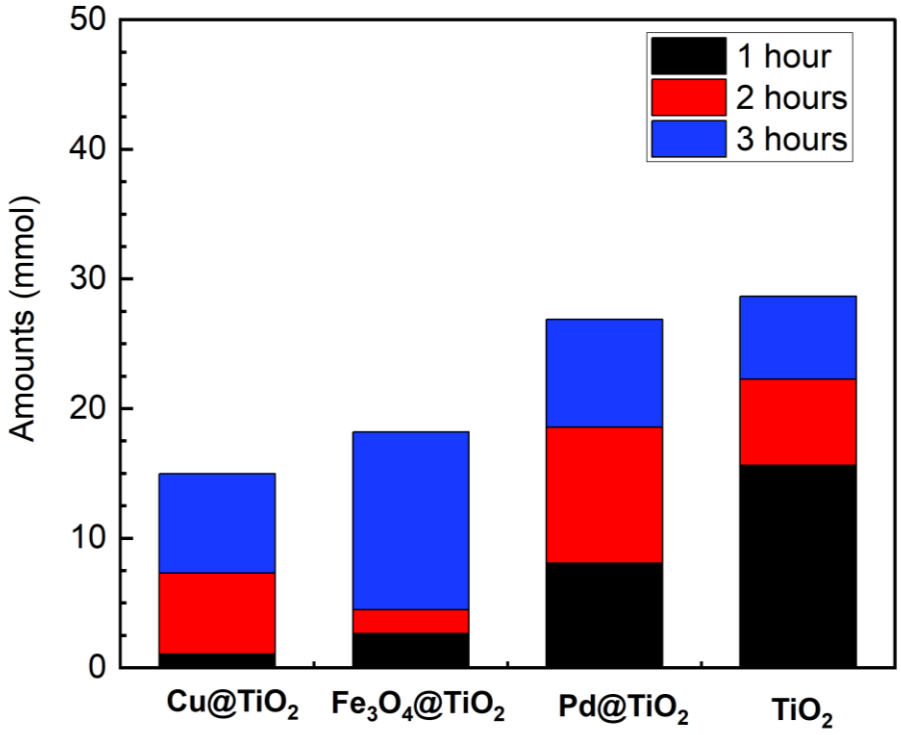

Figure 5.2.5. Photocatalytic performance for the selectively generated Schiff Base N-Benzylideneaniline in the coupled system of benzyl alcohol and nitrobenzene using different catalysts under UVA light irradiation for 1-3 h. Reaction conditions: benzyl alcohol (as the solvent, 5 mL), nitrobenzene (0.1 mmoles/L), M@TiO_2 (10 mg), under Argon, UVA light irradiation (λ= 370 nm). Schiff-base production was quantified using GC-MS.

Interestingly, the Fe and Cu-loaded catalysts exhibited a delayed onset in catalyzing conversion, evident from their low yields within the initial 2 hours, followed by a pronounced increase in yield from 2 to 3 hours. In our previous studies with Cu@TiO_2, we observed a similar slower catalytic rate compared to Pd-loaded TiO_2 in the hydrogenation of alkynes.[20] Just as with the alkynes, Cu exhibited superior control over the selectivity of the reaction, while Pd excelled in enhancing its rate. This difference highlights how various catalysts play a crucial role in controlling both the speed and specificity of chemical reactions.

Despite their slower kinetics relative to other catalysts, Cu@TiO_2 and Fe_3O_4@TiO_2 demonstrated substantial Schiff-base formation within a short timeframe, 15.3 and 18 mmol, respectively (Figure 5.2.5). This contrasts with previous reports utilizing Fe and Co-based catalysts, where reaction completion often required days,[23,24] showing that the association with TiO_2 is beneficial to improve the yields for those catalysts. It is also noteworthy that we did not employ bases, in contrast with prior reports, [23,24,30,31] and yet achieved satisfactory yields in a short timeframe.

Based on the previous results, P25 exhibited higher yields in the synthesis of Schiff bases, however, its powdered form hinders separation processes, often requiring an extra centrifugation step. In contrast, Fe_3O_4@TiO_2 offers the distinct advantage of magnetic removal, facilitating the separation process while keeping good reaction yields. Therefore, recognizing this advantage, we have directed our efforts towards enhancing the yield of this magnetic catalyst, as its facile removal makes it an attractive candidate for scaling up applications in organic synthesis.

Optimizing reaction conditions using Fe_3O_4@TiO_2 as a catalyst

The first observation was that the reactions using Fe_3O_4@TiO_2 had a delayed start compared to pure TiO_2. Consequently, we first evaluated the Schiff base yield at longer irradiation times and compared it with TiO_2 alone. After running the reactions with both catalysts for 6 hours, P25 produced 36.6 mmol (Table 5.2.2, entry 2) of the Schiff base, while Fe_3O_4@TiO_2 produced 41.7 mmol base (Table 5.2.2, entry 1). This results in a Schiff base rate of 6.8 $mmol^{-1}$, which is over ten times higher than the values previously published, which has rates ranging from 4.6 μmol h^{-1} to 0.34 mmol h^{-1} reported[28,29,32–35] (Table S5.4.1). Noting that the magnetic catalyst performs better with extended irradiation we conducted it for 20 hours, achieving over 99% of the desired product. Thus, even with the longer irradiation time, we obtained a significantly high production rate of 4.95 mmol h^{-1}.

We also investigated whether the catalytic delay persisted during a second use of the catalyst. To test this, we conducted a reaction for 3 hours under UVA irradiation. After this period, 0.1 M of fresh nitrobenzene was added to the solution, which would avoid wasting the excess benzyl alcohol and the produced BenzA. The reaction was then irradiated for

another three hours. Figure S5.4.10 compares the results from the first and second uses of the catalyst difference between the first use of the catalyst. During the first use, Fe_3O_4@TiO_2 produced 13.8 mmol of N-benzylamine after three hours. However, during the second use, the catalyst yielded over 44.3 mmol of the desired Schiffbase in the same time frame.

Afterwards, we proceed to evaluate changes in lighting conditions to enhance the Schiff base production yield. We compared the product yield at the 3-hour mark for all the optimization reactions. Since irradiance can alter the distribution of products,[36,37] we evaluated the resulting imine yields at lower irradiance. For our system, reducing the irradiance resulted in a lower Schiff base yield (Table 5.2.2, entry 4). Next, we evaluated the influence of wavelength by irradiating the reaction with a blue LED (450 nm), which excites the iron oxide but not TiO_2. This led to a substantial production of BenzA, while neither Schiff base nor amine was detected (Table 5.2.2, entry 3 and Figure S5.4.8). Likewise, the absence of irradiation resulted in no Shiff base formation (Table 5.2.2, entry 6 and Figure S5.4.9) and a significantly lower BenzA (5.17 min) production. These results suggest that TiO_2 excitation is required for the reaction to occur.

Table 5.2.2. Optimizing Schiff-base yield produced Fe_3O_4@TiO_2 as a catalyst.[a] Reusing the catalyst and the Benzyl alcohol solution after 3 hours irradiation.

Entry	Catalyst	Light source	Irradiance ($mW.cm^{-2}$)	Time (h)	Yield Schiff base (%)	Amounts per hour ($mmol\ h^{-1}$)
1	Fe_3O_4@TiO_2	**370 nm**	**13.5**	**6**	**41.6**	**6.9**
2	TiO_2	**370 nm**	**13.5**	**6**	**36.7**	**6.1**
3	Fe_3O_4@TiO_2	**370 nm**	**13.5**	**20**	**> 99**	**4.95**
4	Fe_3O_4@TiO_2	**370 nm**	**5.3**	**3**	**1.9**	**0.63**
5	Fe_3O_4@TiO_2	**450 nm**	**13.0**	**3**	**ND**	**ND**
6	Fe_3O_4@TiO_2	**None**	**NA**	**3**	**ND**	**ND**
7	Fe_3O_4@TiO_2	**370 nm**	**13.5**	**3[a]**	**44.3**	**14.76**

Mechanistic Insights into the Synthesis of Schiff Bases from Nitrobenzene and Benzyl Alcohol

Based on our previous findings, we propose a plausible mechanism to elucidate the synthesis of Schiff Bases from nitrobenzene and benzyl alcohol catalyzed by M@TiO_2. Initially, the photocatalytic reaction on M@TiO_2 is initiated by the photoexcitation of TiO_2, leading to the generation of electron (e^-) and hole (h^+) pairs. The moderate oxidation potential of the photogenerated holes allows the h^+ to oxidize benzyl alcohol, yielding BenzA and hydrogen ions (H^+). BenzA was identified as one of the main products in our experiments, which is crucial in this process. The H^+ ions formed are subsequently reduced on the surface of the metal to generate H-metal species. This is the case of Pd@TiO_2, in which it has been proposed that Pd-H species will likely form in materials like Pd-decorated TiO_2 (Pd@TiO_2) when exposed to light.[38] In fact, Paul Sabatier who won the Nobel Prize in 1912,[27] worked with Nickel (Ni) and different molecules such as hydrocarbons, alcohols, and acids, mentioned that the hydrogen coming in contact with the metal of a catalyst forms very quickly on the surface of each grain. These species can serve

as active sites for reducing agents on the surface of Pd, facilitating specific reactions like converting nitrobenzene into aniline. This affirmation is supported by our experiment using 3-nitroanisole, where *m*-anisidine, an aniline derivative, was identified. The catalytic condensation of BenzA with aniline on the Lewis acid sites of the TiO_2 surface leads to the formation of the Schiff base. Our experimental results, particularly, highlighted in Figure 5.2.5, demonstrate the efficiency of this reaction on the M@TiO_2 catalysts.

The reaction could vary depending on the metal used to decorate TiO_2. For instance, for Fe_3O_4@TiO_2, we propose that upon catalyst excitation, the holes generated on the catalyst surface may oxidize benzyl alcohol, as described for Pd@TiO_2. Additionally, iron species could facilitate electron transfer, enabling the reduction of nitrobenzene to aniline.[39] Indeed, Xu *et al.*[40], found out that when TiO_2 interacts with Fe^{+3}, it affects how quickly Fe^{+3} is reduced to Fe^{+2}. Particularly, in the presence of P25, Fe^{2+} is formed much faster and accumulates in larger amounts at the beginning of the reaction. This is likely due to the positive energy difference between the conduction band (CB) of TiO_2, and the CB of Fe_3O_4[41]. This difference allows for easy transfer of the photogenerated e^- to the magnetic catalyst, facilitating the Fe^{3+}/Fe^{2+} cycling[41,42]. During the regeneration of Fe^{3+}, the electrons could potentially reduce nitrobenzene to aniline.

A plausible scenario for the described situation is depicted in Figure 5.2.6. Another possible route involves photogenerated electrons helping in the reduction of nitrobenzene to form aniline in the presence of H^+ ions. H-Fe species may also be generated, assisting in the reduction of the nitro moiety, yielding an amine. This process could lead to the condensation between benzaldehyde and aniline.[30] However, it is important to highlight that as mentioned by Moniz *et. al.*[39], who also worked with a nanocomposite of iron, the role of this metal in catalytic processes, particularly when it interacts with TiO_2, remains a subject of ongoing research, presenting intriguing possibilities. While some studies propose that its presence facilitates hole transfer, others suggest its involvement in electron transfer mechanisms.[43,44] Recent investigations have highlighted the electron transfer phenomena occurring between iron and TiO_2.[45]

It is crucial to note that light plays a significant role in the mechanism. Specifically, prolonged photoirradiation significantly enhances the production of the Schiff Base, as

evidenced by the increase in yield from 19 % after 3 hours of irradiation to almost 99 % after 20 hours of UVA irradiation when using the novel metallic catalyst (Figure 5.2.5 and Table 5.2.2). Thus, extending the duration of photoirradiation results in a more efficient reaction given the greater number of photons available to interact with the reactants on the catalyst surface. This increased photon exposure allows more reactions to occur, leading to higher conversion of the reactants into the desired Schiff base product. The M@TiO_2 catalysts facilitate the reaction between the reactants under UVA irradiation, a fact that was confirmed when experimenting without light (Figure S5.4.9), and no Schiff base was identified. Thus, the metallic component likely acts as a co-catalyst, enhancing the efficiency of the overall reaction. In summary, our study elucidates the steps involved in the synthesis of Schiff bases, providing crucial insights into the catalytic activity and reaction kinetics of different M@TiO_2 catalysts. It is noteworthy that, to the best of our knowledge, Fe_3O_4@TiO_2 catalyst has exhibited remarkable efficiency in facilitating Shiff base synthesis. This finding highlights the promising potential of iron-based catalysts for this reaction, emphasizing their importance in catalysis research. Additionally, its abundance and cost-effectiveness, offer a more sustainable alternative. This not only addresses environmental concerns but also highlights its efficacy, while simultaneously mitigating risks associated with resource depletion, particularly evident when working with Palladium.

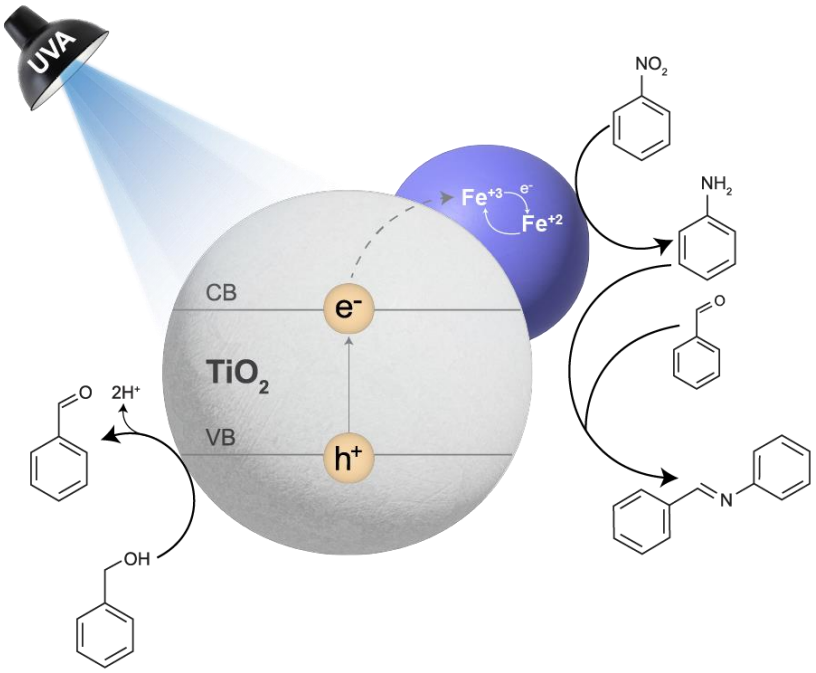

Figure 5.2.6. Plausible scenario to understand the activity shown by Fe_3O_4@TiO_2. Figure inspired by similar concepts in the literature.[46]

Conclusions

To the best of our knowledge, the use of Fe_3O_4@ TiO_2 in organic synthesis, such as in the formation of Schiff Bases is not widespread. However, we want to underscore its potential for broader applications due to several features. Our study strongly indicates the potential efficacy of using Fe_3O_4@TiO_2 for synthesizing Schiff Bases. When irradiating the reaction comprising nitrobenzene and benzyl alcohol and the magnetic catalyst for 3 hours, we observed a Shiff base production of approximately ~18%. Impressively, extending the reaction duration to 20 hours resulted in nearly 99% production of the desired product. In contrast, analogous systems such as Pd@TiO_2 and Cu@TiO_2 exhibited adequate production of the Schiff base; however it is often accompanied by undesirable over-hydrogenation products, particularly notable in the case of Pd. By refining the experimental parameters, we have identified the optimal conditions for the magnetic catalyst. Our findings highlight the promising catalytic role of Fe_3O_4@TiO_2 in the field of

catalysis research, given its ability to easily separate from the mixture reaction. This catalyst presents an alternative to address not only environmental concerns but also to mitigate the use of scarce resources such as Palladium.

Supplementary materials: Figures S5.4.1–S5.4.10: GC-MS characterization, and MS spectra of the products. These results were obtained when performing the reactions with nitrobenzene and aniline under UVA irradiation, inert atmosphere, and M@TiO_2. Spectral irradiance of the light sources employed in the synthesis of the Schiff base is shown. Control experiments without light are depicted and a picture of Fe_3O_4@TiO_2 after its synthesis next to a magnet to demonstrate its response to an external magnetic field is provided. Additionally, the reusability of the magnetic catalyst is shown in Figure S5.4.10 and Table S5.4.1 shows a comparison illustrating the findings of this study alongside previous scientific publications.

Funding: This research was funded by the Natural Sciences and Engineering Research Council of Canada, the Canada Foundation for Innovation and the Canada Research Chairs Program.

Data Availability Statement: Original data are available from the corresponding author upon reasonable request.

Conflicts of Interest: The authors declare no conflict of interest.

5.3. References

1. K. Mahmood, M. J. Maah, I. Bin Yusoff, M. A. Ashraf, A. Wajid and I. Yusoff, *International Conference on Chemistry and Chemical Process*, 2011.

2. E. Raczuk, B. Dmochowska, J. Samaszko-Fiertek and J. Madaj, *Molecules*, 2022, **27**, 787.

3. H. Schiff, *Giornale di Scienze Naturali ed Economiche (in Italian)*, 1866, **2**, 201–257.

4. H. Schiff, *Annalen der. Chemie und. Pharmacie. (in German)*, 1866, **3**, 343–370.

5. E. Yousif, A. A. Al-Amiery, A. Kadihum, A. A. H. Kadhum and A. B. Mohamad, *Molecules*, 2015, **20**, 19886–19899.

6. A. A. Jarrahpour, M. Motamedifar, K. Pakshir, N. Hadi and M. Zarei, *Molecules*, 2004, **9**, 815–824.

7. A. O. De Souza, F. C. S. Galetti, C. L. Silva, B. Bicalho, M. M. Parma, S. F. Fonseca, A. J. Marsaioli, A. C. L. B. Trindade, R. P. F. Gil, F. S. Bezerra, M. Andrade-Neto and M. C. F. De Oliveira, *Quimica. Nova*, 2007, **30**, 1563–1566.

8. E. Yousif, A. Majeed, K. Al-Sammarrae, N. Salih, J. Salimon and B. Abdullah, *Arabian. Journal of Chemistry*, 2017, **10**, S1639–S1644.

9. V. K. Juyal, A. Pathak, M. Panwar, S. C. Thakuri, O. Prakash, A. Agrwal and V. Nand, *Journal of Organometallic Chemistry*, 2023, 999.

10. E. Çınar, E. Başaran, Ö. Erdoğan, R. Çakmak, M. Boğa and Ö. Çevik, *Journal of the Chinese Chemical Society*, 2021, **68**, 2355–2367.

11. I. J. Pharm and A. A. Mahmood, *Iraqi Journal of Pharmaceutical Sciences*, 2022, **18**, 180–193.

12. S. Saranya, R. Ramesh and J. Grzegorz Małecki, *European Journal of Organic Chemistry*, 2017, **2017**, 6726–6733.

13. Y. Shiraishi, M. Ikeda, D. Tsukamoto, S. Tanak and T. Hirai, *Chemical Communications Journal*, 2011, **47**, 4811–4813.

14. A. G. Siraki, *Advances in Molecular Toxicology*, Elsevier B.V., 2013, 7, 39–82.

15. K. Selvam, H. Sakamoto, Y. Shiraishi and T. Hirai, *New Journal of Chemistry*, 2015, **39**, 2467–2473.

16. L. Geng, W. Jian, P. Jing, W. Zhang, W. Yan, F. Q. Bai and G. Liu, *Journal of Catalysis*, 2019, **377**, 145–152.

17. S. Luo, Y. Liu, Y. Zhu, Q. Niu, M. Cheng, S. Ye, H. Yi, B. Shao, M. Shen, X. Wen, G. Zeng and Z. Liu, *Environmental Science: Nano*, 2021, **8**, 20–36.

18. Y. Wu, X. Ye, S. Zhang, S. Meng, X. Fu, X. Wang, X. Zhang and S. Chen, *Journal of Catalysis*, 2018, **359**, 151–160.

19. S. M. Hayes and E. A. McCullough, *Resources Policy*, 2018, **59**, 192–199.

20 M. Cely-Pinto, B. Wang and J. C. Scaiano, *Nanomaterials*, 2023, **13**, 2390.

21. D. R. C. da Silva and J. C. Scaiano, *Photochemistry and Photobiology*, 2023, **99**, 706–715.

22. B. Ohtani, O. O. Prieto-Mahaney, D. Li and R. Abe, *Journal of Photochemistry and Photobiology. A*, 2010, **216**, 179–182.

23. R. Cano, D. J. Ramón and M. Yus, *Journal of Organic Chemistry*, 2011, **76**, 5547–5557.

24. A. Zanardi, J. A. Mata and E. Peris, *Chemistry: A European Journal*, 2010, **16**, 10502–10506.

25. Y. Zhang, K. Fulajtárová, M. Kubů, M. Mazur, M. Hronec and J. Čejka, *Catalysis Today*, 2020, **345**, 39–47.

26. H. Hirao and T. Ohwada, *The Journal of Physical Chemistry A*, 2003, **107**, 2875–2881.

27. P. Sabatier, *Industrial & Engineering Chemistry Research*, 1926, **18**, 1005–1008.

28. H. Hirakawa, M. Katayama, Y. Shiraishi, H. Sakamoto, K. Wang, B. Ohtani, S. Ichikawa, S. Tanaka and T. Hirai, *ACS Applied Materials & Interfaces*, 2015, 7, 3797–3806.

29. J. Tong, J. Wang, X. Shen, H. Zhang, Y. Wang, Q. Fang and L. Chen, *Inorganic Chemistry*, 2021, **60**, 10715–10721.

30. J. Wu and C. Darcel, *The Journal of Organic Chemistry*, 2020, **86**, 1023–1036.

31. J. M. Pérez, R. Cano, M. Yus and D. J. Ramón, *European Journal of Organic Chemistry*, 2012, **24**, 4548–4554.

32. G. Zou, R. Cao, C. Cui, Y. Luo, C. Huang, X. Cui, Z. Wang and Y. Song, *Catalysis Science & Technology*, 2023, **13**, 3916–3926.

33. S. Higashimoto, Y. Nakai, M. Azuma, M. Takahashi and Y. Sakata, *RSC Advances.*, 2014, **4**, 37662–37668.

34. D. Liu, P. Yang, H. Zhang, M. Liu, W. Zhang, D. Xu and J. Gao, *Green Chemistry*, 2019, **21**, 2129–2137.

35. X. Ye, Y. Chen, Y. Wu, X. Zhang, X. Wang and S. Chen, *Applied Catalysis B: Environment and Eenergy*, 2019, **242**, 302–311.

36. T. A. Gawargy, P. Costa, A. E. Lanterna and J. C. Scaiano, *Organic & Biomolecular Chemistry*, 2020, **18**, 6047–6052.

37. C. Zhan, Q.-X. Wang, J. Yi, L. Chen, D.-Y. Wu, Y. Wang, Z.-X. Xie, M. Moskovits and Z.-Q. Tian, *Science Advances*, 2021, **7**, 1–7.

38. A. S. Hainer, J. S. Hodgins, V. Sandre, M. Vallieres, A. E. Lanterna and J. C. Scaiano, *ACS Energy Lett*ers 2018, **3**, 542–545.

39. S. J. A. Moniz, S. A. Shevlin, X. An, Z. Guo and J. Tang, *Chemistry: A European Journal*, 2014, **20**, 15571–15579.

40. L. Xu, L. Meng, X. Zhang, X. Mei, X. Guo, W. Li, P. Wang and L. Gan, *Journal of Hazardous Materials*, 2019, **379**, 120795.

41. A. Aguinaco, J. M. Mánuel, E. Blanco, M. Domínguez, R. Litrán, J. J. Delgado and M. Ramírez-del-Solar, *Materials*, 2022, **15**, 6718.

42. L. Xu, L. Qi, Y. Han, W. Lu, J. Han, W. Qiao, X. Mei, Y. Pan, K. Song, C. Ling and L. Gan, *Chemical Engineering Journal*, 2022, **430**, 132828.

43. L. Peng, T. Xie, Y. Lu, H. Fan and D. Wang, *Physical Chemistry Chemical Physics*, 2010, **12**, 8033.

44. D. W. Bahnemann, M. Hilgendorff and R. Memming, *The Journal of Physical Chemistry B*, 1997, **101**, 4265–4275.

45. M. Nolan, *Physical Chemistry Chemical Physics*, 2011, **13**, 18194.

46. K. Selvam, H. Sakamoto, Y. Shiraishi and T. Hirai, *New Journal of Chemistry*, 2015, **39**, 2467–2473.

5.4.Pre-submission Version of Supporting Information

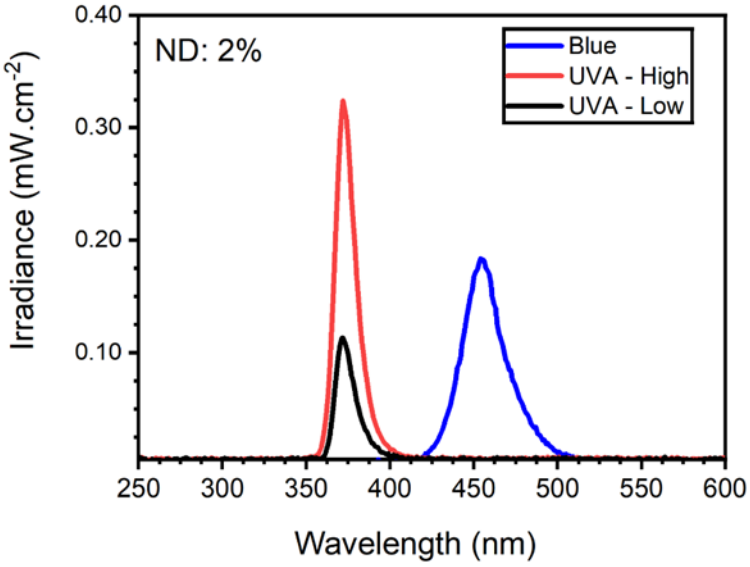

Figure S5.4.1. Emission spectra of light sources used in this work. In Blue 1x450 nm LED, in red 1x370 nm LED (UVA at higher intensity) and in black 1x370 nm LED (UVA at Lower intensity). ND: neutral density filter.

Figure S5.4.2. Fe_3O_4@TiO_2 after its synthesis next to a magnet to demonstrate its response to an external magnetic field.

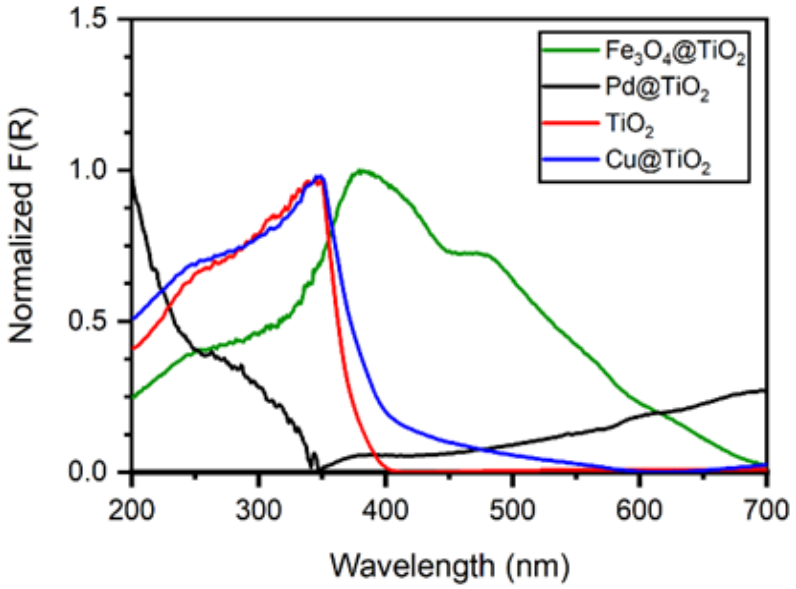

Figure S5.4.3. Diffuse Reflectance of the catalysts used in this study.

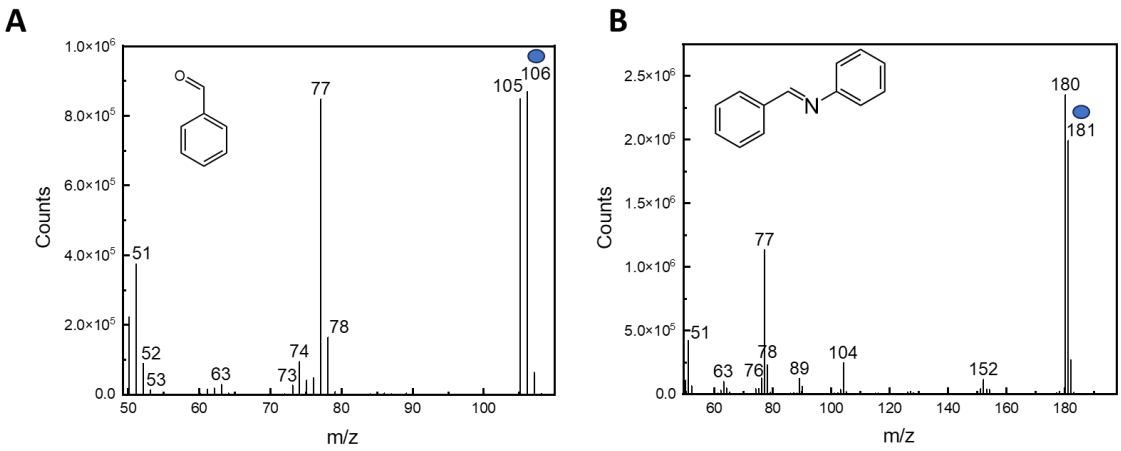

Figure S5.4.4. Mass spectra of the products. Each spectrum shows (●) the molecular ion of the molecules.

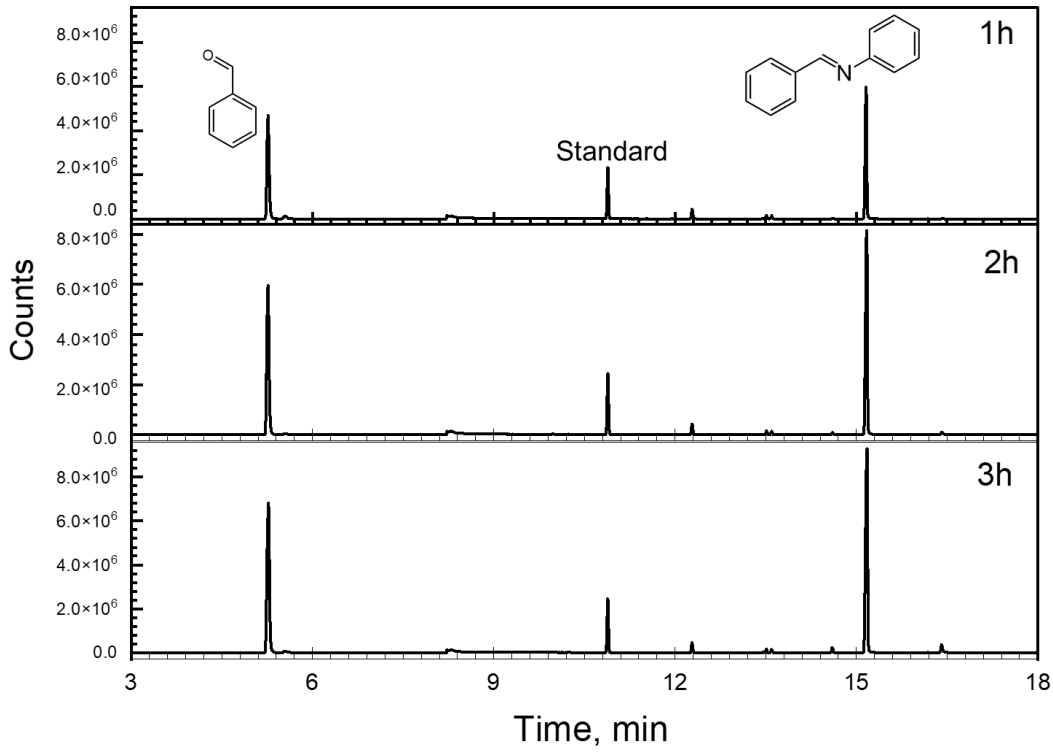

Figure S5.4.5. Chromatograms showing the peaks obtained after performing the reaction with nitrobenzene 0.1 M in benzyl alcohol and 10 mg of TiO_2. 3,5-Di-tert-butyltoluene was used as an external standard (peak at 10.84 min) The major products have the following retention times: BenzA (5.17 min), Schiff Base (15.10 min). The timed events feature of the local user interface was used (Turned off at 6.20 minutes and activated at 8.70 minutes) to prevent the risk of a high concentration of Benzyl Alcohol reaching the detector.

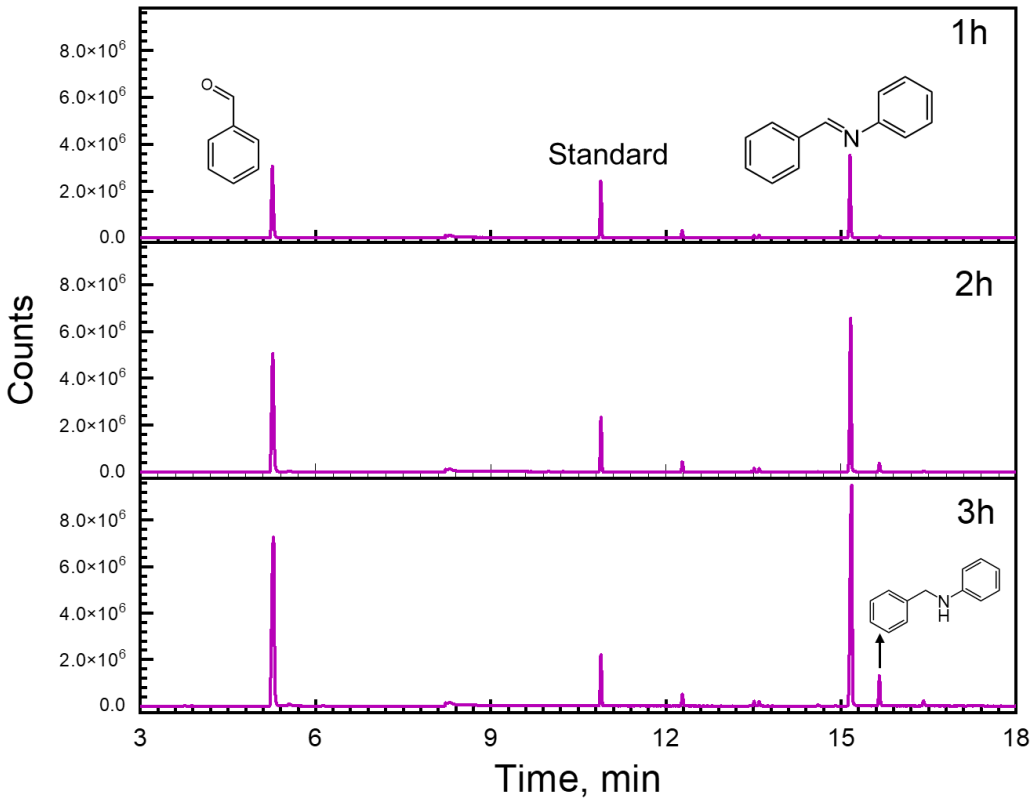

Figure S5.4.6. Chromatograms showing the peaks obtained after performing the reaction with nitrobenzene 0.1 M in benzyl alcohol and 10 mg of Pd@TiO_2. 3,5-Di-tert-butyltoluene was used as an external standard (peak at 10.84 min) The major products have the following retention times: BenzA (5.17 min), Schiff Base (15.10 min). The timed events feature of the local user interface was used (Turned off at 6.20 minutes and activated at 8.70 minutes) to prevent the risk of a high concentration of Benzyl Alcohol reaching the detector.

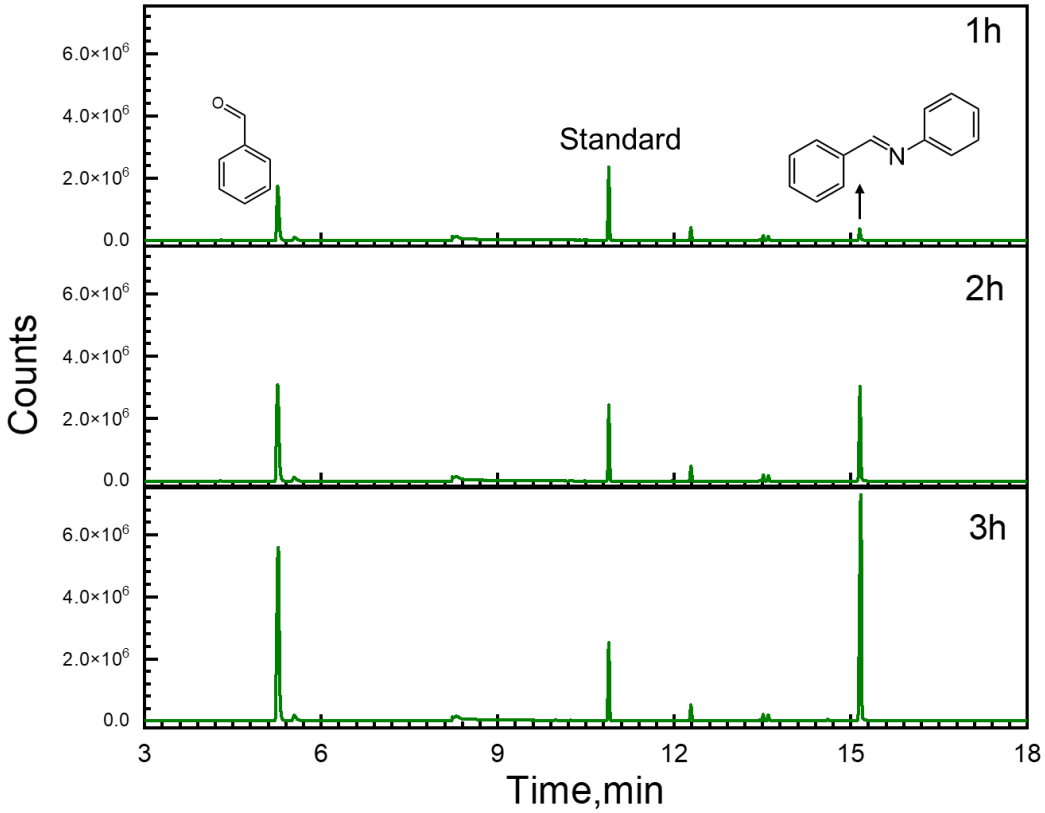

Figure S5.4.7. Chromatograms showing the peaks obtained after performing the reaction with nitrobenzene 0.1 M in benzyl alcohol and 10 mg of Cu@TiO_2. 3,5-Di-tert-butyltoluene was used as an external standard (peak at 10.84 min) The major products have the following retention times: BenzA (5.17 min), Schiff Base (15.10 min). The timed events feature of the local user interface was used (Turned off at 6.20 minutes and activated at 8.70 minutes) to prevent the risk of a high concentration of Benzyl Alcohol reaching the detector.

Table S5.4.1. Comparison table illustrating the findings of this study alongside previous research on the one-pot Schiff Base synthesis using nitrobenzene and benzyl alcohol as reagents. The table shows the production rates in mmol h^{-1} achieved with various catalytic materials under different conditions. Production rates were estimated using the highest published yields for each reference, multiplying the initial nitrobenzene concentration, divided by the reaction times.

Catalyst	Time (Hours)	Atm	Light (nm) or Heat (ºC)	Yield (%)	Schiff base production rate (mmol/H)	Reference
Fe_3O_4@TiO_2	6	N_2	>300	41.6	6.8	This work
$CdIn_2S_4$	8	N_2	>420	32	0.34	[1]
Co–N–C/CNT@AC	18	N_2	Heat 160	97	0.26	[2]
PC-TiO_{2-x}_590	18	Ar	>300	100	0.02	[3]
P25	10	N_2	>300	93	0.005	[4]
$F_{0.04}$-BMO-NS	10	N_2	≥ 400	95.5	0.0019	[5]
CdS (15 wt%)–TiO_2	10	N_2	420	-	0.0018	[6]
$Cd_XZn_{1-X}S$	4	Air	>420	55	0.0011	[7]

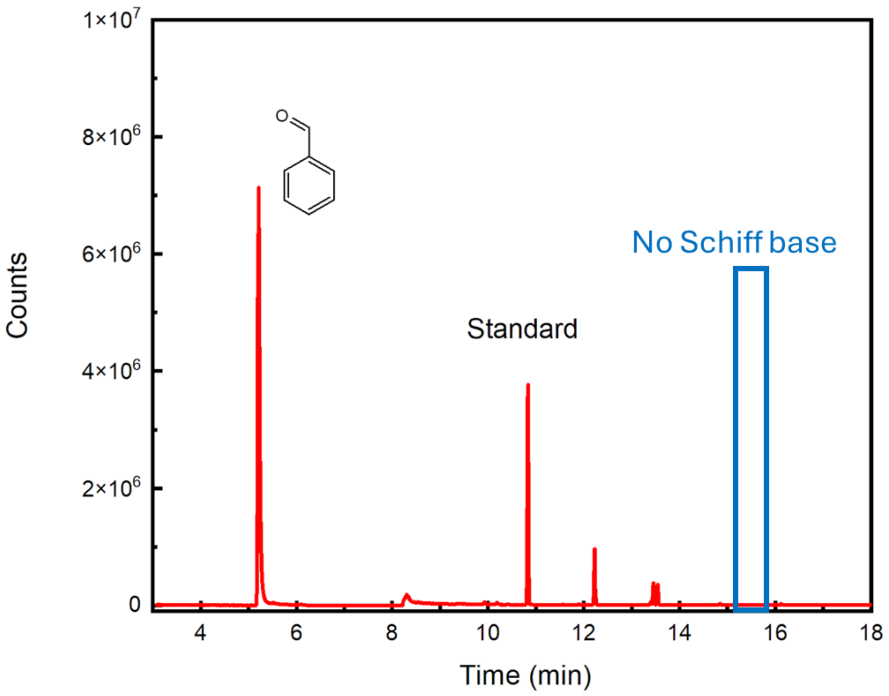

Figure S5.4.8. Chromatogram showing the peaks obtained after 3 hours at 450 nm light irradiation. No peak for the Schiff base (15.10 min) was obtained after reacting with nitrobenzene 0.1 M in benzyl alcohol and 10 mg of Fe_3O_4@TiO_2. 3,5-Di-tert-butyltoluene was used as an external standard (peak at 10.84 min). The timed events feature of the local user interface was used (Turned off at 6.20 minutes and activated at 8.70 minutes) to prevent the risk of a high concentration of Benzyl Alcohol reaching the detector.

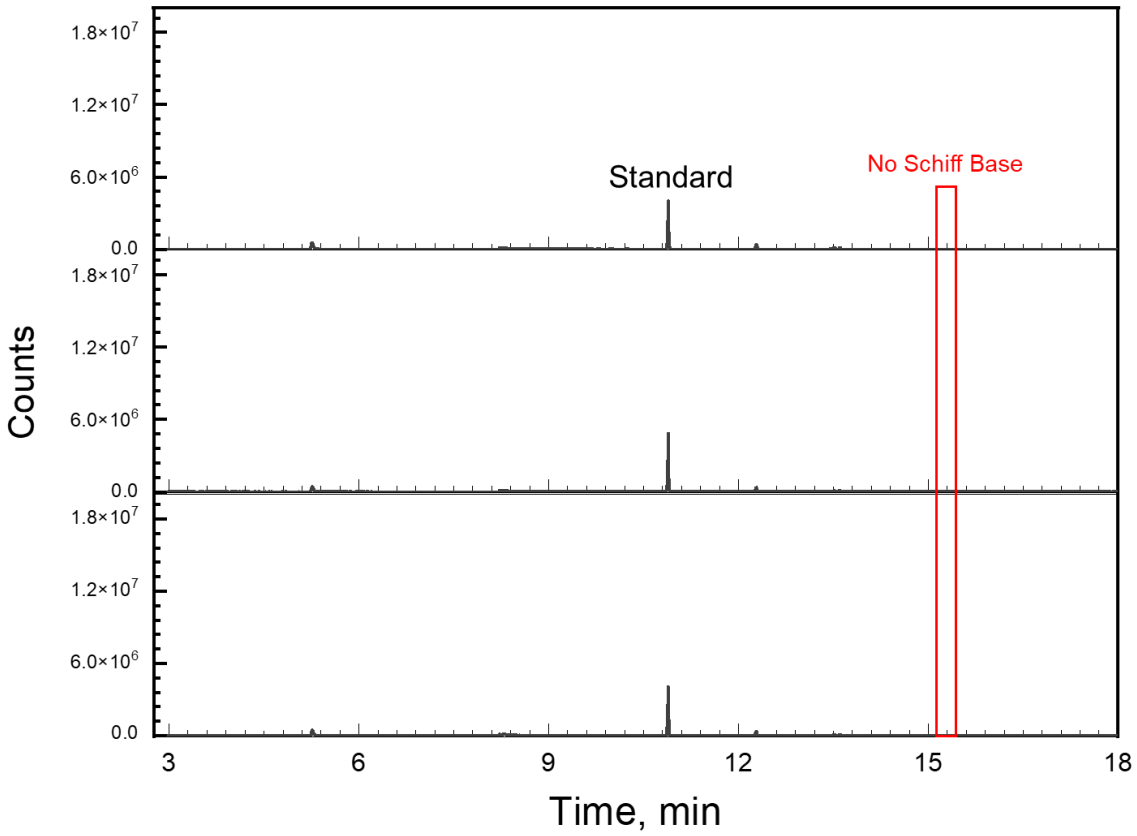

Figure S5.4.9. A control Experiment without light irradiation Chromatogram showing no peak for the Schiff base (15.10 min) was obtained after reacting with nitrobenzene 0.1 M in benzyl alcohol and 10 mg of Fe_3O_4@TiO_2. 3,5-Di-tert-butyltoluene was used as an external standard (peak at 10.84 min). The timed events feature of the local user interface was used (Turned off at 6.20 minutes and activated at 8.70 minutes) to prevent the risk of a high concentration of Benzyl Alcohol reaching the detector.

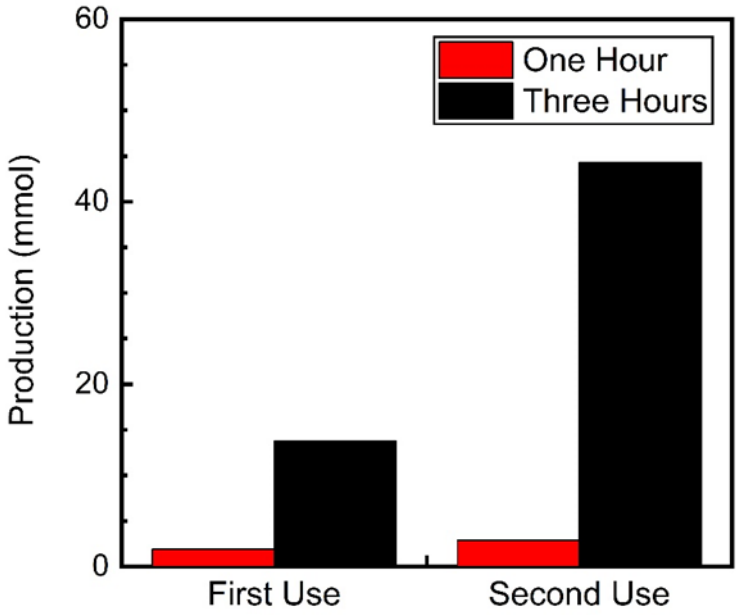

Figure S5.4.10. N-benzylamine production using Fe_3O_4@TiO_2 as catalyst (10 mg) irradiated for up to 3 hours with UVA (λ= 370 nm) under N_2 atmosphere. After the first round of irradiation (first use), 0.1M of nitrobenzene was added to the solution and irradiated for another 3 hours (second use). Schiff-base production was quantified using GC-MS.

5.5. References for the Supporting Information section

1. X. Ye, Y. Chen, C. Ling, R. Ding, X. Wang, X. Zhang and S. Chen, *Dalton Transactions*, 2018, **47**, 10915–10924.

2. D. Liu, P. Yang, H. Zhang, M. Liu, W. Zhang, D. Xu and J. Gao, *Green Chemistry*, 2019, **21**, 2129–2137.

3. J. Tong, J. Wang, X. Shen, H. Zhang, Y. Wang, Q. Fang and L. Chen, *Inorganic Chemistry*, 2021, **60**, 10715–10721.

4. H. Hirakawa, M. Katayama, Y. Shiraishi, H. Sakamoto, K. Wang, B. Ohtani, S. Ichikawa, S. Tanaka and T. Hirai, *ACS Applied. Materials & Interfaces.*, 2015, **7**, 3797–3806.

5. G. Zou, R. Cao, C. Cui, Y. Luo, C. Huang, X. Cui, Z. Wang and Y. Song, *Catalysis Science & Technology*, 2023, 13, 3916–3926.

6. S. Higashimoto, Y. Nakai, M. Azuma, M. Takahashi and Y. Sakata, *RSC Advances*, 2014, 4, 37662–37668.

7. L. Peng, T. Xie, Y. Lu, H. Fan and D. Wang, *Physical Chemistry Chemical Physics*, 2010, 12, 8033.

6. Future Directions and Conclusions

6.1. Summary and Conclusions from the Chapters Presented

In all parts of this dissertation, the theme is centered on strategies for designing and applying nanomaterials in photocatalysis along with the exploration of the photochemistry of different molecules. The applied research presented in this doctoral thesis makes a significant contribution toward different methodologies related to the synthesis of nanoparticles, metal-supported catalysts, and also the development of novel catalysts supports for a wide variety of organics transformations, such as the synthesis of alkenes and Schiff bases.

The use of the substituted tetralone as a precursor for the photogeneration of gold nanoparticles (AuNPs), described in Chapter 2, represents an important advancement in nanomaterial synthesis due to its efficiency under UVA irradiation. This process uses the biradical species generated when the substituted tetralone undergoes photoenolization. At this point of the reaction, the ketyl moiety acts as a potent reductant for the reduction of gold ions to form AuNPs. The process shows fast kinetics, yielding AuNPs in minutes, which is a great advantage for practical applications requiring fast synthesis. One notable aspect of this study is the unique feature of the substituted tetralone's chemistry described in this Chapter, *i.e.*, its ability to revert to its original form as part of the ground state keto-enol equilibrium after the reduction process. This feature is essential when compared to other systems where failure of reductant species can lead to unwanted byproducts, which ensures cleaner synthesis and higher purity of the AuNPs.

Future directions for this chemistry could involve exploring its application in more complex nanoparticle structures or hybrid materials. Additionally, exploring further parameters such as irradiation intensity and solvent effects, could further provide insights into the control over nanoparticle size, shape, and surface properties. Furthermore, understanding the mechanistic details at the molecular level of different substituted tetralones with properties like the one used in this Chapter, through advanced spectroscopic

and computational techniques would deepen insights into the photochemical processes involved, opening doors to more efficient nanoparticle synthesis methodologies.

On the other hand, as detailed in Chapter 3, the use of α-lipoic acid and its polymer (PALA), represents a significant advancement in the synthesis of gold nanostructures. These compounds serve dual roles: *(i)* stabilizing gold nanostructures and *(ii)* enabling precise control over their size. When combined with photoenolizable tetralones, the fast and efficient generation of gold nanostructures is facilitated, which offers distinct advantages. Unlike other photoinitiated molecules, 3,3,6,8-tetramethyl-1-tetralone exhibits a unique capability where its intermediate species, the photoenol, if fails to reduce gold, it could revert to the original tetralone form, minimizing chemical byproducts and ensuring cleaner nanostructure synthesis.

Beyond nanoscience applications, this research contributes to a deeper understanding of the photochemistry of α-lipoic acid. This improved understanding enhances its efficacy in stabilizing nanoparticles and also helps advance its use in biology and health. Future directions could explore further optimization of polymer stabilized nanostructures, exploring their potential in catalysis, and biomedical applications.

Regarding the semi-hydrogenation process of alkynes, the balance between kinetics and selectivity is crucial for successful results, especially in practical laboratory settings where precise timing is often challenging. As described in Chapter 4, Pd@TiO_2, while effective, requires accurate timing to maintain high yields and selectivity, making it less practical for reactions that extend over longer periods, such as overnight reactions. On the other hand, Cu@TiO_2 and CuPd@TiO_2 catalysts demonstrate superior selectivity with less strict timing requirements. CuPd@TiO_2, in particular, not only matches but slightly improves selectivity compared to Cu@TiO_2, performing approximately 52% faster the semi-hydrogenation process of alkynes, preserving the selectivity but also offering a small improvement in the kinetics of the reaction to that obtained when working with Cu@TiO_2.

The recommendation of using this bimetallic catalyst, CuPd@TiO_2, with methanol as a solvent for alkyne semi-hydrogenation suggests a promising way to enhance reaction

efficiency and selectivity in laboratory-scale applications. Future research directions should focus on optimizing reaction times further to expedite semi-hydrogenation processes without compromising selectivity towards alkenes. This optimization could involve exploring additional catalyst modifications, varying reaction conditions, or investigating alternative solvents to enhance efficiency while maintaining control over the critical point of conversion between alkene to alkane. Additionally, deeper mechanistic studies could provide insights into the factors that influence catalyst performance, opening the way for the design of next-generation catalysts with improved efficiency and versatility across different semi-hydrogenation reactions.

Finally, Fe_3O_4@TiO_2 serves as a magnetic catalyst in organic synthesis, particularly in the formation of Schiff Bases as described in Chapter 5, shows promising potential despite its current underutilization. Our study demonstrates that Fe_3O_4@TiO_2 efficiently catalyzes the synthesis of Schiff Bases, achieving high yields with extended reaction times, up to nearly 99% after 20 hours. This efficacy contrasts with traditional catalysts like Pd@TiO_2 and Cu@TiO_2, which, while effective, often produce undesirable over-hydrogenation products, particularly when working with Pd. The key advantage of Fe_3O_4@TiO_2 lies in its rapid separation from reaction mixtures, facilitated by its magnetic properties. This feature not only simplifies the separation process of the catalyst from the reaction but also enhances the catalyst's recyclability and reduces environmental impact. Furthermore, the use of iron-based materials like Fe_3O_4@TiO_2 offers a cost-effective alternative to precious metals like Palladium, addressing both economic and sustainability concerns in catalytic processes. The research has advanced significantly, resulting in published findings (*Catalysts, 2024, 14(9), 612*). While UVA irradiation alone can effectively photocatalyze the process, incorporating blue light (450 nm) significantly accelerates it. Dual-wavelength irradiation not only increases benzaldehyde production but also doubles the yield of the Schiff base. Additionally, the reusability of the catalyst under simultaneous light exposure (450 nm and 370 nm) markedly enhances Schiff base production. These results highlight the potential of color-coordinated catalysis in promoting innovative chemistry through two-color photochemistry.

Future research directions for this line of research should focus on expanding the scope of applications for Fe_3O_4@TiO_2 in diverse organic transformations beyond Schiff Base synthesis. Optimization of reaction conditions and exploration of its catalytic performance in more complex reactions could further highlight its versatility and efficiency. Additionally, deeper mechanistic studies are essential to elucidate the catalytic mechanisms and facilitate the design of enhanced magnetic catalysts for specific chemical reactions. Additionally, exploring its application in flow chemistry could provide insights into scaling up the synthesis of Schiff bases or other organic compounds on a larger scale. These advancements in magnetic catalysts, such as Fe_3O_4@TiO_2, have the potential to greatly influence sustainable practices in chemical synthesis.

In conclusion, this thesis research has demonstrated the potential of photochemistry, photocatalysts, and nanostructures for different applications. The results emphasize the need to continue exploring new materials and designs to improve photocatalytic efficiency and sustainability. Future work should focus on optimizing these systems by integrating computational modeling with experimental methods. By working together across disciplines, we can develop innovative solutions to important global challenges in environmental science, pharmaceuticals and industrial processes.

6.2. Polarity Reversal Catalysis

In addition to the studies described in this thesis, there is an additional one in which I was involved with my colleague Saba Didarataee and it is Polarity Reversal Catalysis (PRC). The basis of PRC is to replace a single-step abstraction process, for example, hydrogen abstraction, that is slow because of unfavorable polar effects, with a two-step process where radicals and substrates are matched in polarity to enhance efficiency.[1] This process is depicted in the Scheme 6.2.1.

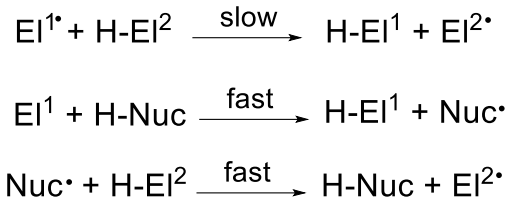

Scheme 6.2.1. The principle underlying PRC of hydrogen atom transfer. El refers to an electrophilic species, while Nuc to a nucleophilic one.

Most common free radicals are electrophilic which typically results in slow hydrogen atom transfers (HAT) from electron-deficient groups. For instance, alkoxyl radicals readily abstract hydrogen from hydrocarbons like cyclopentane or cyclohexane (Bond dissociation energy, BDE, of 400 kJ/mol[2]), whereas acetonitrile (BDE of 410 kJ/mol[3]), despite having similar BDE for C-H bonds, acts as a relatively inert solvent. Roberts[1] suggests that promoting hydrogen abstraction from acetonitrile by electrophilic alkoxyl radicals can be achieved with a small amount of amine–alkylborane. This transforms the electrophilic alkoxyl radical into a nucleophilic amine–boryl radical, this concept is known as polarity-reversal catalysis. Reactions 1-3 in Scheme 6.2.2 depict this idea, focusing on tert-butyl amino borane (specifically, borane tert-butylamine complex), a molecule that was used in this study.

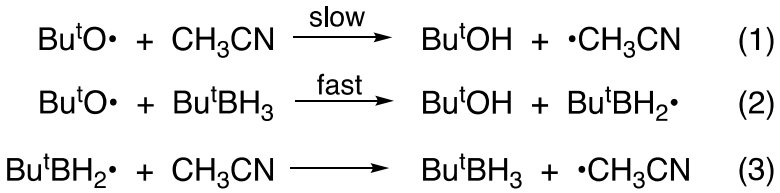

Scheme 6.2.2. The principle behind PRC when using acetonitrile, a tert-butoxy radical and amino borane in the reaction. Hydrogen abstraction from the tert-butoxy radical to acetonitrile which acts as an electrophilic species (1). Amino borane serves as the nucleophilic species capable of donating hydrogen to the electrophilic tert-butoxy radical (2). The radical species derived from amino borane can then abstract hydrogen from acetonitrile, thereby regenerating itself.

Initially, we decided to use our LFP system to monitor the formation of radicals resulting from this specific reaction. Di-tert-butyl peroxide (DTBP) was chosen as the solvent of choice due to the well-established electrophilic characteristics of its alkoxy radical after irradiating with a laser pulse of 355 nm. This radical can abstract hydrogen atoms, a crucial step in our experimental setup, particularly from the amino borane molecule, as outlined in reaction 2 in Scheme 6.2.2. In our experimental procedure, a solution containing 21 mM of amino borane dissolved in DTBP was prepared to monitor its change in absorbance during time at 400 nm. This initial monitoring revealed a characteristic decay, indicative of the formation of the amino borane radical after hydrogen abstraction from DTBP (Figure 6.2.1 A). Upon further investigation, we analyzed the spectrum of the radical and noted a prominent absorption band centered around 400 nm (Figure 6.2.1 B), aligning perfectly with our monitoring wavelength. The distinct presence of this absorption band provided crucial evidence supporting the generation and stability of the amino borane radical within the DTBP solvent environment. Furthermore, our kinetic analysis revealed that the decay of the amino borane radical followed first-order kinetics. By fitting the decay curve, we determined the specific lifetime of the amino borane radical in DTBP to be 2.2 μs. This precise measurement highlights the identifiable nature of the radical species formed in our experimental conditions. Ultimately, this comprehensive experiment using LFP successfully allowed us to monitor and characterize a boryl radical, thereby confirming the anticipated chemical reaction described in reaction 2 from Scheme 6.2.2.

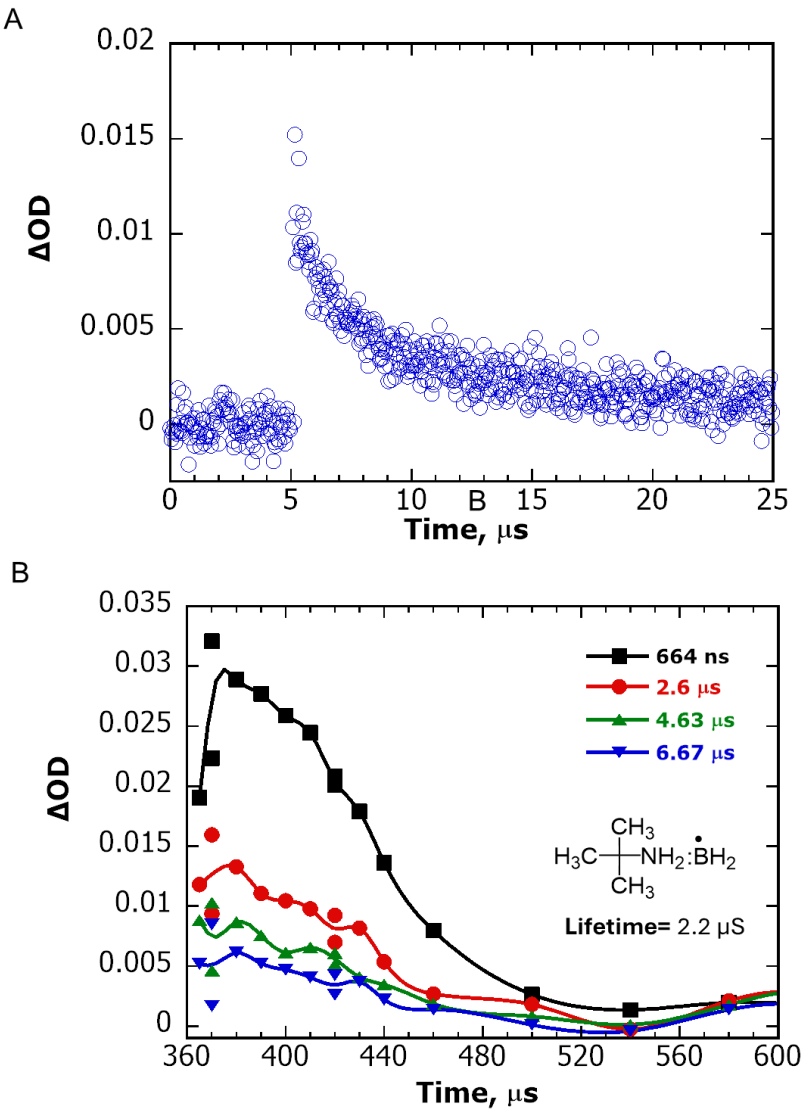

Figure 6.2.1. Transient signal decay monitored at 400 nm under Ar **(A)**; Transient spectra upon 355 nm laser excitation of the sample containing amino borane 21 mM in DTBP under Ar. Monitored at four different times following laser excitation **(B)**.

Additionally, into the same cuvette containing DTBP and amino borane, 0.25 M acetonitrile (CH_3CN) was added with the expectation that the signal corresponding to the boryl radical would be quenched, consistent with reaction 3 in Scheme 6.2.2. This reaction describes the process where the amino borane radical abstracts hydrogen from acetonitrile. As anticipated, the transient signal monitored at 400 nm, indicative of the presence of the

boryl radical, disappeared upon the addition of CH_3CN (Figure 6.2.2, red data). This observation confirmed that nucleophilic species present in the solution, such as the amino borane radical, are indeed capable of abstracting hydrogen from electron-deficient substrates such as CH_3CN.

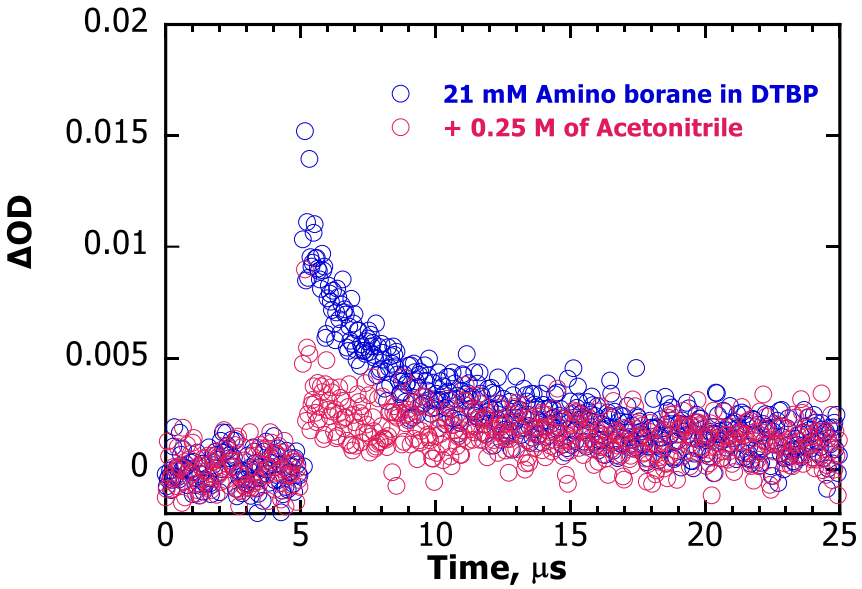

Figure 6.2.2. Transient signals decays monitored at 400 nm under Ar for a solution contianing 21 mM Amino borane in DTBP (blue data) and after the addition of 0.25 M of CH_3CN, leading to the quenching of the detected boryl radical transient decay (red data).

This experimental result emphasizes the reactivity and specificity of the amino borane radical towards hydrogen abstraction from acetonitrile. This interaction exemplifies the utility of our experimental approach in studying radical interactions and their reactivity within different solvent environments, offering insights into chemical pathways involving nucleophilic radicals and their interactions with electron-poor substrates.

This ongoing project focuses on the mechanistic and kinetic aspects of polarity reversal catalysis using amino-borane compounds as catalysts. These compounds generate nucleophilic radicals capable of abstracting hydrogen from electron-poor substrates like nitriles. By studying these reactions, we would like to understand how electrophilic radicals can be formed from typically electron-deficient molecules. Additionally, this study will

involve measuring absolute rate constants for various reaction steps involving different reactants used in organic synthesis. These include hydrogen abstractors, alkoxyl radicals, and ketone triplets such as benzophenone and xanthone. The future work of this study will include the determination of a rate constant for hydrogen abstraction by decatungstate (DT, $W_{10}O_{32}^{4-}$) triplet, a novel catalyst currently under exploration by our group which is capable of abstraction of hydrogen atoms from a range of substrates, including hydrocarbons,[4] alcohols,[4, 5] ethers[6] and amines[4, 7]. By using LFP we could establish a comprehensive library of absolute rate constants. These quantitative tools are essential for the systematic and rational design of catalytic processes using polarity reversal mechanisms. They provide critical insights into reaction kinetics and enable the development of more efficient and selective catalytic systems in organic chemistry.

In conclusion, polarity reversal offers intriguing possibilities in organic chemistry, especially when light is used as part of the system. This approach can challenge conventional reaction pathways, leading to more efficient and selective transformations. By exploring this research topic, chemists can unlock new synthetic methods and enhance materials development.

6.3. References

1. Brian P. Roberts, *Chemical Society Reviews*, 1999, **28**, 25–35.

2. N. Koshino, Y. Cai and J. H. Espenson, *Journal of Physical Chemistry A*, 2003, **107**, 4262–4267.

3. L. Gribov, I. Novakov, I. Pavlyuchko, V. V Korolkov and B. S. Orlinson, *Journal of Structural Chemistry*, 2004, 45, 771–777.

4. D. C. Duncan and M. A. Fox, *Journal of Physical Chemistry A*, 1998, **102**, 4559–4567.

5. C. Tanielian, F. Cougnon and R. Seghrouchni, *Journal of Molecular Catalysis A: Chemical*, 2007, **262**, 164–169.

6. L. Capaldo, S. Bonciolini, A. Pulcinella, M. Nuño and T. Noël, *Chemical Science*, 2022, **13**, 7325–7331.

7. I. Texier, J. A. Delaire and C. Giannotti, *Physical Chemistry Chemical Physics*, 2000, **2**, 1205.

7. Appendix

7.1. Journal Permissions

This dissertation includes revised manuscripts and images that have been republished with permission from the original publishing journals.